A SEARCH FOR WEAKLY INTERACTING MASSIVE PARTICLES
UTILIZING A PROFILE LIKELIHOOD RATIO TECHNIQUE
WITH THE SUPERCDMS SOUDAN EXPERIMENT

Approved by:

Dr. Jodi Cooley
Associate Professor of Experimental
Particle Physics

Dr. Pavel Nadolsky
Associate Professor of Theoretical Physics

Dr. Jingbo Ye
Professor of Experimental Particle
Physics

Dr. Daniel Akerib
Professor of Particle Physics &
Astrophysics, SLAC

A SEARCH FOR WEAKLY INTERACTING MASSIVE PARTICLES UTILIZING A PROFILE LIKELIHOOD RATIO TECHNIQUE WITH THE SUPERCDMS SOUDAN EXPERIMENT

A Dissertation Presented to the Graduate Faculty of the

Dedman College

Southern Methodist University

in

Partial Fulfillment of the Requirements

for the degree of

Doctor of Philosophy

with a

Major in Physics

by

Hang Qiu

B.S., Physics, University of Science and Technology of China, P.R.China
M.S., Physics, Southern Methodist University, United States of America

May 20, 2017

ACKNOWLEDGMENTS

It is an honor for me to work in the direct dark matter search area with the SuperCDMS collaboration during my PhD years. This experience has greatly broadened my view in the physics field. I have participated most in the data analysis and simulation teams, which provided me not only the opportunities in the relevant researches using the current operating experiment (SuperCDMS Soudan), but also an opportunity to work on the blueprint of the future experiment (SuperCDMS SNOLAB).

This short page is not long enough to express my thanks to everyone who has accompanied me through all these years, from collaboration members, professors in the SMU physics department, and to my friends and family. Although I could not list out all of you here, I want to dedicate my sincere thanks to every one of you.

I would like to thank the whole mine crew at the Soudan Underground Laboratory. You made my shifts there much smoother and shared lots of happiness with me. I would also like to thank all the members from the SuperCDMS collaboration who traveled with me, either to an onsite shift or to a conference. Being in another city means that people need to take care of each other more. After returning to the surface from a 10-hour underground shift, I would like to specially thank all the drivers who took everyone out to dinner at a place 20 miles away. During stays at a conferences or meetings, I would especially like to thank all the roommates who had shared a hotel room with me and did not kick me out.

During my time in the simulation group, I would especially like to thank Ben Loer who provided me with much insightful guidance. When I struggled to understand the zero live-time events, I would like to thank Joel Sander who patiently talked with me on the phone

and helped me with all my DAQ questions. Working in the high mass WIMP search analysis team, I would like to express my thanks to Ray Bunker, Robert Calkins, Brett Cornell, Todd Doughty, and Brad Welliver. A lot of efforts and new ideas have been put into this analysis and the conversations during the team meetings are always intriguing and fruitful. I would also want to thank Professor Eilam Gross, who visited SMU in April 2016 and provided me with lots of valuable suggestions on how to utilize the profile likelihood ratio technique in data analysis.

Being at SMU, I have the privilege to work closely with my advisor, Professor Jodi Cooley. She does not only have sound knowledge in the dark matter search area, but also possesses outstanding skills to pass them to her students. She works in an excellently balanced way managing the team function in an optimal way while still giving the team members enough freedom. As an international student here in the US, I especially want to thank her for her cares. One time I was traveling to Canada. Considering my potential visa issue on returning back to the US, she arranged with our collaborators in Canada to host me for a month in the case that I could not get back. I did not even think about the possibility of this visa issue myself. I happened to find out her arrangement two or three months after I came back. This is just one example and there are certainly many more. I almost could write a book but I would stop here for one paragraph.

For the local SuperCDMS team, I would like to express my thanks to Dr. Durdana Balakishiyeva, Dr. Silvia Scorza, Dr. Robert Calkins, Bedile Karabuga, Dan Jardin, and Matt Stein. During my early research time, Silvia provided me with a lot of great suggestions to help me get into a research frame of mind and become familiar with the atmosphere. She taught me a lot of useful skills in both analysis and simulation, which prepared me for later works. Rob came after Silvia and supervised me on various tasks. I have benefited greatly from his expertise in many areas. His good work ethic has also influenced me for a long time. Although he welcomed me every time when I went to his office for discussion, I do

want to apologize to him that I have interrupted him too much and made his work time into a discrete pattern, not to mention that his willingness to discuss research topics even after work and on weekends. In addition to them, Durdana and my fellow grad students Bedile, Dan, and Matt were of great help to me on not only the discussions during the routine group meetings, but also shared ideas on a daily basis.

Last but not least, I would like to thank all my friends here in Dallas. Without you, my personal life would not be as delightful as it has been. I also would not forget my family members, who have provided me with consistent support and love. I could choose an easier life but I chose this path to pursue a physics PhD on the other half of the Earth. No matter when I got frustrated, I never felt your love had gone away. To my parents, I feel really sorry that being your son, I have been staying in a different continent for too long. Although technology has advanced and we could video chat, I still want to apologize for not being around you, accompany you, and love you.

I am grateful to everyone who has helped me reach this point of my life. God bless you all.

Qiu, Hang B.S., Physics, University of Science and Technology of China, P.R.China
M.S., Physics, Southern Methodist University, United States of America

A Search for Weakly Interacting Massive Particles
Utilizing a Profile Likelihood Ratio Technique
with the SuperCDMS Soudan Experiment

Advisor: Dr. Jodi Cooley
Doctor of Philosophy degree conferred May 20, 2017
Dissertation completed April 25, 2017

Dark matter accounts for ∼26.8% of the universe's mass and ∼85% of the matter of the universe. The majority of dark matter is in the form of non-baryonic dark matter. Among all the dark matter particle candidates, the Weakly Interacting Massive Particle (WIMP) is considered the most promising. Tens of experiments around the world are under the searches of WIMPs. The Super Cryogenic Dark Matter Search (SuperCDMS) is one of the leading direct dark matter search experiments. Its latest experiment was located in the Soudan Underground Laboratory in northern Minnesota. By placing its germanium (Ge) detectors deep underground, it aimed at performing a rare-event search in the case that a WIMP would collide with a Ge nucleus and leave a Ge nuclear recoil signal in the detectors. These Ge detectors were operated at a temperature of ∼50 mK to reduce the noise from disturbing the ionization and phonon signal collections.

A high mass WIMP search analysis is performed on the recent collected data sets at Soudan. It aims at exploring WIMPs with masses from the order of 10 GeV/c^2 and above. With a raw exposure of 1657.54 kg-days, an exclusion limit is set on the spin-independent WIMP-nucleon cross section at 1.32 $\times 10^{-44}$ cm^2 for a 75 GeV/c^2 WIMP at a 90% confidence level by the profile likelihood ratio technique.

Neutrons are the most dangerous background in a direct dark matter search experiment. The nuclear recoil signal that a neutron produces in a Ge detector is indistinguishable from

that a WIMP produces. Protection against them is one of the key aspects for the next generation of SuperCDMS experiment at SNOLAB. An active neutron veto system was proposed to be implemented in this future experiment to make it more robust from neutrons. The feasibility of both the plastic and liquid neutron veto systems was studied.

TABLE OF CONTENTS

LIST OF FIGURES xii

LIST OF TABLES xxi

CHAPTER

1. Existence of Dark Matter 1
   1.1. Invisible Mass in the Coma Cluster 1
   1.2. Evidence of Dark Matter 2
      1.2.1. Rotational Curves of Galaxies 2
      1.2.2. The Bullet Cluster 3
   1.3. Dark Matter Component in the Universe 6
   1.4. Dark Matter Particle Candidates 7
2. Weakly Interacting Massive Particles 9
   2.1. The WIMP Miracle 9
   2.2. The Lightest Neutralino 11
   2.3. Dark Matter Detection Methods 12
   2.4. Direct Detection Event Rates 14
   2.5. Three Key Points to a Direct Detection Experiment 16
   2.6. Experiment Sensitivity 18
3. SuperCDMS 20
   3.1. iZIP Detectors 20
      3.1.1. Ionization Signal Collection 22
      3.1.2. Phonon Signal Collection 28
   3.2. Shielding Layers 31
   3.3. Data Acquisition and Processing 36

4. Backgrounds 40
4.1. Gammas 40
4.2. Alphas, Betas and ^{206}Pb 43
4.2.1. Identifying Alpha Particles 44
4.3. Neutrons 50
4.3.1. Cosmogenic Neutrons 50
4.3.2. Radiogenic Neutrons 52
5. Simulations for SuperCDMS SNOLAB 54
5.1. Simulation with SuperSim 54
5.1.1. Geometry 55
5.1.2. Neutron Emission Spectra from SOURCES4 Calculation 55
5.1.3. Output 58
5.2. SuperCDMS SNOLAB Background Estimations 59
5.3. Active Neutron Veto Shield 66
5.3.1. Plastic Scintillator 67
5.3.2. Liquid Scintillator 73
6. Data Sets and Livetime Cuts 79
6.1. Raw Livetime and Target Mass 79
6.2. Particle Identification 80
6.3. Blinding Scheme 81
6.4. Detector Calibration 83
6.4.1. Pile-up 84
6.4.2. Charge and Phonon Calibration 89
6.5. Data Selection 90
7. High Mass WIMP Search 105

7.1. Event selection 105
7.2. Background Modeling 108
7.3. WIMP Signal Modeling 114
7.4. Likelihood Ratio 118
7.5. Analysis 121
7.6. Exclusion Limit 127
8. Conclusion and Future 133
8.1. Analysis with a Profile Likelihood Ratio Method 133
8.2. Future Experiment at SNOLAB 135
APPENDIX
A. Neutron Emission Spectra from Uranium and Thorium Decays 136
B. Data Selection Criteria for the High Mass WIMP Search Analysis 144
C. Statistical Methods 150
C.1. Some Common Distributions 150
C.2. Extended Likelihood 153
C.3. Hypothesis Test 154
BIBLIOGRAPHY 157

LIST OF FIGURES

Figure Page

1.1 (Top plot) Rotational velocity (unit: km/s) in M31 as a function of the distance (unit: minutes of arc) from its center. At a distance of 690 kpc for M31, 1 minute of arc (1') is equal to a distance of 200 pc. The most distant region observed was at 120' (24 kpc). The solid curve is the fitted rotation curve [3]. (Bottom plot) The solid curve is from observation of a galaxy whose rotation curve is flat at large distance. The dashed curve is a prediction based on calculations using Newtonian dynamics [4]. 4

1.2 (a) Contours of the weak gravitational lensing mass overlay on the optical image of 1E0657-56. Dashed curves are negative relative to an arbitrary zero level. (b) Contours of the upper four mass levels (for clarity purpose) overlay on the X-ray image. Gravitational potential of the X-ray gas can be derived from its temperature measurement. After the collision, the gas lags behind the dark matter subcluster [5]. 5

1.3 The anisotropies of the cosmic microwave background (CMB) as observed by Planck. The CMB is a snapshot of the oldest light in our universe, imprinted on the sky when the universe was just 380 000 years old. It shows tiny temperature fluctuations that correspond to regions of slightly different densities, representing the seeds of all future structure: the stars and galaxies of today. *Copyright: ESA and the Planck Collaboration [8].* 6

2.1 This plot shows the WIMP number density during the freeze-out stage in the pre-BBN era in a form of Y(x)/Y(x+1) as a function of x=m/T where Y=n/s (solid line). The dashed lines indicate that the smaller the WIMP self-annihilation cross section, the larger the WIMP relic density [23]. 10

2.2 Illustration of the three ways to detect dark matter particles [25]. χ represents a dark matter particle and p represents a Standard Model particle. Direction detection looks for the interaction between a dark matter particle and a Standard Model particle. Indirect detection looks for Standard Model particles from the annihilation of two dark matter particles. Collider production is to generate dark matter particles through the collision of Standard Model particles. 13

2.3 Expected WIMP energy spectra in germanium target for ten different WIMP masses with the assumption that the WIMP-nucleon spin-independent cross section is 10^{-45} cm^2. The y-axis is the expected WIMP rate in unit of event·kg^{-1}·day^{-1}·keV^{-1} [42]. 16

2.4 A sensitivity plot for SuperCDMS SNOLAB. The four dashed curves are the expected sensitivities before the experiment, where the red dashed curve is the sensitivity from germanium detectors with the normal bias mode, the light blue dashed curve is the sensitivity from the silicon detectors with the normal bias mode, the dark red dashed curve is the sensitivity from germanium detectors with the high voltage bias mode, the dark blue dashed curve is the sensitivity from the silicon detectors with the high voltage bias mode. The solid curves in the upper right region are exclusion limits from data analyses of many other experiments. The bottom region surrounded by dots is called the neutrino floor, where if an experiment is sensitive enough to reach, the neutrino background would become an unavoidable background in this experiment. 19

3.1 A photo of an iZIP detector, which is photolithographically patterned with ionization and phonon collection sensors interleaved on the same face. 21

3.2 There are four phonon signal readout channels and two ionization signal readout channels in total on each face. Three phonon channels are inside and one is outside as a ring. The inner ionization channel is about the same coverage as the three inner phonon channels and the outer ionization channel interleaves with the outer phonon channel. 22

3.3 When an interaction occurs in the bulk region, electrons and holes migrate to different detector faces after creation due to the external electric field. An interaction that occurs within a few microns of the surface may have both the created electrons and holes drawn to the sensors on the same side. 23

3.4 This plot shows the charge signal asymmetry of surface events and how the iZIP detector discriminate between bulk and surface events. The x-axis is the summed charge energy on side 1 and the y-axis is the summed charge energy on side 2. If an event occurs in the bulk region, it would deposit an equal amount of charge energy on both sides, which makes it distribute along the diagonal (blue dots). If an event occurs near the detector surface, it would have asymmetric charge energy deposited on both sides, which makes it distribute along either the x-axis or the y-axis (red dots). The two dashed blue lines are the boundaries for charge symmetry selection. There is a ^{210}Pb source plate placed above side 1 of this detector, which produces a large amount of surface event on side 1. The 46 keV line comes from the gammas in the ^{210}Pb decay chain. The two blue dots with bigger black circles are two low yield events that pass the charge symmetry selection, which could be used to derive an upper limit on the surface event rejection power of the iZIP detector [46]. . . 25

3.5 These two plots demonstrate the stability of signal collection as a function of time with and without flashing. If the duration of LED light shining is short, e.g. 30 seconds or 1 minute, it is called a mini-flash. The blue dots are from a 12 hour data run with no LED flash performed, while the red dots are from a 9 hour data run with a LED flash once every hour. The data without a LED flash starts to show degradation after three hours. As a comparison, the data with LED mini flashes shows signal stability throughout the whole data collection time. This demonstrates that the LED flash method restores the detectors to their neutral state. The x-axis is the voltage bias time. The y-axis of the top plot is an ionization yield quantity [ygsumINT]. The y-axis of the bottom plot is quantity that describes depth measuring quantity [qzpartOF] based on charge signals from both faces. 26

3.6 Detector interface boards (DIBs) are attached at the sides of a detector and in charge of transferring ionization and phonon signals collected from the sensors out. LEDs are installed on each DIB in order to flash light into the crystal to bring it back to neutral state. 27

3.7 Primary (prompt) phonons are created at the interaction location and scatter isotropically. In this plot, the oblique electrons migrate to the top face and the holes migrate to the bottom face. Neganov-Luke phonons are generated along the charge drift direction in a cone shape. 28

3.8 This is an illustration on how the phonon information gets collected. When phonons reach an aluminum collector, they get absorbed and then break Cooper pairs in it. These quasiparticles then diffuse till reaching the tungsten quasiparticle trap where they get trapped and their energy get transported to a TES. The TES then transfers this energy to a SQUID to read out. 30

3.9 This is a view of the second floor in the cavern of the Soudan mine where the SuperCDMS experiment was located. The surrounding material could become a source of backgrounds. 31

3.10 This photo is to show the assembly of shielding layers near the cryogenic region at Soudan site. 32

3.11 The top plot illustrates the layout of the five iZIP towers in the cryogenic region. The bottom plot illustrates the detector and tower orientations. 34

3.12 The cold end of a stripline connects to a SQUET and the warm end of it connects to the E-box. It transfers the collected signals from the cryogenic region to the room-temperature electronic system. 37

4.1 This plot illustrates the gamma background distribution from ^{133}Ba calibration data in the phonon recoil energy and ionization yield plane for detector iT4Z2 (1111) . Surface electron recoils (blue dots) have yield values less than 1 and spread out from the bulk electron recoil band (green dots) towards low yield region. Among 609776 electron recoil events passing the data quality cuts, two events (red dots) fall into the 2σ nuclear recoil band WIMP search region. 42

4.2 ^{210}Pb undergoes two beta decays to reach ^{210}Po, then decays to the stable ^{206}Pb with the emission of a 5.3 MeV alpha particle. 43

4.3 This illustrates the surface electron recoil rejection capability of the iZIP detector. This detector is iT3Z1, which has a ^{210}Pb source plate above its side 1. Although the surface events (red dots) can have yield values down to the WIMP signal region, nearly 100% of them get excluded by the charge symmetry selection. Of the electron recoils that pass the charge symmetry selection (blue dots), two of them possess low yield values which are close to the yield of nuclear recoils that pass the the charge symmetry selection (green dots). The study with the two source plates demonstrates that an upper limit of the surface electron recoil rejection power of the iZIP detector is at the order of 10^{-5} [46]. 45

4.4 The total ionization energy versus the total phonon energy for WIMP search data taken with SuperCDMS. Alpha particles (pluses) have a signature 5.3 MeV kinetic energy. This is much higher than the energies of most gamma particles (orange and green dots) , which makes it easy to identify. Of greatest interest to the analysis are alpha particles in the inner fiducial volume (red and blue pluses). Alpha particles with their energy deposited in the guard channel or with energy shared between the guard and inner channels (pink and cyan stars) are not considered in this analysis. 46

4.5 The top plot shows a Gaussian fit in the outer charge energy dimension within an inner charge energy bin on the bottom face of detector iT2Z2. From this fit, a mean value and a standard deviation can be calculated. In the bottom plot, linear fits are used for all three data points: mean values, 3σ upper bound, and 3σ lower bound. 48

4.6 The inner alpha background rates (top) and total alpha background rates (bottom) in the iZIP detectors (red dots) compared to the alpha background rate measurements from runs taken with CDMS II (black, green, and magenta dots). Both results show consistent rates with the past measurements. The error bar is in $\pm 1\sigma$. 49

4.7 To reduce the effect on the experiment from the potential cosmogenic neutrons produced by the muons in the cosmic rays faking a dark matter interaction, the SuperCDMS Soudan experiment was located deep underground. Compared to SuperCDMS Soudan, the future SuperCDMS SNOLAB will experience a smaller muon flux by a factor of 10^3 [25]. 51

5.1 Mass fractions of different components in brass of C3604 type [55]. 56

5.2 Neutron emission spectra from a concentration of 1 ppb uranium concentration in C3604 brass. 57

5.3 Neutron emission spectra from a concentration of 1 ppb thorium concentration in C3604 brass. 58

5.4 A screenshot of the variables stored in one of the SuperSim simulation output files in ROOT format. 59

5.5 This is an illustration of the conceptual experiment design for SuperCDMS SNOLAB. 60

5.6 The top plot is a cross section view of the experiment geometry in the simulation. The detector towers (brown circles) are in the center surrounded by space for a potential upgrade (purple). Surrounding the detector volume are the copper cans (red), the active neutron veto layer (grey), the lead layer (black), and the polyethylene layer (dark green). The bottom plot provides a more detailed view of the tower arrangement and composition assumed for this geometry. 61

5.7 In reality, a single scattering neutron should only interact once in a detector. But in data collection, a neutron interacts multiple times within the same detector is not able to be separated from a real single scattering neutron. Thus, these two groups are both parts of single scattering neutrons (Singles) in the data analysis. Neutrons leave signals in more than one detector are referred to as multiple scattering neutrons (Multiples) in the data analysis. 64

5.8 This proposed SuperCDMS SNOLAB experiment would have provided sensitivity to a WIMP-nucleon cross section that would have reached down to 8×10^{-47} cm^2 for a WIMP mass of 50 GeV/c^2 by the end of the planned five-year operating period. This Generation-2 (G2) experiment would have had unparalleled sensitivity for low-mass dark matter, with a sensitivity goal that was 100 times better than the current limits at 13 GeV/c^2, increasing to 6×10^5 times better sensitivity at 1.2 GeV/c^2. (Based on original DOE proposal in 2013 [56]) 67

5.9 Example of one system design considered in this study for a neutron veto in the SuperCDMS SNOLAB experiment. In this study, a configuration with a 225 kg Ge detector payload in 27 towers was investigated. From the inside out, there are 27 detector towers, six copper cans, one Gd-loaded polyethylene layer, one lead layer, one aluminum layer and one polyethylene layer. Silicon photomultipliers were considered as the readout device for the active neutron veto layer. The two pipes connecting to the refrigerator and electronic box are visible on the left and right hand sides of the cryogenic region. 70

5.10 The red curve shows the single-scatter neutron capture efficiency as a function of the energy threshold (E_{th}) in the Gd-loaded polyethylene layer with Birk's law taken into account. The blue curve shows the veto efficiency without implementing Birk's law. These are the single-scatter neutrons from ^{232}Th contamination with an energy deposition in the [10, 100] keV range in a detector. 73

5.11 This is an illustration of the experiment setup with an active neutron veto layer using liquid scintillator. 75

5.12 Single-scatter neutron veto efficiencies in the 0.12% Gd-doped LAB liquid scintillator module as a function of the energy threshold when using different tank materials (titanium (red), stainless steel (blue) and acrylic (green)). An energy collection time window of 100 μs was applied. 77

6.1 This is an illustration of the detector orientation and tower arrangement for the SuperCDMS Soudan experiment. A total of 15 detectors were arranged into 5 towers, each tower containing three detectors. Detector names using two different nomenclatures are listed on each detector. 80

6.2 This is an illustration of the yield-energy distributions for bulk ERs, surface ERs, and NRs in iT1Z1 in the Cf data set. The yield of surface ERs can have any value from 1 down to 0, which covers the yield region of the bulk NRs. Thus, a surface ER can fall into the NR band and mimic a WIMP signal event. 81

6.3 The run time for each data series in Table 6.2 is approximately 3 hours. 85

6.4 The ionization yield [ytNF] vs total phonon energy [ptNF] plane is divided into four regions for statistics comparison. 86

6.5 Statistics comparison among different ^{133}Ba source configurations show that retracting the sources back as far as 4-inches maintains comparable statistics in all four regions. Data series 10 has no data in iT3Z3 due to the existence of abnormal energy χ^2 values. 87

6.6 Distribution comparison between four ^{133}Ba source configurations and the fully-inserted configuration. For the radial charge energy partition quantity on side 1 [qrpart1OF] in region 4, the 1-inch (top left), 2-inches (top right) and 4-inches (bottom left) configurations show comparable statistics to the fully-inserted configuration, while the 8-inches (bottom right) configuration shows an obvious decrease in statistics. 88

6.7 The top left and right plots are examples of a good charge energy χ^2 distribution. The bottom left and right plots are examples of a degraded charge energy χ^2 distribution. QS1OFchisq is the side 1 charge energy χ^2 quantity. qsum1OF is the summed side 1 charge energy. 91

6.8 A Gaussian fit is applied to the χ^2 peak, where QS1OFchisq is the side 1 charge energy χ^2 quantity. The $\mu \pm 3\sigma$ boundaries are compared among three selected data series with good performance. 92

6.9 The ratios of QS1OFChisq (top) and QS2OFChisq (bottom) in run 134 (R134) for all functional charge channels in the 15 detectors. The ratio of a charge energy χ^2 quantity is defined as the random triggered events within a range near the peak over all random triggered events. 93

6.10 A ratio cut is set at 0.7 (i.e. 70%) for iT3Z3 (pink vertical line). 20 data series have QS1OFChisq statistics less than 70 % within [3760, 4440] are removed. QS1OFchisq is the side 1 charge energy χ^2 quantity. The ratio of a charge energy χ^2 quantity is defined as the random triggered events within a range near the peak over all random triggered events. 94

6.11 This plot illustrates the effect of the cGoodRandomChi2_v53_HT cut on the livetime of R133 and R134 WIMP search (lowbg) data. 95

6.12 The top plot is the yield [ytNF] distribution as a function of data collection time for non-zero livetime events (black dots) and zero livetime events (red dots). The bottom plot is yield [ytNF] vs phonon energy [ptNF] plane. Both plots show no difference in the distributions between these two groups of events. 98

6.13 The top plot shows the `livetime` distribution of all events. These two groups of events form a quasi exponential decrease together. The bottom plot illustrates differences in the triggering between non-zero livetime events (blue) and zero livetime events (red). The `TimeBetween` values of the zero livetime events are distributed within the range of those of the non-zero livetime events. `TimeBetween` is a time measurement between two triggers. It equals to the deadtime of DAQ following last event trigger plus the livetime of the current event. 99

7.1 The top plot shows a Gaussian is fit from the NR sample in the yield (`ytNF`) dimension in iT2Z1 using the ^{252}Cf calibration data. The bottom plot shows that a PDF is calculated from the above fit. 110

7.2 The top plot shows a KDE is calculated from the NR sample in the phonon recoil energy (`precoiltNF`) dimension in iT2Z1 using the ^{252}Cf calibration data. The bottom plot shows that a PDF is calculated from the above KDE. 111

7.3 The top plot shows a KDE is calculated to from the bulk ER sample in the yield (`ytNF`) dimension in iT2Z1 using the ^{133}Ba calibration data. The bottom plot shows that a PDF is calculated from the above KDE. 112

7.4 The top plot shows that a KDE is calculated from the bulk ER sample in the phonon recoil energy (`precoiltNF`) dimension in iT2Z1 using the blinded WIMP search data. The bottom plot shows that a PDF is calculated from the above KDE. 113

7.5 The top plot shows a KDE is calculated from the surface event sample in the yield (`ytNF`) dimension in iT2Z1 using the surface event data set. The bottom plot shows that a PDF is calculated from the above KDE. 115

7.6 The top plot shows a KDE is calculated from the surface event sample in the phonon recoil energy (`precoiltNF`) dimension in iT2Z1 using the surface event data set. The bottom plot shows that a PDF is calculated from the above KDE. 116

7.7 Calculated WIMP spectra in Ge target for different WIMP masses [42] with an assumption that the spin-independent WIMP-nucleon cross section is 10^{-45} cm^2. 117

7.8 Combined cut efficiency (red) for the WIMP signal within 15 and 155 keV phonon recoil energy in iT2Z1. 118

7.9 This plot shows the comparison between the WIMP spectrum for a 75 GeV WIMP in iT2Z1 after taking the efficiency into account (red) and the WIMP spectrum from theoretical calculation (green) 119

7.10 This plot shows the generation of WIMP signal PDF (red) from the efficiency-corrected WIMP spectrum in iT2Z1 for a 75 GeV WIMP between 20 and 150 keV phonon recoil energy with the assumption of σ_{SI}=10^{-45} cm^2. 119

7.11 This plot shows a linear relation between the measured signal numbers (Ns_measured) and the input signal numbers (Ns_input) for a 25 GeV WIMP. For each input signal number, 80 pseudo data sets are generated to test the model. 128

7.12 This plot shows the scan of a signal event number (Ns) upper limit in a pseudo experiment at a 90% confidence level for a 25 GeV WIMP with the assumption of σ_{SI}=10^{-45} cm^2. 129

7.13 This plot shows the exclusion limit of this high mass WIMP search analysis from the profile likelihood ratio technique (dark red curve). A WIMP-nucleon spin-independent cross section of 1.32 $\times 10^{-44}$ cm^2 with a WIMP mass of 75 GeV/c^2 at 90% confidence level is reached. The shaded area between 25 and 750 GeV/c^2 WIMP masses is the sensitivity with 2σ uncertainties from the profile likelihood ratio technique. The exclusion limit is consistent with the sensitivity estimation before unblinding. The curve in orange is the CDMS-Edelweiss combined limit. The short curve in dark red at the top left is the limit from SuperCDMS Soudan Low-mass WIMP search analysis. The curve in light green is the limit from PICO-60. The curve in magenta is the limit from DarkSide-50. The curve in green is the limit from XENON100. 130

A.1 Neutron emission spectra from uranium (top) and thorium (bottom) in Carbon Fiber Rod 137

A.2 Neutron emission spectra from uranium (top) and thorium (bottom) in Kapton 139

A.3 Neutron emission spectra from uranium (top) and thorium (bottom) in MuMetal. 141

A.4 Neutron emission spectra from uranium (top) and thorium (bottom) in shotcrete at SNOLAB. 143

C.1 Example of a standard normal distribution. The colored area corresponds to the distribution within $\pm 1\sigma$. 152

C.2 Example of Poisson distributions with different expected values ν in histograms. In comparison, the continuous curves are Gaussian distributions with $\mu = \nu$ and $\sigma = \sqrt{\nu}$. 153

LIST OF TABLES

Table Page

3.1 Dimensions of each shielding layer at SuperCDMS Soudan. 35

3.2 List of selected RQs. `T[1-5]` refers to tower 1 through 5. `[16-25]` refers to information of 10 triggers. `[20]` refers to the global trigger. `[16-19]` refers to the four triggers before the global trigger. `[21-25]` refers to the five triggers after the global trigger. `[ch]` = AS1, BS1, CS1, DS1, AS2, BS2, CS2, DS2, or T, S1, S2 (see Fig. 3.2). `[n]` refers to the relative height of a pulse, which can be 10, 20, 40, 50, 70, 80, 100. `S[1/2]` refers to side 1 or side 2. 38

3.3 List of selected RRQs. `[i/o]` refers to inner or outer channel. `[1/2]` refers to side 1 or side 2. 39

4.1 Listed are the inner and total alpha background rates for the seven best performing detectors. 47

5.1 The material and mass of the shielding layers in Fig. 5.6. 62

5.2 The radioactive level of each contaminant in each material. 62

5.3 Estimated single scatter NR and ER rates in different energy ranges for Ge and Si detectors separately. 65

5.4 Estimated single scatter NR and ER rates in different energy ranges for a combined payload of 178.784 kg. 65

5.5 Estimated numbers of single-scatter NR and ER events in different energy ranges for an experiment exposure of 385 kg-years. 66

5.6 Estimated neutron event number at SuperCDMS SNOLAB with the assumption of a ∼244 kg-years net exposure and an 8-48 keVr WIMP search range [56]. 68

5.7 The dimensions of each shielding layer. 69

5.8 Radioactivities of each contaminant considered in each material. 71

5.9 NR, ER selection rules in detectors. 71

5.10 NR, ER and single-scatter NR, ER rate ranges in the detectors. 72

5.11 The total NR and single-scatter NR rates in the detectors from the contaminants in stainless steel, titanium, and acrylic. Natural uranium consists of ∼99.3% ^{238}U and ∼0.7% ^{235}U. 76

6.1 Summary of the cuts required to blind the conventional WIMP search data [63]. 82

6.2 Stats and configuration of each examined data series. 85

6.3 The division of four regions in the ionization yield vs phonon energy plane. 86

6.4 Detector livetime after the application of the `cGoodRandomChi2_v53_HT` cut on the R133 WIMP search data. 92

6.5 Detector livetime after the application of the `cGoodRandomChi2_v53_HT` cut on the R134 WIMP search data. 94

6.6 The fractions of zero livetime events in some example Ba data sets. 97

6.7 The fractions of zero livetime events in WIMP search (WS), Ba and Cf data, calculated for data runs 133 and 134. 100

6.8 The definition of each bit information in `T*TGMask##` RQ. 102

6.9 Numbers of real zero livetime events without TrigEnable bits found. For R133 WIMP search data, 155236 events with no TrigEnable bits found occur in five out of 39 data series taken between 2012/07/31 and 2012/08/14. There were many tests taking place onsite in this period. Thus, these five data series were removed entirely. This leaves only seven events in the remaining R133 WIMP search data with no TrigEnable bits found. 103

6.10 The corrected livetime for each data set. 104

7.1 Shorts that prevent these five detectors to be included in the final high mass WIMP search analysis. 106

7.2 The ten best performing detectors selected for the high mass WIMP search analysis. 106

7.3 Special notes for some good detectors being selected in the high mass WIMP search analysis. 107

7.4 Mass and livetime information of the ten best performing detectors in the high mass WIMP search analysis. 125

7.5 Expected WIMP number in each detector between 20 and 150 keV recoil energy after efficiency correction in each detector for three studied WIMP masses with the assumption of σ_{SI}=10^{-45} cm^2. 125

7.6 The mean number of each background in each detector for pseudo data generation after compensating for the blinding region in the bg-permitted data. 127

A.1 Information about Carbon Fiber Rod. 136

A.2 Neutron Yield in Carbon Fiber Rod (see Fig. A.1). 136

A.3 Information about Kapton. 138

A.4 Neutron Yield in Kapton (see Fig. A.2). 138

A.5 Components of MuMetal with a density of 8.747 g/cm^3. 140

A.6 Neutron Yield in MuMetal (see Fig. A.3). 140

A.7 Components of Shotcrete with a density of 2.30 g/cm^3 [76]. 142

A.8 Neutron Yield in shotcrete (see Fig. A.4). 142

B.1 A summary guide to cut tables. 144

B.2 Individual Cuts in `cGoodEv_v53` umbrella cut. 145

B.3 Individual Cuts in `cLiveTime_v53_HT` umbrella cut (continue in the next page). 146

B.4 Individual Cuts in `cLiveTime_v53_HT` umbrella cut. 147

B.5 Individual Cuts in parallel with `cGoodEv_v53` and `cLiveTime_v53_HT` umbrella cuts. 147

B.6 List of pre-selection cuts. 148

B.7 List of Ionization Fiducial Volume cuts. 148

B.8 Nuclear Recoil Event Selection cut. 149

B.9 Veto cut. 149

B.10 Single Scattering Event Selection cut. 149

This dissertation is lovingly dedicated to my parents, Rong-Sen Qiu and Fu-Ying Li, my elder brother, Yu Qiu, and my nephew, Sheng-Ting Qiu.

Chapter 1

Existence of Dark Matter

1.1. Invisible Mass in the Coma Cluster

In the 1920s and 1930s, observations based on luminosities and internal rotations were the usual ways to estimate the masses of nebulae. There were two factors that made these methods unreliable. Firstly, the observed luminosity of an extragalactic system could be used to estimate only the visible mass in that system. If there was any invisible mass, the estimation of the mass was only a lower limit of that entire galactic system. Secondly, the observed internal rotation of an extragalactic system was under the assumption that the internal part of this system rotated like a solid body. But in fact, the internal part was not a huge core of mass. Many nebulae were distributed within the system. There was a non-zero viscosity caused by the gravitational interactions among its component masses that made this central core move like a solid body.

In 1933, Fritz Zwicky, who was a Swiss astronomer and worked at the California Institute of Technology in the United States of America, studied the Coma cluster and performed a calculation to estimate its total mass [1, 2]. He made an assumption that the Coma cluster was a mechanically stationary system. In this case, the total mass of the Coma cluster could be estimated using the virial theorem.

After a series of derivation, he arrived at the following expression

$$\mathcal{M} \geq \frac{3R\bar{v_s^2}}{5G} \tag{1.1}$$

where R was the radius of the Coma cluster of nebulae and its value was 2×10^6 light-years, $\bar{v_s^2}$ was an average of the average velocity squared along the line of sight and its value was approximately 5×10^{15} cm^2 sec^{-2}, G was the gravitational constant and the "$\geq$" sign came from the fact that the bright nebulae were not distributed uniformly in the Coma cluster.

After he put these values in the formula, he estimated the total mass of the Coma cluster of nebulae $\mathcal{M}$ to be greater than $4.5 \times 10^{13} M_\odot$, where $M_\odot$ is the mass of the sun. The Coma cluster contained about one thousand nebulae. Thus, the average mass of a nebulae was calculated as

$$\bar{M} \geq 4.5 \times 10^{10} M_\odot \tag{1.2}$$

This estimate should be a lower limit for the average mass of a nebulae. However, the observed luminosity gave the average mass of a nebulae to be only $8.5 \times 10^7 M_\odot$. Thus, this result was really surprising and unexpected. Based on the observation of the luminosity only, the discrepancy in the mass estimation was about a factor of 500. From this Zwicky concluded that the total mass of the Coma cluster was dominated by nonluminous matter, which he named dark matter.

1.2. Evidence of Dark Matter

Starting from 1960s the equipment for astronomical observations and measurements improved significantly. Studies of the rotational curves of galaxies improved estimates of the amount of dark matter in the universe and further supported the idea that in addition to luminous matter, there were large amounts of nonluminous mass in these galaxies. This nonluminous mass can have gravitational effect on the space-time nearby. By studying this effect through gravitational lensing, the result indicated that a massive dark matter component should exist in these galaxies. One of these studies was the observation of the Bullet Cluster, which lead to a constraint on the self-interaction cross section between dark matter particles.

1.2.1. Rotational Curves of Galaxies

In the late 1960s and early 1970s, Vera Rubin made measurements of the rotational velocities of the Andromeda nebulae (M31) within the range of 3 kpc to 24 kpc from its nucleus [3]. She found that the rotational velocities dropped slower than expected at large galaxy radii (see Fig. 1.1). According to Newtonian dynamics, based only on the luminous matter in the galaxy, the rotational velocities should decrease at a rate of $\frac{1}{r^2}$ as the distance from the luminous core increases. Thus, without the existence of a large amount of nonluminous matter, the galaxy would be torn apart as it rotates.

1.2.2. The Bullet Cluster

If general relativity is valid, when there exists an amount of matter between a light source and an observer, the paths of the light would be bent as it travels from the source towards the observer due to the warped space-time around this amount of matter. The image of the source will be displaced. This effect is called gravitational lensing. By examining the bending of light propagation, the mass of this amount of matter can be estimated.

If a cluster consists of both luminous and nonluminous matter, the amount of nonluminous matter in the total mass can be determined by observing the nonluminous matter via the gravitational lensing effect and the luminous matter via the electromagnetic measurement. This combination of observation methods was used in the study of the Bullet Cluster.

A hot main cluster and a relatively cold subcluster are involved in the Bullet Cluster, 1E0657-56 [5]. After the galaxies collided, the centroid of the hot X-ray gas cloud were identified by x-ray measurements made by the Chandra telescope and the centroid of the nonluminous matter was identified from a gravitational lensing analysis. These centroids were offset as illustrated in Fig. 1.2. If dark matter does not exist, the majority of the mass is expected to be in the hot X-ray gas cloud. However, the observation indicated that only

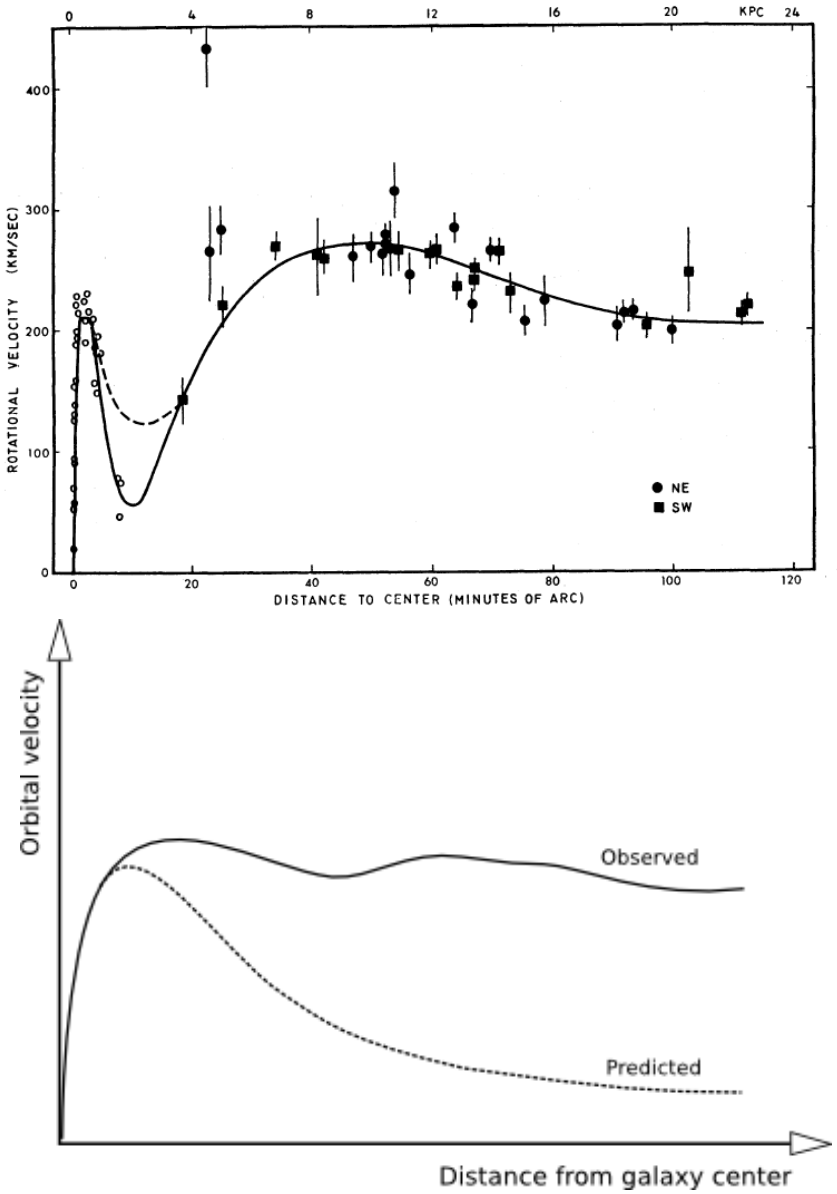

Figure 1.1: (Top plot) Rotational velocity (unit: km/s) in M31 as a function of the distance (unit: minutes of arc) from its center. At a distance of 690 kpc for M31, 1 minute of arc (1') is equal to a distance of 200 pc. The most distant region observed was at 120' (24 kpc). The solid curve is the fitted rotation curve [3]. (Bottom plot) The solid curve is from observation of a galaxy whose rotation curve is flat at large distance. The dashed curve is a prediction based on calculations using Newtonian dynamics [4].

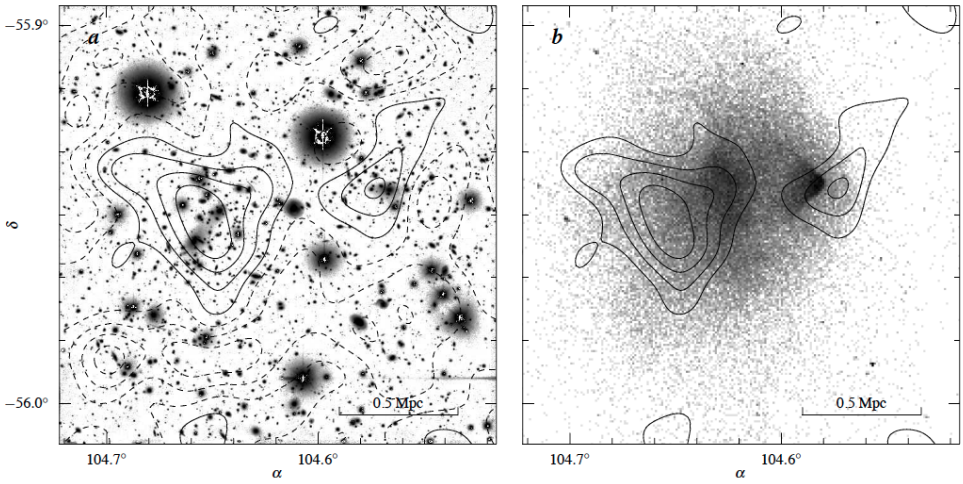

Figure 1.2: (a) Contours of the weak gravitational lensing mass overlay on the optical image of 1E0657-56. Dashed curves are negative relative to an arbitrary zero level. (b) Contours of the upper four mass levels (for clarity purpose) overlay on the X-ray image. Gravitational potential of the X-ray gas can be derived from its temperature measurement. After the collision, the gas lags behind the dark matter subcluster [5].

a fraction of 10% -15% of mass was in the form of hot gas or plasmas, which indicated that the majority of the mass is dark matter.

This observation not only provides evidence for the existence of dark matter, but also sets an upper limit for the strength of dark matter self-interaction. When passing through the main cluster, the subcluster's velocity decreases from 4500 km/s (theoretical calculation) to 3500 km/s (at the time when the observation takes place). Dark matter particles are relatively collisionless. Assuming the drag force comes from the dark matter particle collisions only, a constraint can be set for the dark matter self-interaction

$$\frac{\sigma}{m} < 1\ \mathrm{cm}^2 \cdot \mathrm{g}^{-1} \tag{1.3}$$

where σ is the cross section for the dark matter self-interaction, and m is the mass of the dark matter particle.

1.3. Dark Matter Component in the Universe

The cosmic microwave background (CMB) radiation [6] is photons produced during the recombination era when the universe cooled down. Their wavelengths are in the microwave region now and the CMB is nearly uniform in density across the universe (see Fig. 1.3). From measurements of the CMB, the shape of the universe can be deduced. The inflation model [7] can be used to describe the near-uniformity of CMB from which the curvature of the universe could be derived. This curvature is determined by the density of the universe, which could tell us how much matter is needed to construct such a universe with uniform CMB.

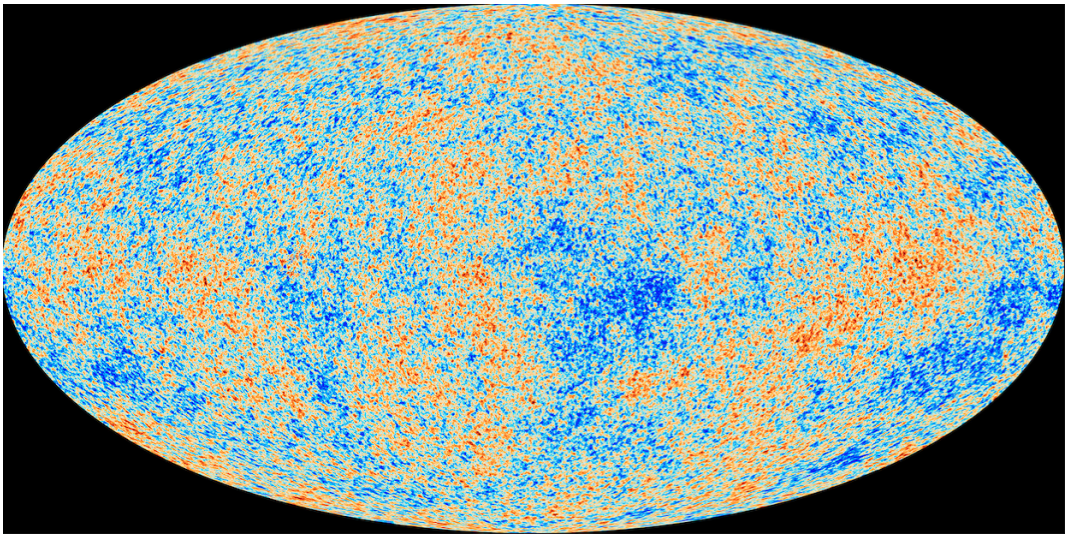

Figure 1.3: The anisotropies of the cosmic microwave background (CMB) as observed by Planck. The CMB is a snapshot of the oldest light in our universe, imprinted on the sky when the universe was just 380 000 years old. It shows tiny temperature fluctuations that correspond to regions of slightly different densities, representing the seeds of all future structure: the stars and galaxies of today. *Copyright: ESA and the Planck Collaboration [8].*

Measurements taken by the *Planck* satellite launched by the European Space Agency (ESA) indicate that the curvature of the universe is flat [9] as predicted by the model of inflation. In order for the universe to be flat more components than the baryonic matter are needed. Results from the analysis of data taken by the *Planck* satellite indicate that

ordinary matter only contributes 4.9% of the total universe mass, dark matter contributes 26.8%, and dark energy contributes 68.3%. Over 85% of matter is dark matter which is non-baryonic dominant and cold (moving at non-relativistic speeds) [10–12].

1.4. Dark Matter Particle Candidates

If dark matter exists, there must be as least one type of dark matter particle. In order for a particle to be considered as a "good" dark matter particle candidate, it must meet the following criteria [13].

1. Electric neutral
2. Non-relativistic
3. Support the hierarchic star formation process [14]
4. Compatible constraints on self-interaction
5. Provide the appropriate relic density [15]
6. Experimentally detectable
7. Consistent with the results from current direct dark matter searches
8. Compatible with other astrophysical bounds

Although the term "dark matter" had been introduced into the physics field for over 80 years, its composition is still a mystery. Below is a brief introduction to some favored dark matter candidates [15].

Neutralinos are one type of Weakly Interacting Massive Particles (WIMPs) that results from supersymmetric models of particle physics [16, 17]. If neutralinos are dark matter, two physics problems can be solved simultaneously because they can not only help to explain the problem of the nonluminous mass in the universe, but also prove the existence of supersymmetry.

Extra Dimensional Dark Matter was first proposed by Kaluza and Klein back in 1920s [18]. If this type of dark matter does exist, it would live in a higher dimensional space, i.e. a fourth spatial dimension in this case. This extra dimension is too small to directly explore experimentally. Only the effect of its projections in our universe may be observed. Thus, an observation of multiple particles sharing different masses but same charge might shed a light on this. If this candidate does exist, it could also support the idea of String Theory [19, 20].

Axions were motivated to solve the strong CP violation problem and first proposed by physicists Roberto Peccei and Helen Quinn back in 1977 [21]. They are weakly interacting but extremely light in mass at the order of 10^{-6} eV.

Sterile Neutrinos were proposed as a 4th generation of neutrinos [22]. In the Standard Model, neutrinos do not have right-handed fields. The flavor oscillation and mixing suggests the incompleteness of the Standard Model of particle physics. Sterile neutrinos are a cold dark matter candidate. Unfortunately, they would be very difficult to detect because the time for sterile neutrinos to interact with ordinary matter is about the age of the universe.

Chapter 2

Weakly Interacting Massive Particles

Weakly Interacting Massive Particles (WIMPs) are among the most promising dark matter candidates. A WIMP self-annihilation cross section at the weakly interacting scale can naturally provide the right abundance for the WIMP relic density, which makes WIMPs compelling. The Super Cryogenic Dark Matter Search (SuperCDMS) experiment is one of the leading direct dark matter search experiments across the world that search for WIMPs.

2.1. The WIMP Miracle

During the radiation era, a WIMP could interact with another WIMP to produce a pair of Standard Model particles at a high rate, and vice versa. Thus, the production and annihilation rates were in thermal-dynamic equilibrium. As the universe expanded, the number density of WIMPs dropped. Although WIMPs and the Standard Model particles were still in equilibrium, the production and annihilation rates decreased. As the expansion continued, eventually the number density of WIMPs dropped so low that there was little chance for two WIMPs to meet and interact with each other. This time point is commonly referred to as freeze-out. Once this occurred, there was negligible WIMP self-annihilation and a relic density of WIMPs remained in the universe.

If n is the WIMP number density, s is the entropy density, t is time, $\langle \sigma_{\text{ann}} v \rangle$ is the thermal average of WIMP self-annihilation cross section, n_{eq} is the equilibrium WIMP number density, m is the WIMP mass and H is the Hubble parameter, then the Boltzmann equation

and entropy conservation give the following equations [15]

$$\begin{aligned} \frac{dn}{dt} &= -3Hn - \langle\sigma_{\rm ann} v\rangle (n^2 - n_{\rm eq}^2) \\ \frac{ds}{dt} &= -3Hs \end{aligned} \tag{2.1}$$

If we let $Y = n/s$ and $x = m/T$, then the relation between Y and x can be derived from the above equations. This relationship is illustrated in Fig. 2.1. The smaller the WIMP self-annihilation cross section, the larger the WIMP relic density.

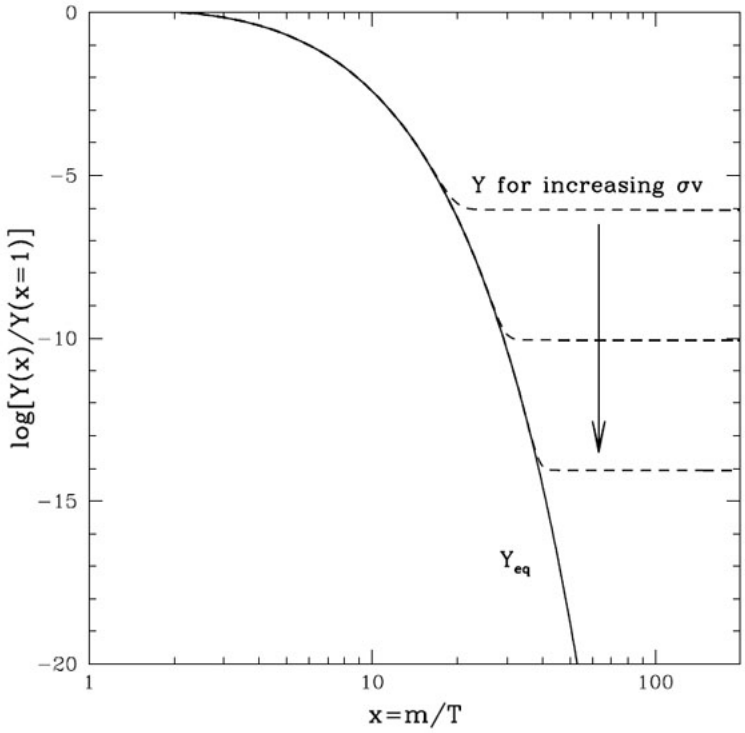

Figure 2.1: This plot shows the WIMP number density during the freeze-out stage in the pre-BBN era in a form of Y(x)/Y(x+1) as a function of x=m/T where Y=n/s (solid line). The dashed lines indicate that the smaller the WIMP self-annihilation cross section, the larger the WIMP relic density [23].

The freeze-out temperature is $T_{\rm fo} \sim m/20$. Big bang nucleosynthesis (BBN) started about 200 s after the big bang. At that point in time, the temperature was about 0.8 MeV. This means that if the WIMP mass is larger than ∼20 MeV, the WIMP relic density would

be determined before the BBN. At the present day, the relic density is believed to be [15]

$$\Omega h^2 \approx \frac{3 \times 10^{-27}\ \mathrm{cm}^3 \cdot \mathrm{s}^{-1}}{\langle \sigma_{\mathrm{ann}} v \rangle} \tag{2.2}$$

If the WIMP self-annihilation cross section is at the weakly interacting scale, then it gives the right abundance for a $\sim$100 GeV/c^2 scale WIMP. The present estimation for the WIMP mass ranges from the order of GeV/c^2 to a few TeV/c^2. This also implies that the freeze-out happened in the pre-BBN era.

2.2. The Lightest Neutralino

In the minimal supersymmetric standard model (MSSM) [24], there is a discrete symmetry called R-parity. It is conserved and is defined as

$$R = (-1)^{3B+L+2s}$$

where B is the baryon number, L is the lepton number, and s is the spin of the particle. All the known Standard Model particles have the value of $R = 1$, while the supersymmetric (SUSY) particles [16] have the value of $R = -1$ resulting from the condition that the spin difference between a Standard Model particle and its superpartner is $\frac{1}{2}$.

From the conservation of R-parity, the SUSY particles can either be produced in pairs or annihilate in pairs. When a heavier SUSY particle decays, it can only decay to a lighter SUSY particle. Thus, the lightest SUSY particle (LSP) is stable since there is no lighter SUSY particle and it cannot decay further. For these reasons, the LSP is the canonical and best-investigated supersymmetric WIMP candidate.

The neutralino is the most favored LSP. There are four kinds of neutralinos in the MSSM. Each neutralino, χ, is a linear combination of four superparticles.

$$\chi = \alpha\tilde{B} + \beta\tilde{W}^3 + \gamma\tilde{H}_1 + \delta\tilde{H}_2$$

where $\tilde{B}$ is the bino, $\tilde{W}^3$ is the neutral wino, $\tilde{H}_1$ and $\tilde{H}_2$ are two neutral Higgsinos. α, β, γ and δ are the mixing coefficients. Depending on the values of α, β, γ and δ, the lightest neutralino can be bino-like, wino-like or higgsino-like.

2.3. Dark Matter Detection Methods

The true identity of dark matter is still an enigma and the development of experiments and approaches to uncover it is ongoing. Dark matter does not interact through the electromagnetic and strong forces with ordinary matter, but it does have a gravitational effect on the surroundings and may be able to interact weakly with ordinary matter. The interaction cross section between dark matter and normal matter is fairly small. Thus, experiments must be designed with great sensitivity to rare interactions between dark matter and ordinary matter.

In principle, there are three distinct methods to detect dark matter particles: direct detection, indirect detection, and collider production. Although they are distinct from each other, their ultimate goal is the same: to discover the identity and understand the characteristics of this mysterious component of the universe. Figure 2.2 illustrates the physics processes used in these three different detection methods.

a) Direct Detection

The direct detection method [26] examines the interactions between dark matter particles (χ) and ordinary particles (p) via the weak interaction. This interaction type is illustrated in Fig. 2.2 as

$$\chi + p \rightarrow \chi + p$$

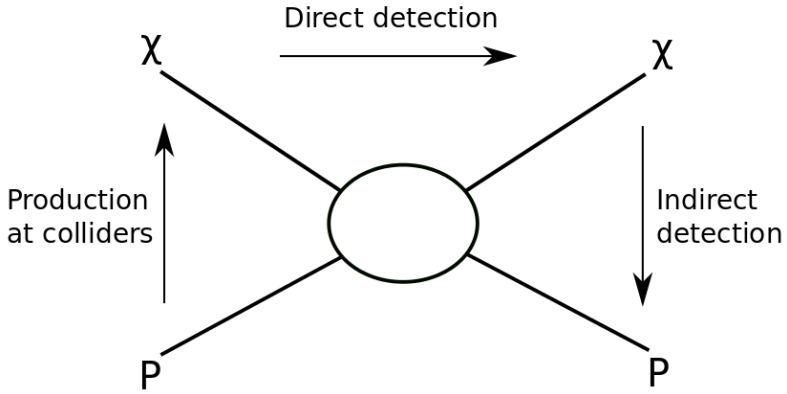

Figure 2.2: Illustration of the three ways to detect dark matter particles [25]. χ represents a dark matter particle and p represents a Standard Model particle. Direction detection looks for the interaction between a dark matter particle and a Standard Model particle. Indirect detection looks for Standard Model particles from the annihilation of two dark matter particles. Collider production is to generate dark matter particles through the collision of Standard Model particles.

In the direct detection technique, the energy from a dark matter particle collision with a target is measured directly [26, 27]. This technique uses low-background terrestrial targets. By scattering off the nuclei in the target, the dark matter particle would leave signatures such as ionization, phonon or scintillation signals from the recoiling nucleus. SuperCDMS [28], Edelweiss [29], LUX [30], XENON [31], CRESST [32] are some examples of the direct detection experiments around the world.

b) Indirect Detection

Indirect dark matter searches [26, 33] look for the annihilation products from two dark matter particles interacting with each other. This interaction type is illustrated in Fig. 2.2 as

$$\chi + \chi \rightarrow p + p$$

There are areas in the universe where dark matter particles can exist in high densities such as the center of a galaxy. If dark matter particles could annihilate with each other in the early universe, they can still annihilate with each other today. The goal of indirect detection

techniques is to detect these products (gamma rays, neutrinos, etc.) of dark matter particle pair annihilations. Fermi-LAT [34], AMS [35], HESS [36] and IceCube [37] are some examples of the current running indirect detection experiments around the world.

c) Collider Production

To search for dark matter particles at a collider, researches sift through the products of Standard Model particle collisions for signatures of dark matter production [38]. Although this interaction type is illustrated as $p + p \rightarrow \chi + \chi$ in Fig. 2.2, a more accurate illustration would be

$$p + p \rightarrow \chi + \chi + p\prime + p\prime + p\prime + \cdots$$

because there are many Standard Model particles ($p\prime$) produced during these same collisions. Since the produced dark matter particles leave no direct signal in the detectors, their existence is inferred from the missing energy of other interaction products observed. ATLAS [39] and CMS [40] at the Large Hadron Collider are two of the detectors that are searching for dark matter through Standard Model particle collisions.

2.4. Direct Detection Event Rates

Although there are three detection methods, this dissertation will focus only on the dark matter direct detection. The feasibility of using a terrestrial detector to detect the direct interaction between dark matter particles and Standard Model particles was investigated by Mark Goodman and Edward Witten in the 1980s [41]. At that time, a neutral-current neutrino detector was just proposed. They immediately saw the possibility to use it to detect dark matter candidates in the galactic halo.

Assuming the mass of a dark matter candidate is M_{WIMP}, the local dark matter density is ρ_0, the mean velocity of dark matter is $\langle v \rangle$, the atomic weight of the target atom is A, the elastic scattering cross section between this dark matter candidate and the target atom is σ,

the counting rate of this dark matter candidate was derived as

$$R = \frac{5.8\,\text{events}}{\text{kg day}}[\frac{\bar{\sigma}}{10^{-38}\,\text{cm}^2}][\frac{\rho}{10^{-24}\,\text{g/cm}^3}][\frac{v}{200\,\text{km/sec}}] \tag{2.3}$$

where $\bar{\sigma} = (\sigma/A)(1\ \text{GeV/m})$. In order to estimate the rate of a particular dark matter particle on a specific target, σ needs input from nuclear physics, and ρ, $\langle v\rangle$ need inputs from astrophysics. From Equation 2.3, three different types of dark matter candidates were considered: particles with coherent weak interactions, particles with spin-dependent interactions, and strongly interacting particles.

The WIMP-nuclei elastic scattering differential rate [42, 43] can be written as

$$\frac{dR}{dE_R} = N_N \frac{\rho_0}{M_{\text{WIMP}}} \int_{v_{min}}^{v_{max}} d\mathbf{v} f(\mathbf{v}) v \frac{d\sigma}{dE_R} \tag{2.4}$$

where $N_N = N_A/A$ is the number density of the target nuclei, N_A is the Avogadro number, $f(\mathbf{v})$ is the WIMP velocity distribution, E_R is the transfer energy from WIMP to the recoiling nucleus. Assuming a WIMP with a mass of M_{WIMP}=100 GeV/c^2 and using the inputs of the mean WIMP velocity $\langle v\rangle$=220 km/s, the galactic halo escape velocity $v_{esc} \approx 544$ km/s and the local WIMP density $\rho_0 = 0.3$ GeV/cm^3, the elastic scattering cross section $\sigma \sim 10^{-38}$ cm^2 for electroweak WIMP-nucleus interactions from particle physics, the expected WIMP event rate can be expressed as

$$R \sim N_N \times \phi_0 \times \sigma = \frac{N_A}{A} \times \frac{\rho_0}{M_{\text{WIMP}}} \times \langle v\rangle \times \sigma \sim 0.13\,\text{events kg}^{-1} \cdot \text{year}^{-1} \tag{2.5}$$

This can also be written as

$$R \sim 0.13\,\frac{\text{events}}{\text{kg year}}\,[\frac{A}{100} \times \frac{\sigma}{10^{-38}\,\text{cm}^2} \times \frac{\langle v\rangle}{220\,\text{km s}^{-1}} \times \frac{\rho_0}{0.3\,\text{GeV cm}^{-3}}] \tag{2.6}$$

Equation 2.6 shows that different WIMP interaction rates are expected between WIMPs and detectors that use different target materials. The higher the atomic number of the target

atom, the higher the WIMP-nucleon interaction rate. For WIMPs with low masses, it is much harder for them to cause nuclei with high atomic numbers to recoil. Thus, a target with a low atomic number and a low energy threshold would be more sensitive to low-mass WIMP search.

2.5. Three Key Points to a Direct Detection Experiment

In order to increase the probability to detect dark matter interaction signals, one needs to improve detector performance and experiment design. Generally speaking, there are many aspects and details that need to be addressed when operating an experiment in this field. Among all of these aspects, three key aspects affect the experiment sensitivity most, which are energy threshold, exposure and background rates [27].

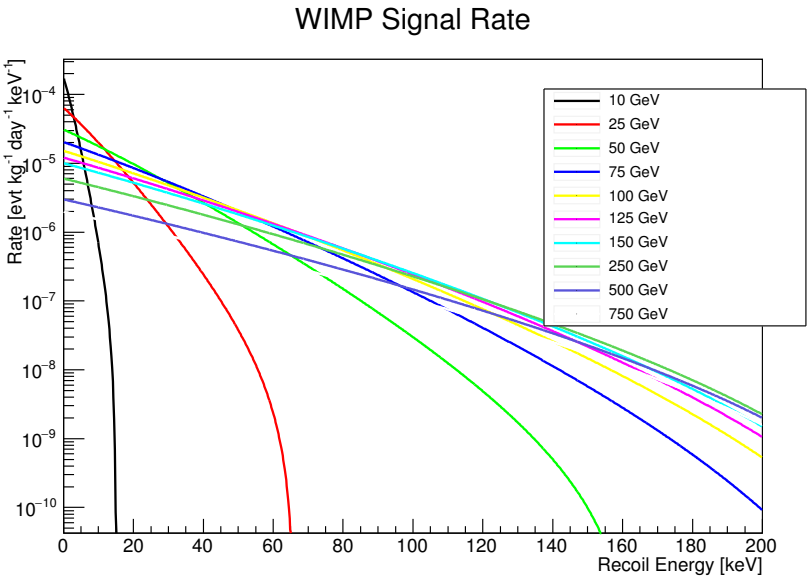

Figure 2.3: Expected WIMP energy spectra in germanium target for ten different WIMP masses with the assumption that the WIMP-nucleon spin-independent cross section is 10^{-45} cm^2. The y-axis is the expected WIMP rate in unit of event·kg^{-1}·day^{-1}·keV^{-1} [42].

The first key aspect to consider is the energy threshold. Because the expected WIMP energy spectrum [42] is quasi-exponentially decreasing with recoil energy (see Fig. 2.3), pushing the energy threshold of the detectors lower means increasing WIMP interaction rate

in the detectors exponentially. But the energy threshold of an experiment is often limited by the electronic system and noise around the detectors. When a detector goes down to a lower energy threshold, it picks up more noise and the fraction of good signal candidates is reduced. In experiments like SuperCDMS, detectors are cooled to $\sim$50 mK in order to reduce the thermal noise. In addition to thermal noise, the electronic readout system also has intrinsic noise. Development of cryogenic and electronic readout systems are a key part in making sensitivity improvements for this type of dark matter detector.

The second key aspect is the exposure of the experiment, which is a measure of how much effective data an experiment has for detecting dark matter. It is an input to the calculation of the expected sensitivity of an experiment and it is defined as the target mass times the good data collection time.

$$\text{Exposure [kg·day]} \;=\; \text{Mass [kg]} \;\times\; \text{Time [day]}$$

where *kg* is used as the unit of mass and *day* is used as the unit of time in most experiments in this field. The higher the exposure, the higher the probability for a WIMP-nucleon interaction to occur in the detectors. In order to increase exposure, an experiment can use target with a higher atomic number, increase the dimension of a target, use multiple targets, take longer WIMP search data collection, or a combination of them.

The third key point is the background event rates. When a detector is built to detect WIMPs, it is designed to detect the elastic collision signal between a WIMP and a nucleon in the detector. During an elastic collision, some amount of kinetic energy is transferred from the incident WIMP to a nucleon to make it recoil in the detector. Unfortunately, when a neutron, which is one of the background event types, interacts with a nucleon in the detector via an elastic collision, it can produce a signal that is indistinguishable from a WIMP-nucleon interaction. If this nuclear recoil event falls into the WIMP signal region

of an experiment, it may be misclassified as a WIMP signal. In addition to neutrons, there are several other background event types that can exist in a direct dark matter detection experiment. Thus, to understand and reduce backgrounds in an experiment is crucial.

2.6. Experiment Sensitivity

Sensitivity is an estimation of the ability of an experiment to probe the dark matter detection parameter space before conducting the experiment. Figure 2.4 is a sensitivity plot for SuperCDMS SNOLAB, which is expected to be operational in 2020. The dashed curves are the expected sensitivities on the spin-independent WIMP-nucleon cross section. From Section 2.4 we know that the expected WIMP event rate R is in unit of $\mathrm{kg}^{-1}\cdot\mathrm{day}^{-1}$, which means that with more exposure, there are more WIMPs expected to interact with the detector material. The sensitivity depends linearly on the exposure in all mass ranges until the experiment becomes limited by irreducible backgrounds.

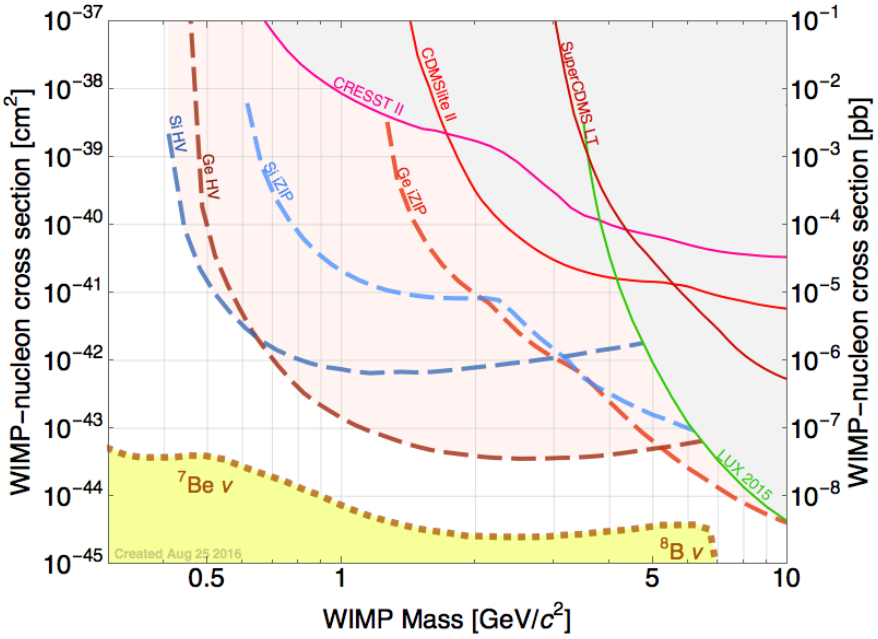

Figure 2.4: A sensitivity plot for SuperCDMS SNOLAB. The four dashed curves are the expected sensitivities before the experiment, where the red dashed curve is the sensitivity from germanium detectors with the normal bias mode, the light blue dashed curve is the sensitivity from the silicon detectors with the normal bias mode, the dark red dashed curve is the sensitivity from germanium detectors with the high voltage bias mode, the dark blue dashed curve is the sensitivity from the silicon detectors with the high voltage bias mode. The solid curves in the upper right region are exclusion limits from data analyses of many other experiments. The bottom region surrounded by dots is called the neutrino floor, where if an experiment is sensitive enough to reach, the neutrino background would become an unavoidable background in this experiment.

Chapter 3

SuperCDMS

This dissertation will focus on the direct dark matter search field and specifically the SuperCDMS experiment within this field. The SuperCDMS Soudan experiment was located and operated in the Soudan Underground Laboratory in northern Minnesota. The laboratory is below the surface at a depth of 2000 meter water equivalent (or mwe), which makes it well shadowed from cosmic rays. It started operation in March 2012 and it was decommissioned in December 2015. SuperCDMS focuses mainly on detecting the WIMP-nucleon interaction. Semiconductor crystals were operated in a very low temperature environment in order to detect the interaction between a WIMP and an ordinary nucleus. By measuring both the ionization and phonon signals of an interaction, the interleaved Z-dependent Ionization and Phonon (iZIP) detector provides a possibility for SuperCDMS to identify WIMPs from its interaction with the terrestrial target.

The next stage of SuperCDMS will be located and operated in the SNOLAB laboratory that is located in Sudbury, Ontario, Canada. SNOLAB is below the surface at a depth of 6000 mwe, which is as three times deep as Soudan. The overburden enhances the ability to reduce cosmic rays that can generate cosmogenic backgrounds in the experiment setup by a factor of 1000. The experiment is scheduled to begin its first science running in 2020.

3.1. iZIP Detectors

The iZIP detector used in SuperCDMS Soudan was made from germanium crystal (cylindrical shape, 3 inches in diameter, 1 inch in thickness, ∼0.6 kg per detector, see Fig. 3.1). It was photolithographically patterned with ionization and phonon collection sensors interleaved on both the top and bottom faces. With the charge signals being read out from both

sides, a physics quantity can be constructed to reflect the depth information of an interaction in the detector. This feature provides the iZIP detector a superior ability to reject surface background events compared to the previous CDMS II detector that only had ionization sensors on one side.

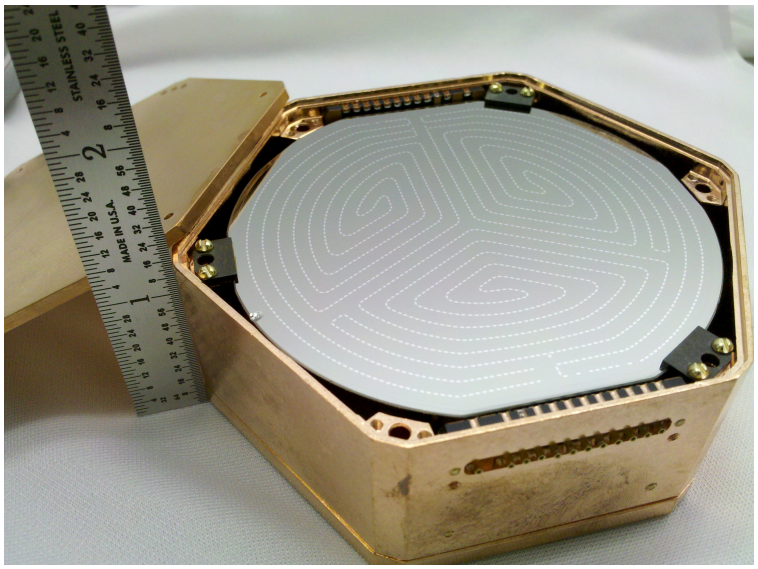

Figure 3.1: A photo of an iZIP detector, which is photolithographically patterned with ionization and phonon collection sensors interleaved on the same face.

On each face of the iZIP detector, there are two ionization signal collection channels and four phonon channels in total as illustrated in Fig. 3.2. The inner charge channel is in the center region and covers about 70%-75% surface area of the face. Three of the four phonon channels are in the middle with a surface coverage close to the inner charge channel. The outer charge and phonon channels are interleaved in a ring shape surrounding the inner channel region. The combination of inner and outer channel signals can provide more accurate radial information of an interaction. Combining the radial and depth information together, the 3D position of an interaction can be reconstructed.

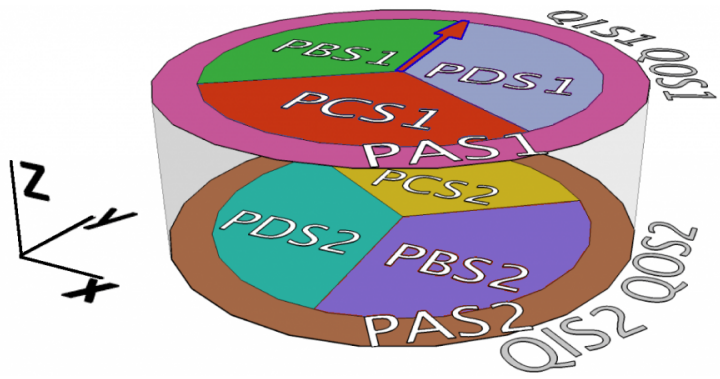

Figure 3.2: There are four phonon signal readout channels and two ionization signal readout channels in total on each face. Three phonon channels are inside and one is outside as a ring. The inner ionization channel is about the same coverage as the three inner phonon channels and the outer ionization channel interleaves with the outer phonon channel.

Another useful quantity that can be constructed is the ionization yield of an event in the iZIP detector, which is defined as its ionization energy deposition over its phonon energy deposition.

$$\text{yield} = \frac{\text{ionization energy}}{\text{phonon energy}}$$

The yield value of a nuclear recoil (NR) event is approximately one third of that of an electron recoil (ER) event [44]. WIMPs produce NRs in the detector while background particles such as gammas, betas, electrons can only produce ERs. Thus, yield can be used to discriminate between an ER and a NR, which provides a possibility to distinguish WIMP signals from many types of backgrounds.

3.1.1. Ionization Signal Collection

The charge electrodes on both the top and bottom detector faces can be voltage biased while all the phonon sensors are grounded. In the high mass WIMP search analysis, all the iZIP detectors were biased in a +2V/-2V mode, which was +2V to one face and -2V to the opposite face. No voltage bias was applied to the sidewall. Due to the non-zero voltage bias on both faces, there is an electric field existing in the detector volume pointing from one face to the other.

When an interaction occurs in the detector, the ionization energy deposited in the crystal creates electron/hole pairs (e^-/h^+ pairs) [45]. If this event is in the bulk region, the electrons would drift to the +2V side and the holes would migrate to the -2V side. Since the phonon sensors are all grounded, if this event is near the surface, both the electrons and holes may migrate to the sensors on the same side and result in an imbalanced charge signal collection on both sides (see Fig. 3.3).

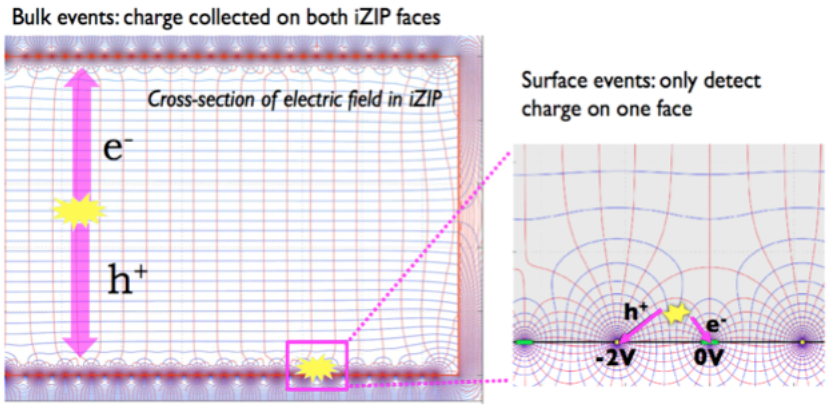

Figure 3.3: When an interaction occurs in the bulk region, electrons and holes migrate to different detector faces after creation due to the external electric field. An interaction that occurs within a few microns of the surface may have both the created electrons and holes drawn to the sensors on the same side.

In practice the electric field is more uniform in the center region than on the edge of the detector. Because of the existence of sidewalls and the intersection points where the sidewalls meet the surfaces, the electric field lines bow. Thus, if an interaction occurs at a large radial position, some of the charge carriers may end up on the sidewall and their information is lost. This group of high-radius events could result in a reduced ionization signal.

If an event interacts with the detector within a few microns on either detector face, it is categorized as a "surface" event. The electric field lines near one face terminate in the grounded phonon sensors on the same face and the electrons and holes of a surface event can

migrate to the sensors on the same face and cause an imbalanced ionization signal collection on both faces. Thus, surface events are a dangerous background type which could lead to a false WIMP discovery. With the interleaved design and the ability to readout charge signals from both sides of the iZIP detector, these surface events can be excluded using the asymmetric feature of ionization signal collection whereby surface events have their charge signals collected on only one detector face and bulk events have their charge signals collected evenly on both faces as illustrated in Fig. 3.4.

During migration, the electrons can be captured and trapped along the way. These trapped electrons then create an internal electric field that opposes the external electric field from the voltage bias. As time goes on, the signal collection degrades (see Fig. 3.5). In order to bring detectors back to a neutralized state, LEDs are used. They are installed on the detector interface boards, or DIBs(see Fig. 3.6), which are placed close to the detector surfaces. These LEDs shine light towards the detector crystals and knock out those trapped electrons. Once the detectors are neutralized, the stability of signal collection is restored.

In the path of migration to the surface, electrons collide with other particles. Thus, their path is not a vertical line from the interaction point to the +2V surface but spreads out with an angle like a cone. These electrons are referred to as oblique electrons. On the other hand, a hole is created due the absence of an electron. Thus, holes are imaginary particles. Their transportation is not affected by collisions with other particles and they will travel to the -2V side in almost vertical lines. In this sense, the radial information of an interaction location is more concentrated when it is provided by the holes.

Since there are two ionization channels on the same side, charge signal crosstalk could exist between channels. The ionization signal in the outer channel can be affected by the ionization signal in the inner channel. This could affect the ionization energy information as well as the radial position information of an interaction.

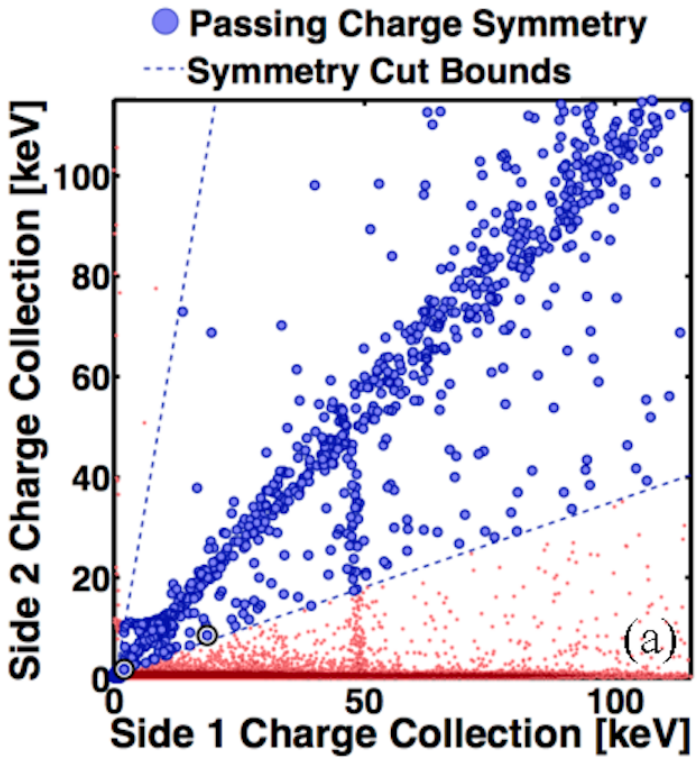

Figure 3.4: This plot shows the charge signal asymmetry of surface events and how the iZIP detector discriminate between bulk and surface events. The x-axis is the summed charge energy on side 1 and the y-axis is the summed charge energy on side 2. If an event occurs in the bulk region, it would deposit an equal amount of charge energy on both sides, which makes it distribute along the diagonal (blue dots). If an event occurs near the detector surface, it would have asymmetric charge energy deposited on both sides, which makes it distribute along either the x-axis or the y-axis (red dots). The two dashed blue lines are the boundaries for charge symmetry selection. There is a ^{210}Pb source plate placed above side 1 of this detector, which produces a large amount of surface event on side 1. The 46 keV line comes from the gammas in the ^{210}Pb decay chain. The two blue dots with bigger black circles are two low yield events that pass the charge symmetry selection, which could be used to derive an upper limit on the surface event rejection power of the iZIP detector [46].

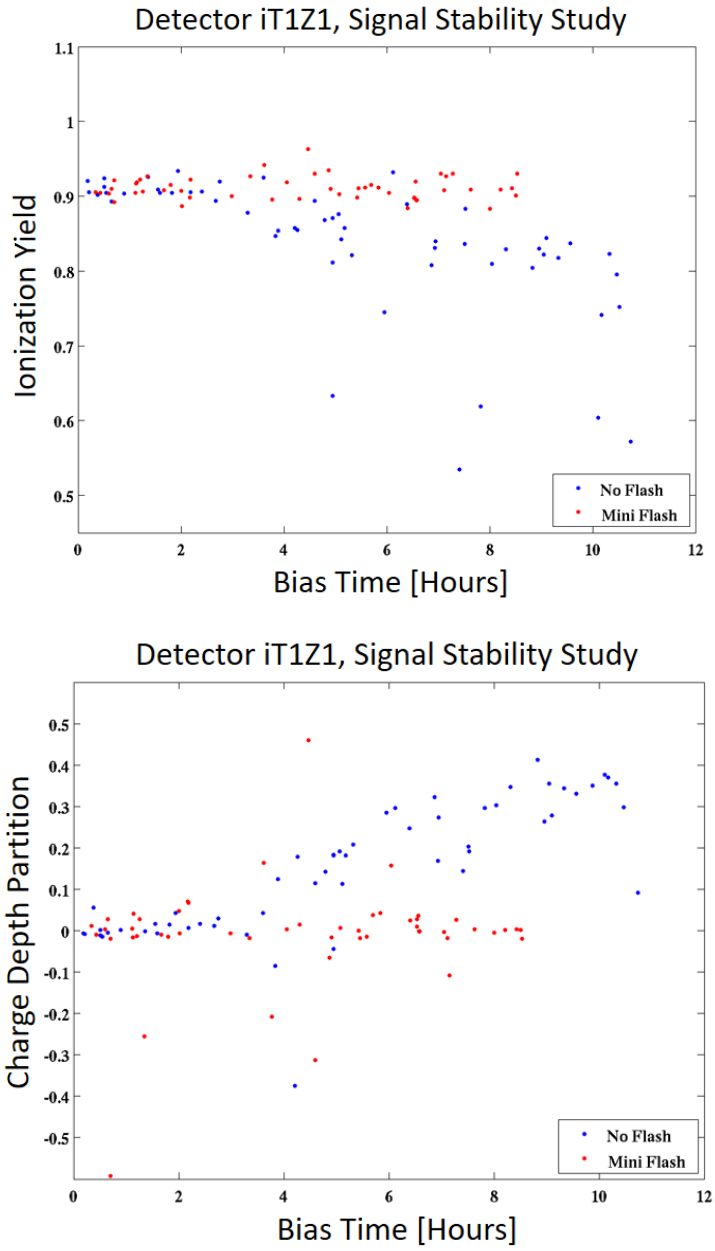

Figure 3.5: These two plots demonstrate the stability of signal collection as a function of time with and without flashing. If the duration of LED light shining is short, e.g. 30 seconds or 1 minute, it is called a mini-flash. The blue dots are from a 12 hour data run with no LED flash performed, while the red dots are from a 9 hour data run with a LED flash once every hour. The data without a LED flash starts to show degradation after three hours. As a comparison, the data with LED mini flashes shows signal stability throughout the whole data collection time. This demonstrates that the LED flash method restores the detectors to their neutral state. The x-axis is the voltage bias time. The y-axis of the top plot is an ionization yield quantity [ygsumINT]. The y-axis of the bottom plot is quantity that describes depth measuring quantity [qzpartOF] based on charge signals from both faces.

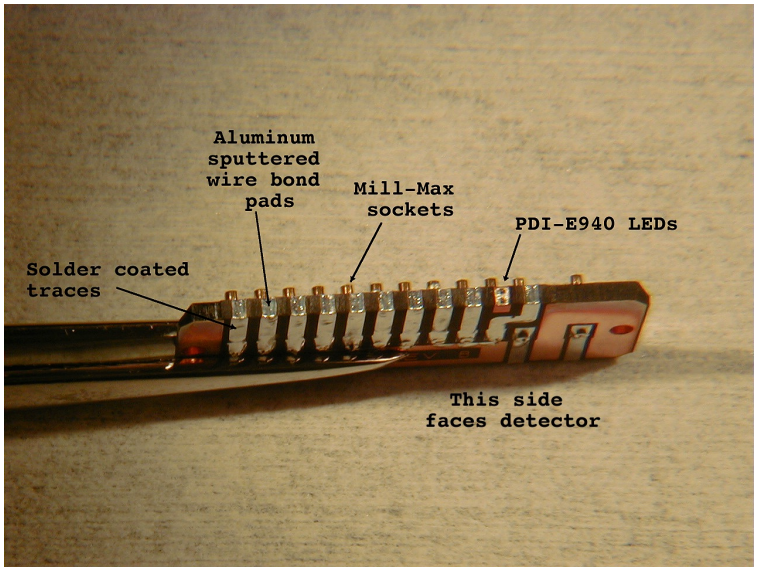

Figure 3.6: Detector interface boards (DIBs) are attached at the sides of a detector and in charge of transferring ionization and phonon signals collected from the sensors out. LEDs are installed on each DIB in order to flash light into the crystal to bring it back to neutral state.

In SuperCDMS, three iZIP detectors are stacked together to form a tower. Although there is a gap between two iZIP detectors in a tower, the ionization channels of the middle detector can also experience crosstalk with the detectors above and below it. Due to the capacitance between two adjacent detectors, a positive charge signal on one detector's face may induce a negative charge signal on the other detector's face. This kind of crosstalk can affect ionization signals from one detector to the other. An estimation of this effect shows that a crosstalk signal of approximately 0.5% is expected between two facing sides [47]. This means that a 2 MeV charge signal on one detector surface could induce a 10 keV negative charge signal on the facing side of its adjacent detector. If an event of 15 keV charge energy occurs in this adjacent detector within a time window of this 2 MeV event, its charge energy estimation would get reduced from 15 keV to 5 keV. As a result, the yield of this 15 keV event becomes one third of its true value. If this is an electron recoil event, it would be misclassified as a nuclear recoil event. Thus, this charge crosstalk can affect the ionization yield estimation of an event and results in an possibility of having this event appear in the WIMP search signal region.

3.1.2. Phonon Signal Collection

When an incident particle interacts with the crystal, it produces either an electron recoil or a nuclear recoil event. When this recoil travels through the crystal, it experiences stopping powers from the surrounding lattice [44]. It gradually releases energy as it passes its way and causes the crystal lattice to vibrate. This vibrational energy will be transmitted via a kind of quasi-particle called a phonon. There are three categories of phonons produced in the SuperCDMS crystal detectors: primary phonons, Neganov-Luke phonons, and recombination phonons.

Primary phonons [48] are produced at the interaction location by the recoiling particle and their emissions are isotropic. They are very energetic, so they interact a lot within a small volume and bounce around due to their small mean free path. They are prevented from propagating to a large distance before downconverting to acoustic phonons via anharmonic decay. Because the acoustic phonons have a mean-free path that is larger than the thickness of the iZIP detector, they could propagate nearly ballistically to the phonon sensors on the detector faces.

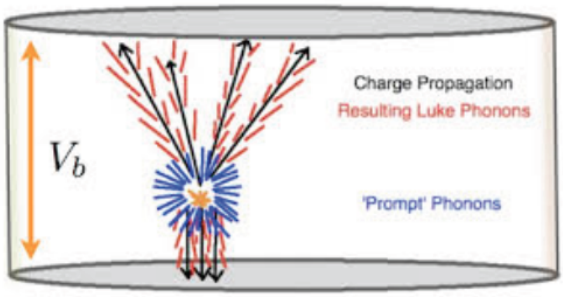

Figure 3.7: Primary (prompt) phonons are created at the interaction location and scatter isotropically. In this plot, the oblique electrons migrate to the top face and the holes migrate to the bottom face. Neganov-Luke phonons are generated along the charge drift direction in a cone shape.

Neganov-Luke phonons [49] are produced during the drift of charge carriers in the crystal (see Fig. 3.7). These charge carriers are quickly accelerated to a constant velocity and the work done on them due to the external electric field is balanced by emitting Neganov-Luke phonons. The relation between total phonon energy (E_{phonon}) and the energy of the recoiling particle (E_{recoil}) can be described by the following equation

$$\begin{aligned} E_{phonon} &= E_{recoil} + E_{Neganov-Luke} \\ &= E_{recoil} + n_{eh}\, V_{bias} \\ &= E_{recoil}\,[1 \;+\; (\frac{Y(E_{recoil})}{\epsilon_{eh}})\, V_{bias}] \end{aligned} \tag{3.1}$$

where n_{eh} is the number of electron/hole pairs created, ϵ_{eh} is the average energy needed to create an electron/hole pair in a particular crystal, V_{bias} is the voltage bias on the detector faces, and $Y(E_{recoil})$ is the ionization yield of the recoiling particle. In order to keep the momentum conserved, ϵ_{eh} of a particular crystal is larger than the band gap energy of it.

In the case of a Ge crystal, ϵ_{eh} is $\sim$3 eV. With a +2V/-2V voltage bias mode, the calculation of total phonon energy becomes

$$E_{phonon} = E_{recoil}\,[1 \;+\; \frac{4}{3}\, Y(E_{recoil})] \tag{3.2}$$

where $Y(E_{recoil})$ is energy dependent and different for electron recoils and nuclear recoils according to Lindhard theory [44], which is used to predict the fraction of energy that goes into the ionization system when given an input of recoil energy. The model proposed by Lindhard is as follows

$$\epsilon = \frac{k \times g(\epsilon)}{1 \;+\; k \times g(\epsilon)} \tag{3.3}$$

where $\epsilon = 11.5 E_r Z^{-7/3}$, $k = 0.133 Z^{2/3} A^{-1/2}$, $g(\epsilon) = 3\epsilon^{0.15} + 0.7\epsilon^{0.6} + \epsilon$. The best k-value for Ge is $k = 0.159$.

The third category is recombination phonons [50]. When electrons and holes reach the electrodes at the detector surface, they recombine, release the band gap energy, and generate recombination phonons. These recombination phonons are emitted like an approximate point source at the surface. They contribute a small amount of energy in the total phonon energy, so the primary and Neganov-Luke phonons are the two that the SuperCDMS considers most.

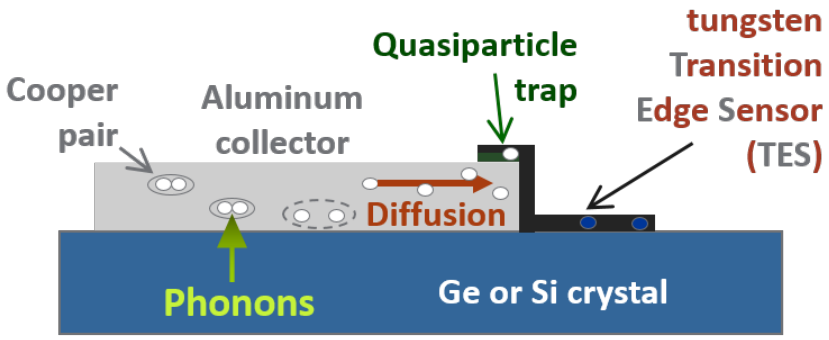

Figure 3.8: This is an illustration on how the phonon information gets collected. When phonons reach an aluminum collector, they get absorbed and then break Cooper pairs in it. These quasiparticles then diffuse till reaching the tungsten quasiparticle trap where they get trapped and their energy get transported to a TES. The TES then transfers this energy to a SQUID to read out.

The iZIP detectors use QETs (Quasiparticle assisted, Electrothermal feedback, Transition edge sensors) to collect and record phonon signal information [50]. As shown in Fig. 3.8, when phonons reach a superconducting aluminum collector, they get absorbed and break Cooper pairs in it. These quasiparticles then diffuse till they reach the tungsten quasiparticle trap, which has a smaller band gap. Once the quasiparticles get trapped, their energy is transported to a TES (Transition Edge Sensor) and heat it up. The TES works at a critical temperature and it is very sensitive to the temperature change. With a change in the temperature by the heat, its resistance changes significantly and causes a change in the current. This current change produces a pulse in the SQUID (Superconducting Quantum Interference Device) and the integral of this pulse is in proportion to the absorbed phonon energy. After this point, the phonon signal is transmitted out to the electronic system.

3.2. Shielding Layers

Although the WIMP signal events are expected and looked for, a variety of background events hit the detectors as well. The environment in which the experiment apparatus resides is a large source of background events. The SuperCDMS Soudan experiment was located in an obsolete mine deep underground. The cavern rock in the mine, the shotcrete painted on the cavern, the material placed on the floor, the equipment outside the experiment room (see Fig. 3.9), were all potential background sources. If they contained a radioactive isotope, a neutron, a gamma, or a beta particle might be emitted from them during a radioactive decay. Any decay product could have a chance to hit a detector and produce a signal. These background events from the surrounding environment might mimic the WIMP signature in a detector, resulting in a false WIMP claim.

Figure 3.9: This is a view of the second floor in the cavern of the Soudan mine where the SuperCDMS experiment was located. The surrounding material could become a source of backgrounds.

In order to protect the detectors from the contamination resulting from the surrounding environment, shielding layers were used near the detectors (see Fig. 3.10). In SuperCDMS, there are two types of background events of most concern: neutrons and gammas.

Figure 3.10: This photo is to show the assembly of shielding layers near the cryogenic region at Soudan site.

Neutrons can come from the radioactive decays of uranium, thorium and their daughter isotopes that exist in the materials nearby, such as the cavern rock, the walls. They can also be generated by the interactions between the high energy muons in the cosmic rays and the materials which make up the shield. When a neutron interacts with one of the nucleons in a detector via an elastic collision, it can produce a signal that is indistinguishable from a WIMP-nucleon elastic collision. Thus, neutrons are the most dangerous background to SuperCDMS. To reduce or eliminate potential neutron backgrounds coming from the surrounding environment, polyethylene layers were selected and used in SuperCDMS Soudan experiment. Polyethylene ($(C_2H_4)_n$) is a solid plastic material, which contains low-Z elements such as carbon (C; Z=6) and hydrogen (H; Z=1). Since neutrons interact readily with low-Z elements, polyethylene is a great material to absorb and reduce incoming neutrons from the environment.

Gammas are another background type of concern to the SuperCDMS experiment. Since most radioactive decays emit gammas, gammas almost exist everywhere. If a gamma particle interacts and deposits energy within a few microns of a detector's surface, the ionization collection sensors may not be able to collect the produced charges fully. This could result in a suppressed ionization signal and hence a reduced ionization yield. If the ionization yield is sufficiently low, the gamma might be tagged as a WIMP. Copper (Cu; Z=29) and lead (Pb; Z=82) were the materials that SuperCDMS used to attenuate and absorb gammas from outside. Gammas are more likely to interact with high-Z elements. Thus, copper layers and lead layers are two excellent choices for shielding from incoming gammas. In addition, the iZIP detector has demonstrated a great rejection power towards the surface events [46].

The SuperCDMS Soudan experiment had five towers of iZIP detectors in total (see Fig. 6.1). Each tower had three iZIPs and was housed in copper. From the inner most region going outward, there were six copper shielding layers called the mixing chamber can, the cold plate can, the still can, the inner vacuum can, the shield can, and the outer vacuum can. Outside the outer vacuum can, there were four more shielding layers. They were called inner polyethylene, ancient lead, lead, and outer polyethylene layers. The outer polyethylene layer attenuated and blocked neutron background particles from the surrounding environment. The lead layer absorbed gammas from outside. The dimensions of each of the shielding layers is listed in Table 3.1.

Since any shielding material itself could also be a source of contamination, an ancient lead layer was placed inside the lead layer. The half-life of ^{210}Pb is $\sim$22.3 years. With an age over 100 years, the ^{210}Pb isotopes in the ancient lead nearly have all decayed away. It contributed less contamination towards the experiment parts inside while still attenuating and absorbing gammas from outside.

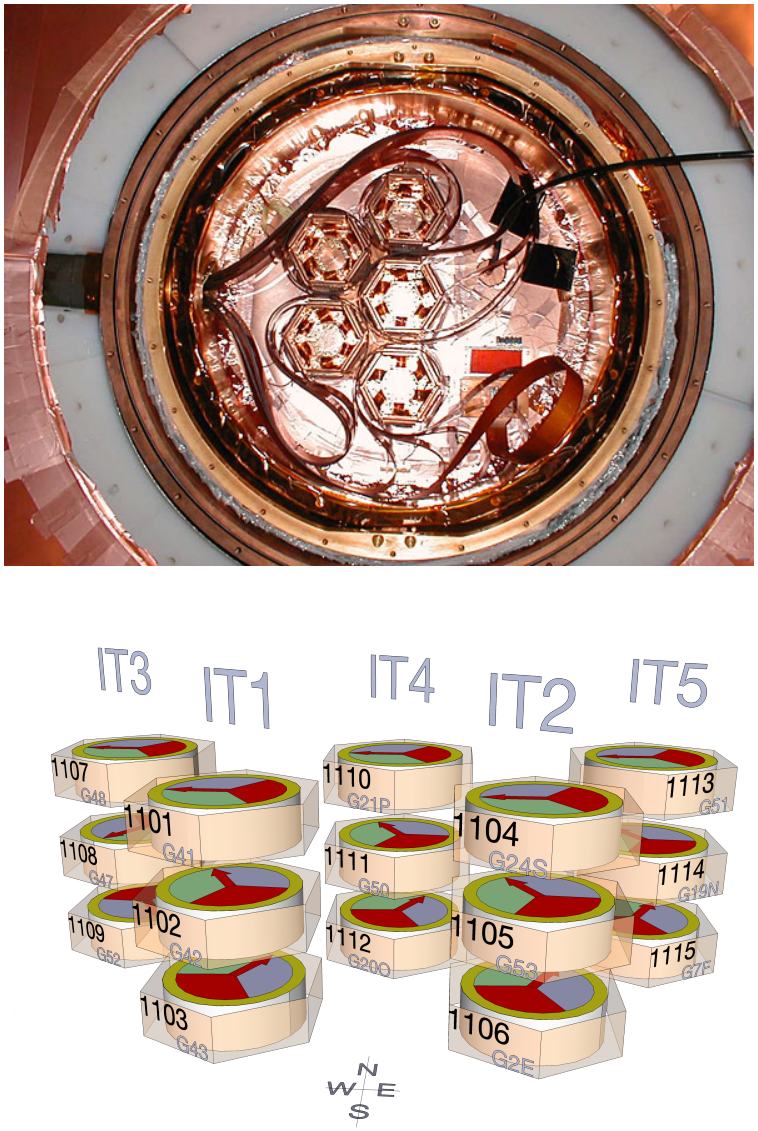

Figure 3.11: The top plot illustrates the layout of the five iZIP towers in the cryogenic region. The bottom plot illustrates the detector and tower orientations.

Layer	**Inner Radius mm**	**Outer radius mm**	**Inner Length mm**	**Outer Length mm**
MixingChamber	151.5	154.675	303.3	309.65
ColdPot	177.475	180.65	361.35	367.7
Still	201.68	204.855	400.15	406.5
InnerVacuum	224.225	227.4	545.3	577.3
ShieldVacuum	251.68	254.855	613.05	619.4
OuterVacuum	280.655	283.83	668	700
InnerPoly	299.037	400.637	730.414	908.214
InnerLead	401.637	446.087	910.214	999.114
OuterLead	450.849	628.649	1008.64	1364.24
OuterPoly	636.587	1030.29	1380.11	2192.91

Table 3.1: Dimensions of each shielding layer at SuperCDMS Soudan.

Inside the ancient lead layer, there was another layer of polyethylene. Since there is an alpha decay in the ^{210}Pb decay chain, neutrons could be produced by these alphas via the (α, n) process in the experimental components. In addition to these neutrons, the outer polyethylene layer may not be sufficient enough to absorb environmental neutrons at a 100% efficiency and there are also neutrons produced from the copper cans inside. This extra polyethylene layer between the lead and outermost copper layer provided additional protection against neutron backgrounds.

Outside the outer polyethylene layer, there was a muon veto panel layer. These were individual plastic scintillator panels that enclosed the whole experiment apparatus. These panels were used to tag the muons passing through the experiment region. High energy neutrons can be produced from muon interactions with the surrounding materials. These neutrons may travel through all the shielding layers and interacts with the detectors, which could result in nuclear recoil signals that mimic WIMP signals. The muon veto panels was designed to identify muon-induced neutrons via coincidence tagging. Any nuclear recoil

event that occurs within a certain time period of an incoming muon would be excluded in the analysis.

3.3. Data Acquisition and Processing

When an interaction occurs in an iZIP detector, ionization and phonon signals are produced. In order to reconstruct this event, these signals must be read out and stored for later data analysis. This process relies on the data acquisition system. Once the raw data is collected, it is processed into some meaningful physics quantities that analyzers can use to perform WIMP searches. This process is called data processing.

The data acquisition system was located at the experiment site. It was divided into two parts: cold hardware, and warm hardware. Cold hardware referred to the part of the system that resided inside the cryogenic region (icebox) and worked in a low-temperature environment ($\sim$50 K). The iZIP detectors were also located in this cryogenic region.

Once an interaction occurred in the crystal, ionization signals from e^-/h^+ and phonon signals were collected by the sensors on the top and bottom faces of the iZIP detectors. Two DIBs were attached to the sides of each detector and each DIB was in charge of transferring signals out from six channels. On the sides of each iZIP tower, there were side coax boards installed. They transferred signals gathered by the DIBs to the top of the tower, where the FETs (Field Effect Transistors) and the SQUIDs were installed. The ionization signals were amplified by the FETs and phonon signals were amplified by the SQUIDs before they were transferred out of the cryogenic region to the room-temperature region.

The inside of the icebox and the room-temperature electronic systems were connected by the striplines (see Fig. 3.12). The cold end of a stripline connected to a SQUET and its warm end connected to the electronic box (E-box) through the electronics stem (E-stem).

Once the signals reached the E-box, they had left the cold hardware part and entered the warm hardware part.

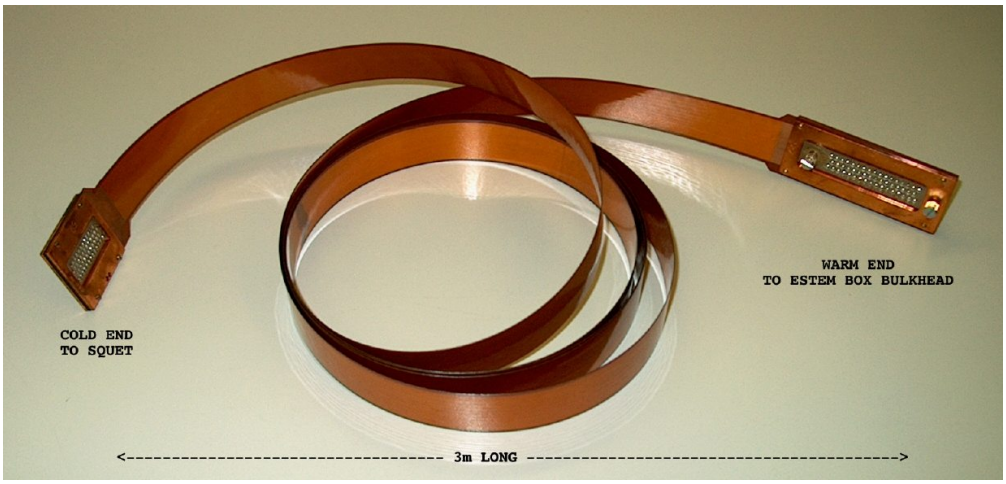

Figure 3.12: The cold end of a stripline connects to a SQUET and the warm end of it connects to the E-box. It transfers the collected signals from the cryogenic region to the room-temperature electronic system.

The warm electronic system decided which events would be recorded by the data acquisition system. Trigger thresholds for the ionization and phonon signals were set by the RTF (Receiver/Trigger/Filter) boards, and usually they were set independently for each detector. If there was a signal higher than the threshold set for a particular channel, a trigger was issued and all the signal information from this event were read out and stored. These events were recorded and stored as raw data on hard drives on computers located in the Soudan Laboratory. Here they were prepared to be transferred from underground to the computers located in a building on the surface. Raw data from the surface computers was then transferred to Fermilab (Fermi National Accelerator Laboratory) for further data processing.

Raw data was processed into quantities known as "RQs" and "RRQs" with a software package known as cdmsbats, which included BatRoot to generate RQs (see Table 3.2) and BatCalib to generate RRQs (see Table 3.3). RQs stands for "Reduced Quantities", which were derived by a quick first-run "reduction" on some of the event information, such as event

time since the start of the run, trigger information, pulse amplitudes. Some of the RQs were further refined to Rational Reduced Quantities (RRQs) to better reflect the physics properties of an event such as energy, timing information.

RQs	**Information Provided**
`SeriesNumber`	The date and time when a particular data series was taken
`EventNumber`	The order number of a particular event in a data series
`LiveTime`	How long the DAQ waits for this particular event
`T[1-5]TGTime[16-25]`	The time of a trigger with respect to the event trigger [20]
`T[1-5]TGMask[16-25]`	Trigger information of a particular trigger
`P[ch]WKr[n]`	Rise time to reach n% of the pulse height
`P[ch]WKf[n]`	Fall time to reach n% of the pulse height
`PTNFchisq`	χ^2 value for phonon energy from non-stationary optimal filter
`QS[1/2]OFchisq`	χ^2 value for side 1/2 charge energy from optimal filter

Table 3.2: List of selected RQs. `T[1-5]` refers to tower 1 through 5. `[16-25]` refers to information of 10 triggers. `[20]` refers to the global trigger. `[16-19]` refers to the four triggers before the global trigger. `[21-25]` refers to the five triggers after the global trigger. `[ch]` = AS1, BS1, CS1, DS1, AS2, BS2, CS2, DS2, or T, S1, S2 (see Fig. 3.2). `[n]` refers to the relative height of a pulse, which can be 10, 20, 40, 50, 70, 80, 100. `S[1/2]` refers to side 1 or side 2.

RRQs	Information Provided
q[i/o][1/2]OF	Inner/Outer charge energy on side 1 or 2
qsum[1/2]OF	Summed charge energy on side 1 or 2
qsummaxOF	Maximum of qsum1OF and qsum2OF
ptNF	Total phonon energy from non-stationary optimal filter
plukeqOF	Luke phonon energy estimated from charge signal
precoiltNF	Non-Luke phonon energy
ytNF	qsummaxOF/precoiltNF
qrpart[1/2]OF	qo[1/2]OF/qsum[1/2]OF
qzpartOF	(qsum1OF-qsum2OF)/(qsum1OF+qsum2OF)
pt[1/2]OF	Summed phonon energy on side 1 or 2
pzpartOF	(pt1OF-pt2OF)/(pt1OF+pt2OF)
pzdelWK	Phonon signal time delay between two sides

Table 3.3: List of selected RRQs. [i/o] refers to inner or outer channel. [1/2] refers to side 1 or side 2.

Chapter 4

Backgrounds

When a type of background event has the ability to fall into the WIMP signal region, it cannot be ignored by the experiment. How to reduce backgrounds and discriminate signals from backgrounds is a life-long topic in the rare event search field. Since WIMP-nucleon interactions rarely occur in a direct dark matter search experiment, it becomes especially crucial to better understand the backgrounds.

For SuperCDMS, backgrounds of concern include neutrons (n), gammas (γ), betas (β^-) and ^{206}Pb nuclear recoils. These backgrounds can come from a variety of contamination sources. Shielding layers were constructed to reduce and block background particles coming from the surrounding environment and cosmic rays. Unfortunately, the materials used to build the shielding layers also had a possibility to become a new source of contamination to the detectors that they enclosed. Although the SuperCDMS experiment used radiopure materials, some radioactive isotopes, such as uranium (^{238}U, ^{235}U) and thorium (^{232}Th), existed naturally and could not be avoid. In addition to the analysis technique, computer simulations were also performed to understand and characterize these backgrounds.

4.1. Gammas

Gamma particles (γ) are one category of background particles relevant to the SuperCDMS experiment. The gamma particles detected in the iZIP detectors are mainly generated and emitted via two physical processes. The first process is radioactive decays that result from uranium, or thorium, or potassium decays. Since the daughter isotope in a radioactive decay is not necessarily in its ground state, an alpha or beta particle usually accompanies gamma particle emission. The second process is the cosmogenic activation of the Ge nucleus. When

a cosmic ray particle interacts with a Ge nucleus, this Ge nucleus could become excited and emit a gamma when it drops back down to its ground state.

The ionization yield, which is defined as the ionization energy deposition of an event divided by the phonon energy deposition, is an important quantity in the discrimination between electron recoils and nuclear recoils. According to the Lindhard theory [44], the ionization yield by an electron recoil is about one third as that by a nuclear recoil event. Thus, for an electron recoil event with charge energy fully collected, it would be easy to discriminate it from a nuclear recoil event.

Unfortunately, since the iZIP detector has a finite volume, there is a geometrical effect on the ionization signal collection. The electric field is strongly distorted near the electrodes. If an event occurs close to it, both the electrons and holes can migrate to the sensors on the same side, which creates imbalanced charge signals on the two sides. In addition, the surface coverage of a sensor is limited, if the energy deposited near the sensor is too high, it can get saturated and some charge energy information is lost. This ionization signal loss can end up in an reduced ionization yield. If this ionization signal loss is large enough, the yield for such an event could be so low that the event is misclassified as a nuclear recoil.

Figure 4.1 show an electron recoil event distribution from ^{133}Ba calibration data in detector iT4Z2. The bulk electron recoils have a yield calibrated to be one. The surface events possess reduced yield values which make their yields have the potential to spread from one down to zero. In this detector, two surface electron recoil events leak into the WIMP signal region and mimic two nuclear recoil events. Without a charge energy symmetry cut (see Fig. 3.4), these two events might cause a false WIMP discovery claim. With the unique design of the iZIP detector, a charge symmetry cut was developed to efficiently reject surface electron recoil events. An upper limit electron recoil leakage level in the 8-115 keV WIMP signal region is at the order of 1.7×10^{-5} at 90% confidence level [46].

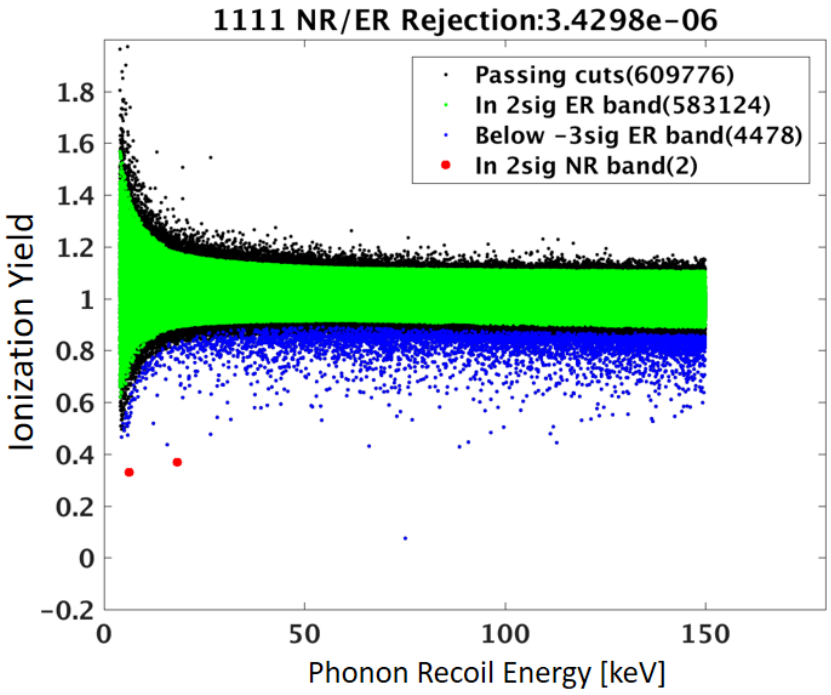

Figure 4.1: This plot illustrates the gamma background distribution from ^{133}Ba calibration data in the phonon recoil energy and ionization yield plane for detector iT4Z2 (1111) . Surface electron recoils (blue dots) have yield values less than 1 and spread out from the bulk electron recoil band (green dots) towards low yield region. Among 609776 electron recoil events passing the data quality cuts, two events (red dots) fall into the 2σ nuclear recoil band WIMP search region.

Another background produced by gamma interactions are the gamma-induced electrons, known as ejectrons. These are the electrons knocked out from a volume by gammas. The ejectrons in the detectors are considered coming from two sources: detector surface or non-detector surface such as housing or the copper cans.

In the first case, a gamma particle hits one detector surface, and an ejectron is knocked out from that surface. This ejectron ends up hitting the surface of a nearby detector. This ejectron event leaves signals in multiple detectors: a gamma signal in one, and an ejectron signal on another. This group of ejectrons is easy to identify using a coincidence check.

In the second case, a gamma particle hits a non-detector surface, such as a copper can, and knocks out an ejectron. When this ejectron interacts a detector there is not a gamma interaction in a neighboring detector that can be used for a coincidence check. Since ejectrons do not penetrate deep into crystals, they leave signals as surface electron recoils in the detectors. This group of ejectrons can leave a single signal with reduced ionization energy and ionization yield, which can increase the chance for this type of event to leak into the WIMP signal region and contribute a fake WIMP signal.

4.2. Alphas, Betas and ^{206}Pb

^{210}Pb is a daughter product of ^{222}Rn, which is ubiquitous. When fabricating detectors or constructing the experiment, ^{222}Rn or its daughters attach to any material surface exposed to air. ^{222}Rn goes through a series of quick decays to ^{210}Pb. ^{210}Pb is of particular interest because it has a half-life of 22.3 years, much longer than the lifespan of the SuperCDMS experiment. ^{210}Pb goes to ^{210}Bi through a beta decay. Then, ^{210}Bi, which has a half-life of 5.3 days, goes to ^{210}Po through a beta decay. Finally, ^{210}Po, which has a half-life of 138 days, goes to ^{206}Pb through an alpha decay. This decay chain ends in ^{206}Pb since it is a stable isotope (see Fig. 4.2).

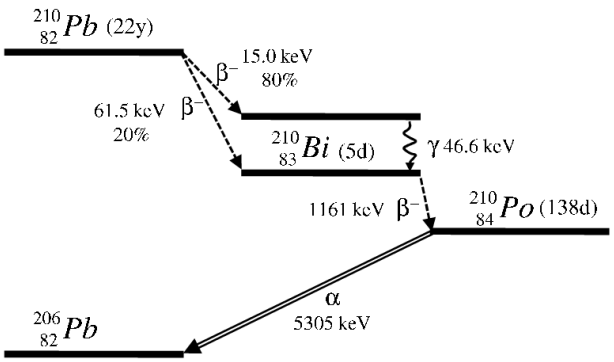

Figure 4.2: ^{210}Pb undergoes two beta decays to reach ^{210}Po, then decays to the stable ^{206}Pb with the emission of a 5.3 MeV alpha particle.

If the beta particles released during this decay process interact in a detector, they leave surface event signals which can have sufficient ionization collection inefficiency to produce a ionization yield that mimics the dark matter signal in the SuperCDMS detectors. The alpha particle emitted during the decay may also generate a neutron particle through the (α, n) process. If this neutron interacts in a detector, it would produce a nuclear recoil signal in that detector that is indistinguishable from a WIMP signal. In addition to these potential backgrounds, the ^{206}Pb recoiling nucleus itself is a nuclear recoil with suppressed ionization yield. All three of these decay products are background sources that need consideration when analyzing SuperCDMS data.

In order to better understand the surface event background, two ^{210}Pb source plates were deployed in tower 3, in which the detectors placed from top to bottom were iT3Z1, iT3Z2 and iT3Z3. One ^{210}Pb source plate was above the top face of iT3Z1 and the other was below the bottom face of iT3Z3. These two source plates provided a substantial amount of surface events so an upper limit of the low yield electron recoil rejection capability can be estimated, which is at the order of 1.7×10^{-5} at 90% confidence level in the 8-115 keV WIMP signal region [46].

4.2.1. Identifying Alpha Particles

During the last process in the ^{210}Pb decay chain, ^{210}Po decays to ^{206}Pb through an alpha decay. The ^{206}Pb recoiling nucleus, which can contribute a nuclear recoil signal in the detector, is emitted back to back with an alpha particle. In order to have an estimation of the ^{206}Pb background rate, a study on the alpha particles was performed.

Assuming the ^{206}Pb emission is isotropic, the number of alpha particles that hit on the detectors should be in equal amount to that of ^{206}Pb. These alphas have a signature kinetic energy of 5.3 MeV, which makes them easy to identify from other background types. In addition, the portion of energy deposited as ionization by alpha particles is not as high as

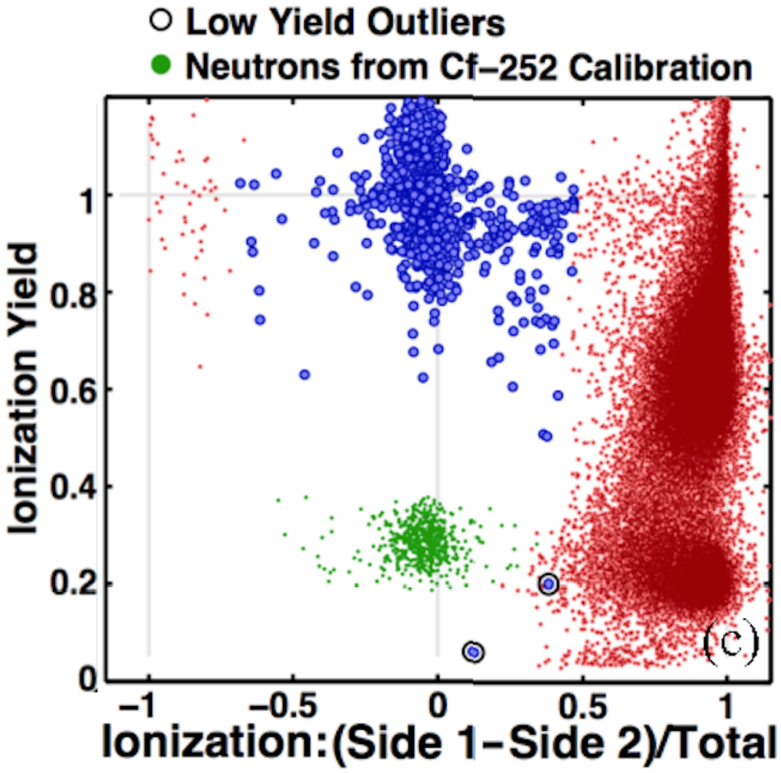

Figure 4.3: This illustrates the surface electron recoil rejection capability of the iZIP detector. This detector is iT3Z1, which has a ^{210}Pb source plate above its side 1. Although the surface events (red dots) can have yield values down to the WIMP signal region, nearly 100% of them get excluded by the charge symmetry selection. Of the electron recoils that pass the charge symmetry selection (blue dots), two of them possess low yield values which are close to the yield of nuclear recoils that pass the the charge symmetry selection (green dots). The study with the two source plates demonstrates that an upper limit of the surface electron recoil rejection power of the iZIP detector is at the order of 10^{-5} [46].

gamma particles. These two features of alpha particles are reflected in a charge energy vs phonon energy plane (see Fig. 4.4). A vertical cut on the phonon energy and a linear cut with a slope that follows the gammas works well on separating the alpha particle candidates out in the lower right region, where the events deposit high phonon energy but low ionization energy.

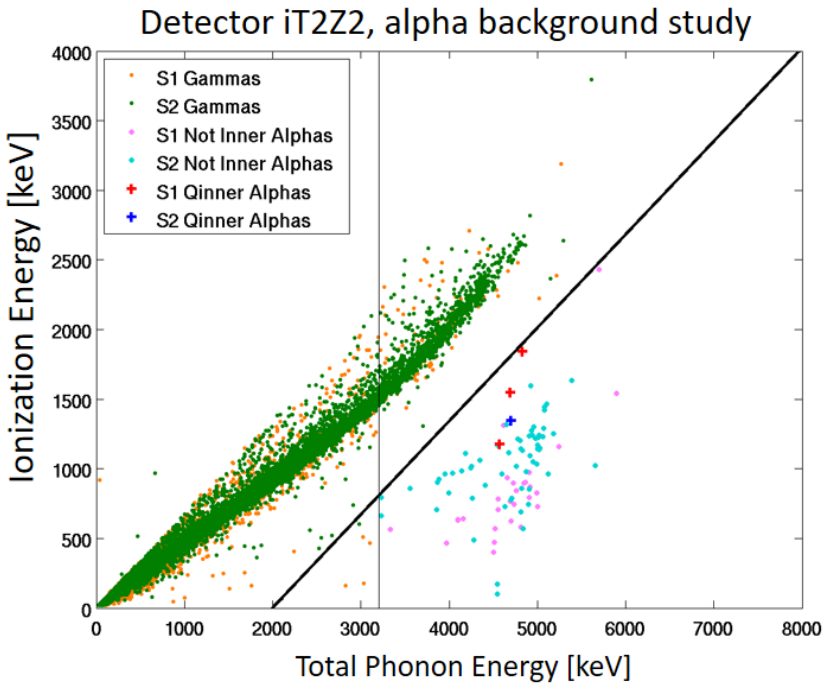

Figure 4.4: The total ionization energy versus the total phonon energy for WIMP search data taken with SuperCDMS. Alpha particles (pluses) have a signature 5.3 MeV kinetic energy. This is much higher than the energies of most gamma particles (orange and green dots) , which makes it easy to identify. Of greatest interest to the analysis are alpha particles in the inner fiducial volume (red and blue pluses). Alpha particles with their energy deposited in the guard channel or with energy shared between the guard and inner channels (pink and cyan stars) are not considered in this analysis.

The alpha particles in the fiducial volume region are those the experiment is interested in. In order to select the alpha particles in the inner charge region, a cut that selected events with high charge energy in the inner channel was developed. The inner charge energy dimension was divided into several energy bins and the distribution of events in each bin

was fit with a Gaussian in the outer charge energy dimension. A mean value and a standard deviation were calculated from each bin. Due to the decrease in statistics as inner charge energy increased, the energy bin sizes were larger in the high energy region (see Fig. 4.5).

Upper and lower 3σ bounds were calculated in each bin. A linear or a second order polynomial fit was performed to define acceptance boundaries. For the alpha particles that occurred in the inner fiducial region, the inner and total alpha background rates were calculated for the best performing detectors and is summarized in Table 4.1. The average inner alpha rate was found to be 0.0022 counts $\cdot$ cm$^{-2}\cdot$ day^{-1} and the total alpha particle rate was found to be 0.028 counts $\cdot$ cm$^{-2}\cdot$ day^{-1}. Comparisons of both inner and total alpha background rates with earlier runs are shown in Fig. 4.6. Although a different type of detector was used in SuperCDMS Soudan, the alpha background rates were found consistent with measurements from CDMS II.

Detector	**Livetime [Days]**	**Inner α**	**Rate [cm$^{-2}\cdot$ day^{-1}]**	**Total α**	**Rate [cm$^{-2}\cdot$ day^{-1}]**
iT1Z1	33.579	4	0.0018	179	0.036
iT2Z1	37.587	9	0.0036	174	0.031
iT2Z2	33.431	4	0.0018	96	0.019
iT2Z3	29.875	5	0.0025	119	0.027
iT4Z1	4.323	0	0	26	0.040
iT4Z3	37.586	5	0.0020	146	0.026
iT5Z2	36.078	3	0.0013	144	0.027
Average	**30.351**	**4.29**	**0.0022**	**68**	**0.028**

Table 4.1: Listed are the inner and total alpha background rates for the seven best performing detectors.

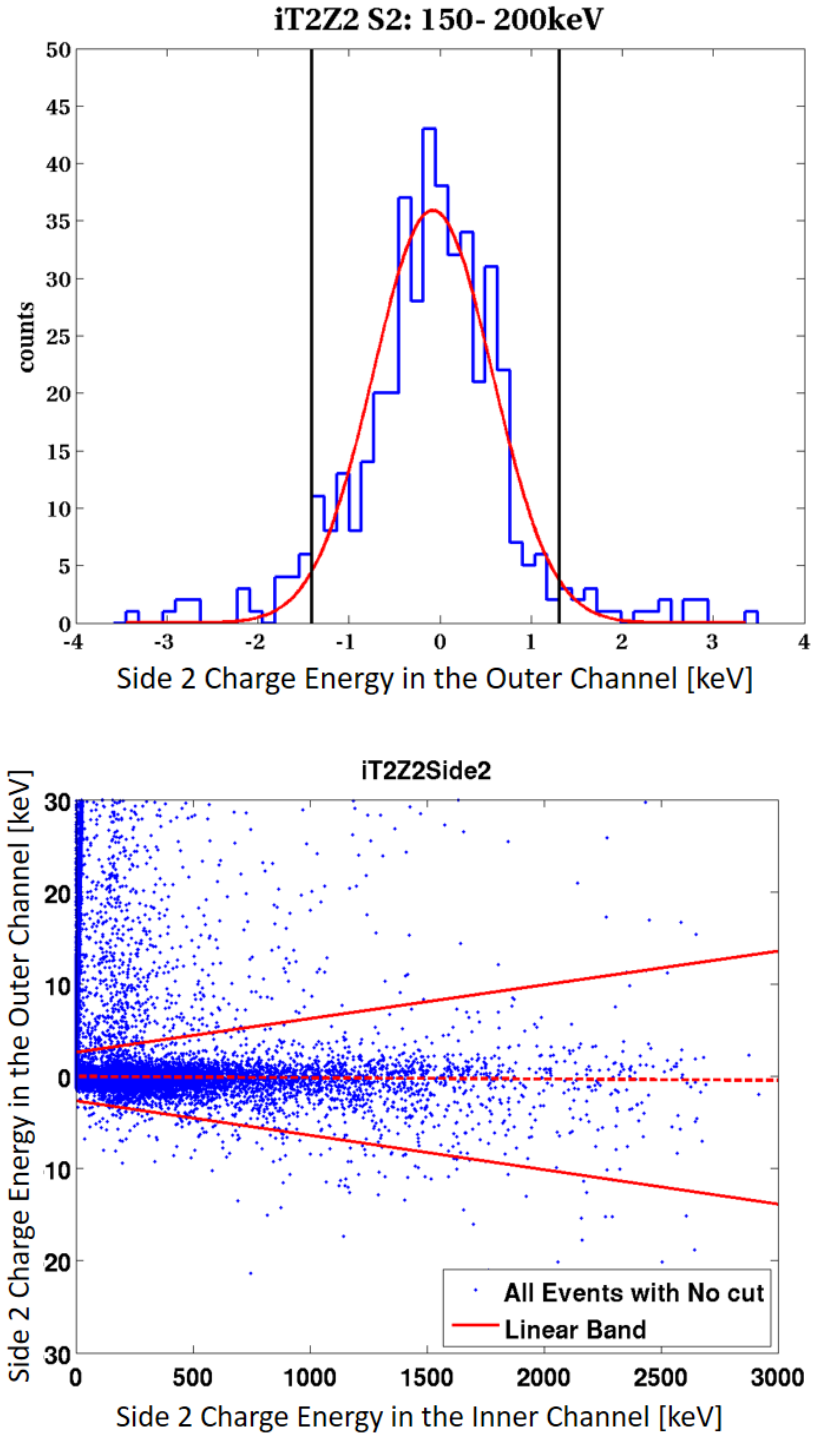

Figure 4.5: The top plot shows a Gaussian fit in the outer charge energy dimension within an inner charge energy bin on the bottom face of detector iT2Z2. From this fit, a mean value and a standard deviation can be calculated. In the bottom plot, linear fits are used for all three data points: mean values, 3σ upper bound, and 3σ lower bound.

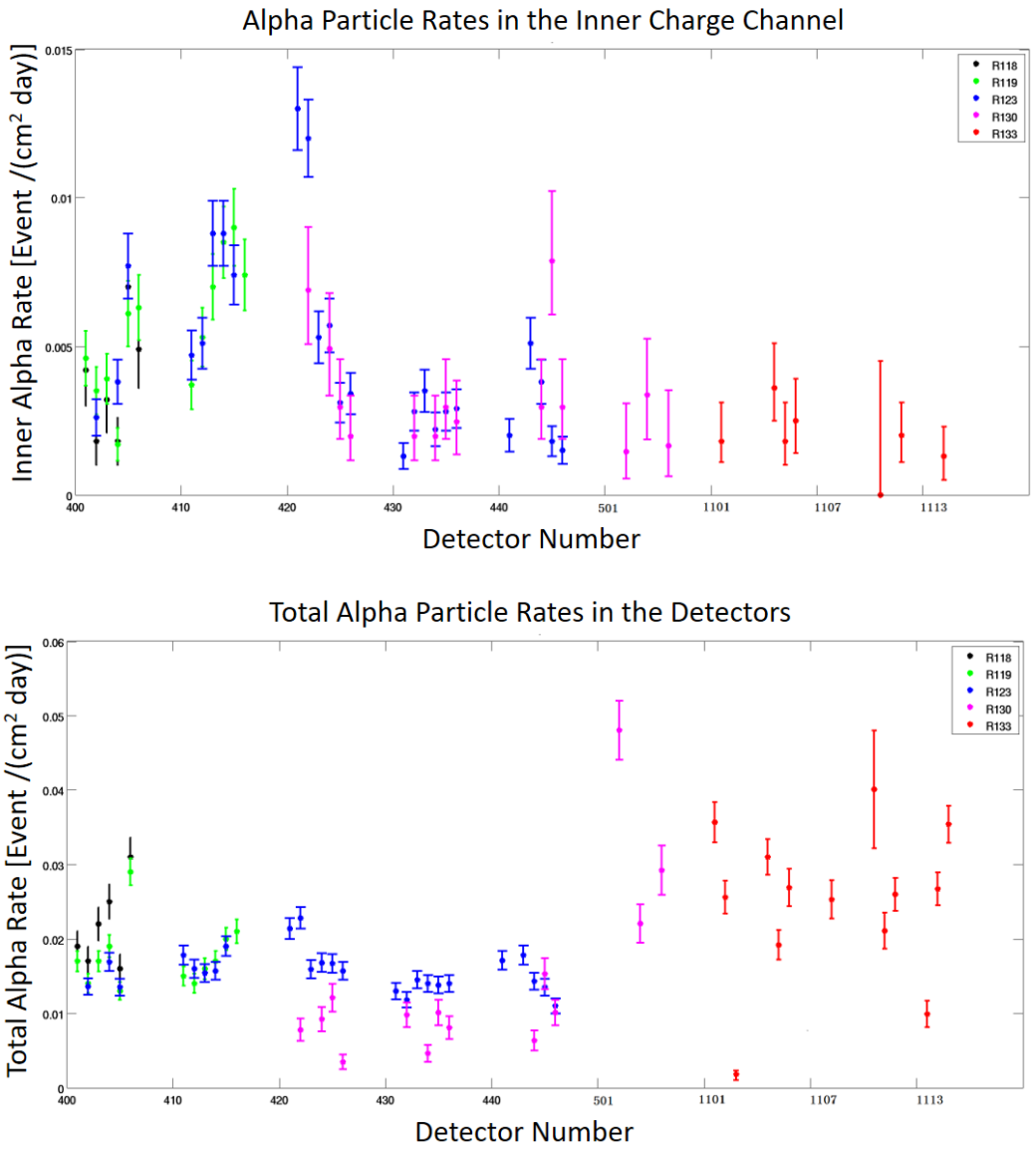

Figure 4.6: The inner alpha background rates (top) and total alpha background rates (bottom) in the iZIP detectors (red dots) compared to the alpha background rate measurements from runs taken with CDMS II (black, green, and magenta dots). Both results show consistent rates with the past measurements. The error bar is in $\pm 1\sigma$.

4.3. Neutrons

When SuperCDMS searches for WIMPs in its data, it looks for the signal of nuclear recoil events produced by WIMPs via elastic collision in the detector. When a neutron interacts with a detector, it also collides with a nucleon elastically and produces a nuclear recoil event. This signal is identical to that which a WIMP produces and could be misclassified in an analysis as a WIMP. This makes neutrons the most dangerous type of backgrounds since they could lead to a false WIMP discovery.

Neutrons can be produced in various ways. In general, the sources of the neutron background can be classified into two categories: radioactive sources, and cosmic rays. An understanding of the neutron background is necessary in order to design specific experimental parts to capture, reduce, and block neutrons. Theory, simulation and calibration are used in SuperCDMS to understand the behaviors of neutron background.

4.3.1. Cosmogenic Neutrons

Cosmic rays are constantly bombarding the Earth. These high energy particles can interact with terrestrial materials and produce secondary products that include muons and neutrons. Muons (μ^-) mostly interact with other particles through four types of interactions: muon-capture, muon-spallation, photo- and lepto- production, and hadro-production. Photo- and lepto- production mainly happens in electromagnetic cascades [51]. Hadro-production mainly happens in hadronic cascades. The first two types of interactions are the main sources for cosmogenic neutrons. When a muon travels through material and is captured by an isotope, this isotope goes to an excited state and then emits one or more neutrons to reach back to its ground state. This process is called muon-capture. If the energy of a muon is high enough, it could hit a nucleus, split it, and cause a nuclear disintegration. Neutrons could be released during this process called muon-spallation.

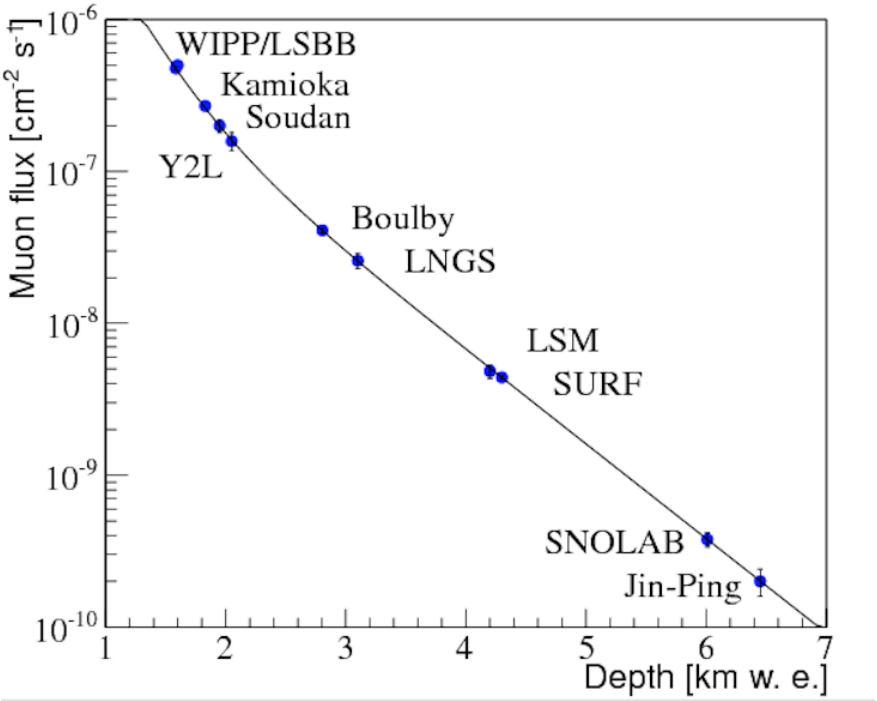

Figure 4.7: To reduce the effect on the experiment from the potential cosmogenic neutrons produced by the muons in the cosmic rays faking a dark matter interaction, the SuperCDMS Soudan experiment was located deep underground. Compared to SuperCDMS Soudan, the future SuperCDMS SNOLAB will experience a smaller muon flux by a factor of 10^3 [25].

$$\text{Muon capture} : \mu + {}^{b}_{a}\mathrm{X} \rightarrow \mathrm{X}^{*} \rightarrow {}^{b-1}_{a}\mathrm{X} + n$$

$$\text{Muon spallation} : \mu + \mathrm{X} \rightarrow n + \mathrm{A} + \cdots$$

When muons interact with cavern rock or experimental components, the muon-induced neutrons can have energies up to GeV scale. These fast high-energy neutrons could easily penetrate through shielding layers and interact in the detectors. In order to avoid muon-induced neutrons, the SuperCDMS Soudan experiment was sited ∼2000 mwe deep underground, and the future SuperCDMS SNOLAB experiment is sited ∼6000 mwe below the surface (see Fig. 4.7).

Although the experiment was located deep underground, SuperCDMS still used a number of plastic scintillation veto panels to monitor muons. The muon interaction signals from these panels allowed coincident tagging to identify muon-induced neutrons. Since these panels were on all faces, if a muon traveled through the experiment setup, it was expected to leave a signal in at least one scintillation panel. If there was a neutron interacted in a detector within a few microseconds of this scintillation signal, this neutron might be induced by this passing muon. Using such a coincidence check, these muon-induced neutrons were removed from the final data analysis.

4.3.2. Radiogenic Neutrons

Radioactive isotopes can generate neutrons through radioactive decays, either by emitting neutrons directly via spontaneous fission, or producing neutrons via the (α, n) process with the surrounding material. Uranium, ^{238}U and ^{235}U, and thorium, ^{232}Th, are the most common elements which could generate radiogenic neutrons. These radioactive isotopes exist in all materials used in the construction of SuperCDMS Soudan. The half-lives of ^{238}U, ^{235}U and ^{232}Th isotopes are of order of 10^9 to 10^{10} years. Even now, they still exist in a certain amount of abundance that cannot be ignored. In addition, many decay products within these decay chains have very long half-lives, which are either longer or comparable to the life span of the SuperCDMS experiment. Thus, the effect of the neutron background contribution from these radioactive decay chains exist through the entire operation of the experiment.

When a radioactive isotope goes through an alpha decay, the emitted alpha particle could interact with the materials nearby to generate a neutron. This (α, n) process can be described as

$$\alpha + \mathrm{X} \rightarrow \mathrm{Y} + n$$

Many elements that exist in common materials include isotopes that could interact with alpha particle and generate a neutron, such as copper ($^{63}_{29}$Cu, $^{65}_{29}$Cu), iron ($^{54}_{26}$Fe, $^{56}_{26}$Fe, $^{57}_{26}$Fe, $^{58}_{26}$Fe), aluminum ($^{27}_{13}$Al), etc. When these materials are used to build experiment parts that

are close to the sensitive detector region, it potentially increases the danger of a neutron background in the experiment. This is why radiopure materials with less contamination from uranium and thorium are in need near the detector region.

Spontaneous fission of heavy isotopes is another way to generate radiogenic neutrons. An isotope with high atomic number, such as ^{238}U, ^{235}U and ^{232}Th, is unstable given that the maximum nuclear binding energy of elements is around an atomic number of 58. These isotopes spontaneously break down into two or more smaller nuclides with the release of neutrons. Compared to the (α, n) process, the relative ratio of radiogenic neutrons generated via spontaneous fission is small. Thus, when designing the SuperCDMS SNOLAB experiment or analyzing data from SuperCDMS Soudan, an estimation of radiogenic neutron background level is critical.

Radiogenic neutrons from the surrounding environment, such as cavern rock, laboratory walls, equipment and tools nearby, can be reduced by the use of passive shielding. Materials containing low-Z elements, such as polyethylene and water, are efficient at moderating neutrons and are used to shield against these backgrounds. Radiogenic neutrons from the experimental components can become a limiting factor to the sensitivity of the experiment. Thus, radiopure materials are needed in the direct dark matter search field to minimize radiogenic neutrons resulting from decays of uranium and thorium in the construction materials.

Chapter 5

Simulations for SuperCDMS SNOLAB

The next generation of the SuperCDMS experiment will include not only an upgrade of the detector payload, but also a new experimental apparatus including new shielding. This new experiment will be located in SNOLAB, Sudbury, Canada. As the experimental plans evolve, simulation efforts are needed to study the new features such as a proposal to use an active neutron veto shielding layer. Simulations are also needed to estimate the nuclear recoil (NR) and electron recoil (ER) background levels in detectors from a brand new experimental setup. This chapter starts by introducing the SuperCDMS simulation package, SuperSim, and then discusses the NR and ER rates in the originally proposed 25 tower configuration with a mixture of Ge and Si detectors. The chapter closes with studies of an active neutron veto layer and a demonstration of its feasibility for the SuperCDMS SNOLAB experiment.

5.1. Simulation with SuperSim

SuperSim [52] is a simulation package specifically developed for use in the SuperCDMS experiments. It is written in the C++ language and it is based on GEANT4 [53]. The SuperSim package provides analyzers with predefined materials, geometries, source particle generators and physics processes for the investigation of potential backgrounds under a variety of situations.

Although SuperCDMS uses multiple shielding layers to reduce backgrounds, no shielding material itself is absolutely pure from containing radioactive sources and some level of contamination needs to be considered in these shielding layers. When running simulations with SuperSim, the user can select a specific geometry and contaminants for the various experimental components. Both text and ROOT formats are available for the simulation output

files. SuperSim is a very powerful and fast growing simulation package that is continuously updated with new materials, geometries and experiment components.

5.1.1. Geometry

At the time of these studies, the official geometry for the SuperCDMS Soudan experiment included five towers of Ge detectors with three detectors in one tower, copper housing for each tower, shielding layers (from outside to inside they are outer polyethylene, aluminum, lead, inner polyethylene, MuMetal, six copper layers, and a cryogenic stem (C-stem) and an electronics stem (E-stem) to connect the inside of icebox to the outside environment). SuperSim automatically configures the materials used, detector tower pattern and orientation, the shielding layers and their dimensions.

SuperSim is also used by the SuperCDMS SNOLAB experiment to investigate the impact of various geometry designs for the shielding. Using the code, analyzers are able to vary both the number of shielding layers and the dimensions of those layers. Detector tower geometries from various designs are also predefined and assigned aliases. These designs differ from each other in the materials used and dimensions of the detectors, the layout patterns and orientations of the towers, etc. In addition, new materials are continuously introduced in SuperSim to study more variations.

5.1.2. Neutron Emission Spectra from SOURCES4 Calculation

In order to study how the contaminations in different experiment components affect the background rates in the detectors, sources of contaminants need to be added in these components in the simulation. Neutron emission spectra are generated using the SOURCES4 software for both uranium and thorium contamination. Since the half-lives of ^{238}U, ^{235}U, and ^{232}Th are greater than 10^9 years and the half-lives of their daughter isotopes are significantly shorter compared to them, these three decay chains are assumed to be in a secular equilibrium state.

In order to perform a computer simulation on the neutron background, a neutron emission spectrum is needed as an input for the simulation. Neutron emission spectra depend on the process and material in which the neutron is generated. There are several software packages that calculate neutron emission spectrum in different materials from different contamination sources. The SOURCES4 package [54] is the code used by the SuperCDMS collaboration. This package can do calculations from the following neutron sources: a homogeneous mixture, a beam, a two-region interface, and a three-region interface. The homogeneous mixture configuration is used by SuperCDMS when generating neutron emission spectra for simulation studies.

Uranium and thorium are the two neutron background sources considered in simulation. Since the half-lives of ^{238}U, ^{235}U, and ^{232}Th are greater than 10^9 years, their decay chains are assumed to be in a secular equilibrium state. When a material is specified, neutron emission spectra are generated for each contamination source. The following example shows the neutron emission spectra that I generated using SOURCES-4A for uranium and thorium contaminations in the brass screws used in SuperCDMS experiment. The type of brass is C3604, and its composition is shown in Table 5.1.

Elements		CAS No.	Weight(%)
Copper	Cu	7440-50-8	57.0 ~ 61.0%
Lead	Pb	7439-92-1	1.8 ~ 3.7%
Iron	Fe	7439-89-6	0.5% Max
Tin	Sn	7440-31-5	0.5% Max
Zinc	Zn	7440-66-6	34.3 ~ 41.2%

Figure 5.1: Mass fractions of different components in brass of C3604 type [55].

The fractions used are 57.4% for copper, 3.0% for lead, 3.0% for iron, 0.3% for tin, and 39.0% for zinc. The density of C3604 brass is 8.0 g/cm^3. Assuming uranium and thorium chains are in secular equilibrium and contamination level is 1 ppb, the neutron emission

spectra for the brass screws from uranium and thorium contaminations is generated via SOURCES-4A. These spectra are illustrated in Fig. 5.2 and Fig. 5.3.

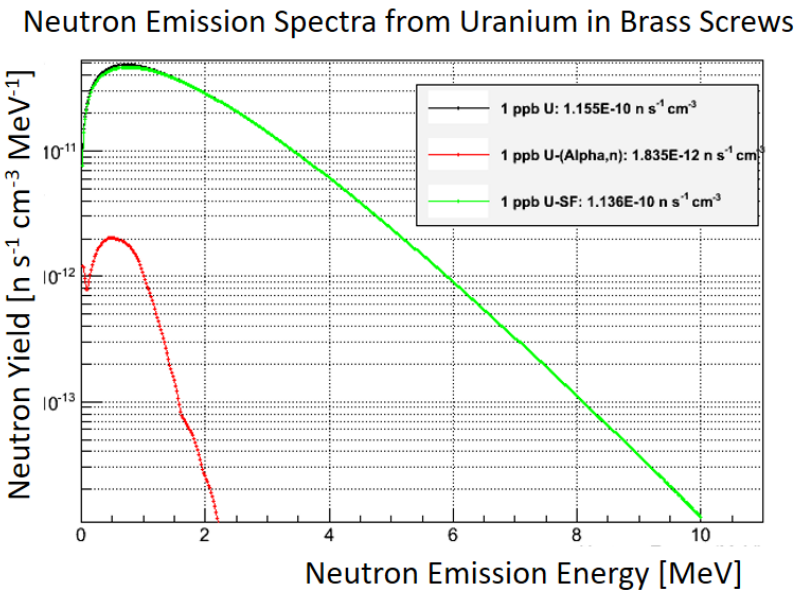

Figure 5.2: Neutron emission spectra from a concentration of 1 ppb uranium concentration in C3604 brass.

For 1 ppb natural uranium contamination in the brass screws, 1.155×10^{-10} neutrons would be produced per second per cubic centimeter. Of which, 1.835×10^{-12} neutrons are contributed from the (α, n) process and 1.136×10^{-10} neutrons are from the spontaneous fission. For 1 ppb thorium contamination in the brass screws, 7.660×10^{-12} neutrons would be produced per second per cubic centimeter. Of which, 7.659×10^{-12} neutrons are contributed from the (α, n) process and 1.313×10^{-15} neutrons are from the spontaneous fission.

Once a contamination level is determined, e.g. x ppb for uranium, the expected neutron yield from brass screws is found by multiplying 1.155×10^{-10} with x. If the operation time and the total volume of brass screws are known, an expected number of neutrons contributed from brass screws can be estimated. Additional neutron spectra which I calculated can be found in Appendix A.

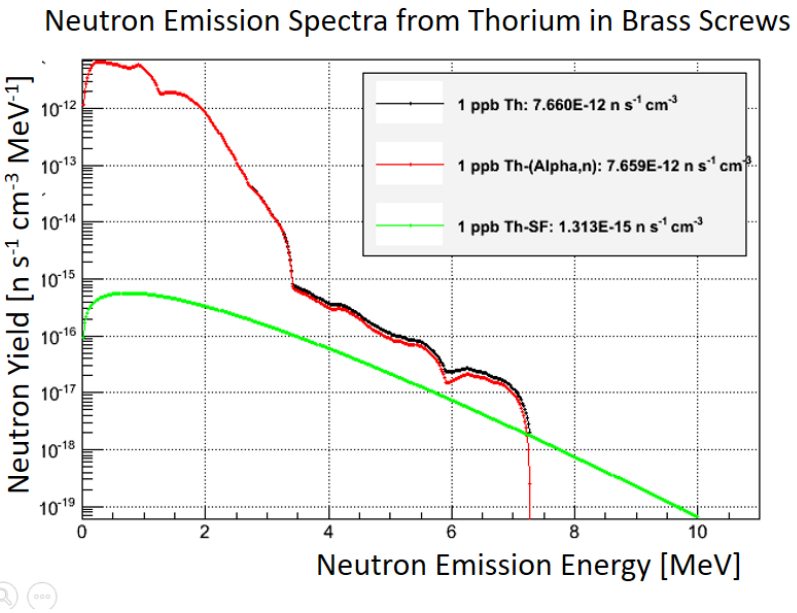

Figure 5.3: Neutron emission spectra from a concentration of 1 ppb thorium concentration in C3604 brass.

5.1.3. Output

After the experiment geometry is set and background sources are contaminated, simulations are run through the SuperSim framework. Simulation output is stored in both text and ROOT formats. By default, track information including the kinetic energy, energy loss, position, timing, momentum and particle type are recorded for volumes such as the detectors which are considered sensitive. These information is illustrated in Fig. 5.4.

Several additional features are available included a flux counter for the various types of backgrounds, for example an ejectron counter. When the flux counter is turned on for a volume, it will record the entry and exit information of all the particles within this volume. By setting this option, it is possible to estimate the fraction of particles that are absorbed by a particular volume. For example, the ejectron counter records the production information of the ejectrons hitting the detectors. By storing this information, it is possible to identify the experimental component where an ejectron is generated. This is particularly useful for identifying single ejectrons versus multiple ejectrons.

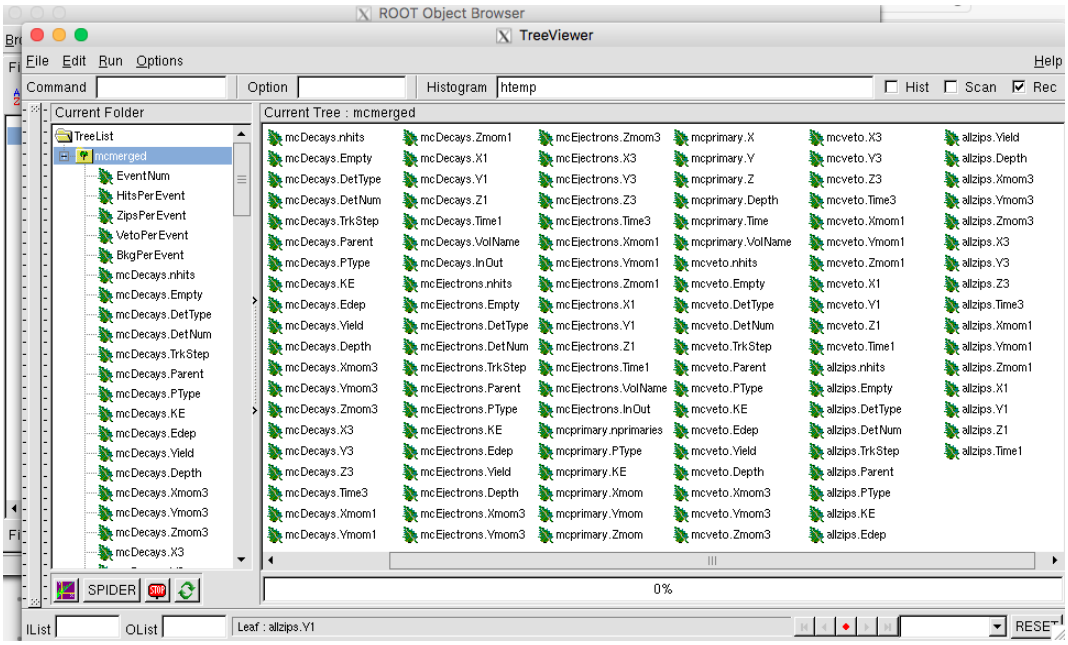

Figure 5.4: A screenshot of the variables stored in one of the SuperSim simulation output files in ROOT format.

5.2. SuperCDMS SNOLAB Background Estimations

The current baseline design for the SuperCDMS SNOLAB experiment consists of four towers with a mixture of both Ge and Si detectors, where two towers will operate in high-voltage mode and the other two towers in normal bias.

The simulations that I performed were of a previously proposed larger payload. The payload was a mixture of both germanium (Ge) and silicon (Si) detectors as illustrated in Fig. 5.6. Simulations estimating the level of neutron and gamma backgrounds were performed with a detector configuration of 25 towers. The outside 15 towers were all Ge iZIP detectors. The center tower consisted of four Ge and two Si detectors operated in high-voltage mode to be sensitive to the lowest mass WIMPs. The nine towers in between were proposed to be of mixed types with two Ge and four Si detectors in each tower. Each Ge detector had a mass of 1.39 kg and each Si detector had a mss of 0.608 kg for a total detector payload of 178.8 kg.

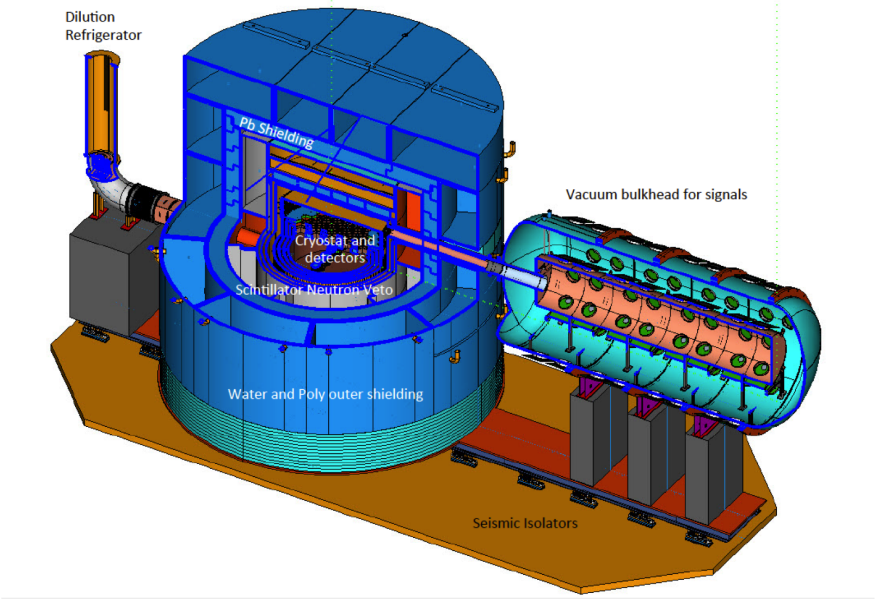

Figure 5.5: This is an illustration of the conceptual experiment design for SuperCDMS SNOLAB.

The towers were to be shielded by multiple layers (see Fig. 5.5) designed and arranged in a way to maximize their ability to block and reduce the backgrounds from outside while minimizing new backgrounds from the construction materials. Several materials had been selected for the shielding layers. The density and mass information of each layer is listed in Table 5.1.

A simulation study was performed to understand and estimate the background level in the detectors with this geometry design. In order to account for all the dominant neutron and gamma sources from the experimental setup, all layers were contaminated with radioactive sources in the simulation. For neutron sources, uranium and thorium decay chains were included. For gamma sources, in addition to uranium and thorium decay chains, ^{40}K isotope was also considered. The radioactivities for these three contaminants in different layers are listed in Table 5.2.

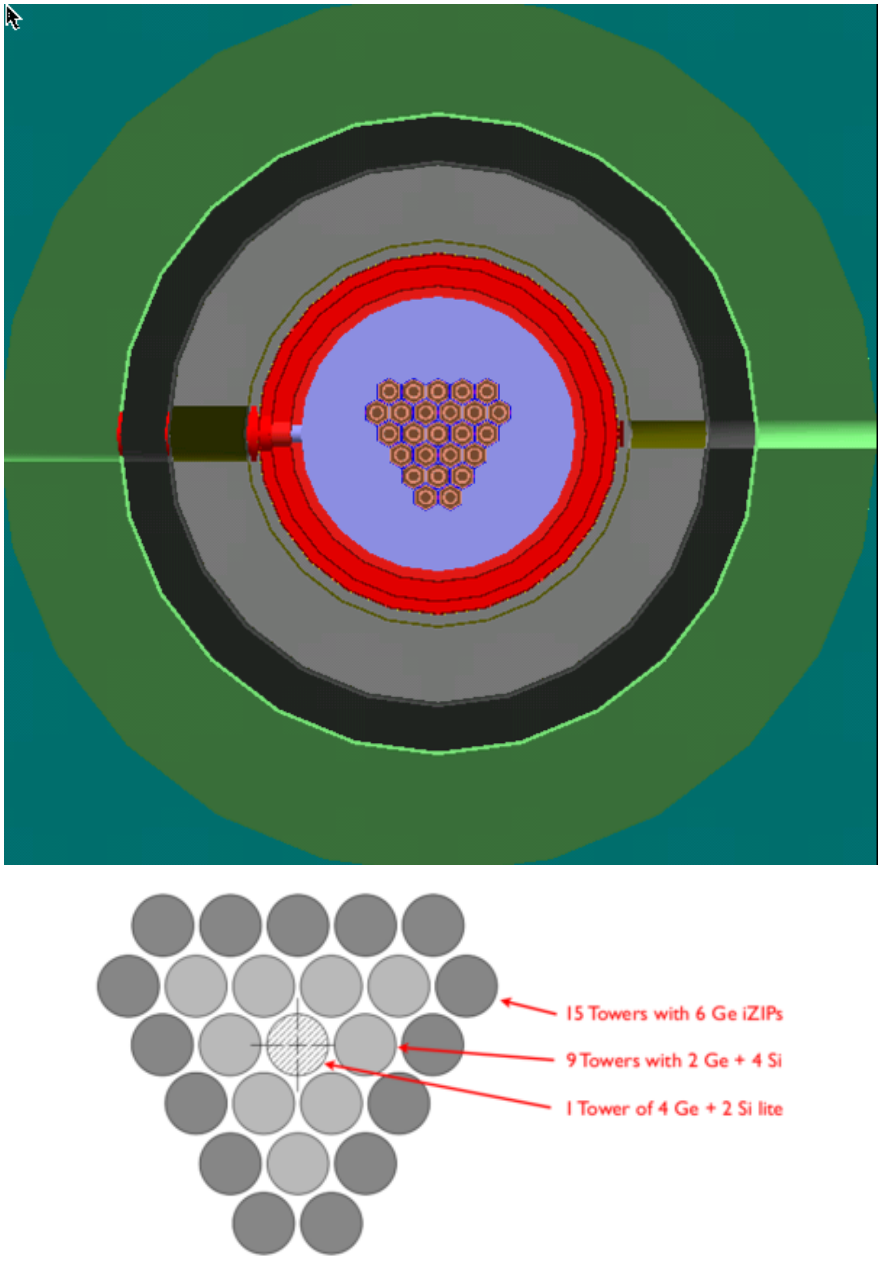

Figure 5.6: The top plot is a cross section view of the experiment geometry in the simulation. The detector towers (brown circles) are in the center surrounded by space for a potential upgrade (purple). Surrounding the detector volume are the copper cans (red), the active neutron veto layer (grey), the lead layer (black), and the polyethylene layer (dark green). The bottom plot provides a more detailed view of the tower arrangement and composition assumed for this geometry.

Layer	Material	Density [g/cm^3]	Mass [kg]
Tower Housing	Cu	8.96	425.36
Mixing Chamber	Cu	8.96	231.14
Cold Pot	Cu	8.96	376.49
Still	Cu	8.96	459.06
Inner Vacuum	Cu	8.96	635.73
Shield Vacuum	Cu	8.96	820.40
Outer Vacuum	Cu	8.96	2316.88
Inner Tank	Acrylic	1.18	242.25
Scintillator	3% B-LAB	0.881	8059.67
Outer Tank	Acrylic	1.18	4992.48
Lead	lead	11.35	108399.5
Polyethylene	Poly	0.94	42091.6

Table 5.1: The material and mass of the shielding layers in Fig. 5.6.

Layer Material	Uranium	Thorium	^{40}K [mBq/kg]
Cu	0.07	0.02	0.04
Acrylic	0.03	0.02	0.1
3% B-LAB	1.2E-4	4.1E-5	2.65E-2
Lead	0.66	0.5	7.0
Polyethylene	0.03	0.02	0.1

Table 5.2: The radioactive level of each contaminant in each material.

In this simulation, one million primary particles were simulated for each contaminant in each layer. The contaminants were assumed to be uniformly distributed in the bulk region of the layers. The single-scatter nuclear recoil and electron recoil events in the detectors (see Fig. 5.7) were selected with the following rules.

- **Nuclear Recoil Event**
  - Energy Range : [E_{min}, E_{max}] keV
  - E_{ER}/E_{NR} : < 0.05
  - Energy Collection Time Window: 10 μs
  - Single Scatter: No energy deposition larger than 2 keV in any other detector
- **Electron Recoil Event**
  - Energy Range : [E_{min}, E_{max}] keV
  - Energy Collection Time Window : 10 μs
  - Single Scatter: No energy deposition larger than 2 keV in any other detector

This study investigated two energy ranges of interest: [2,10] keV and [10,100] keV. After the simulations were complete, nuclear recoil and electron recoil events were counted in each detector as well as their single scatter components. To achieve the estimated rates, conversion factors in unit of exposure [$kg^{-1}\cdot$ $year^{-1}$] are needed and they were calculated in the following ways.

Nuclear Recoil Conversion Factor $F_{conv}[kg^{-1}\cdot\ year^{-1}] =$

$$\frac{nYield[n/s/cm^3/ppb]\cdot A[Bq/kg]\cdot Conv[ppb\rightarrow Bq/kg]\cdot Conv[sec\rightarrow year]\cdot V_{layer}[cm^3]}{N_{prim}\cdot M_{det}[kg]} \tag{5.1}$$

Electron Recoil Conversion Factor $F_{conv}[kg^{-1}\cdot\ year^{-1}] =$

$$\frac{gYield[\gamma/decay]\cdot A[Bq/kg]\cdot Conv[sec\rightarrow year]\cdot M_{layer}[kg]}{N_{prim}\cdot M_{det}[kg]} \tag{5.2}$$

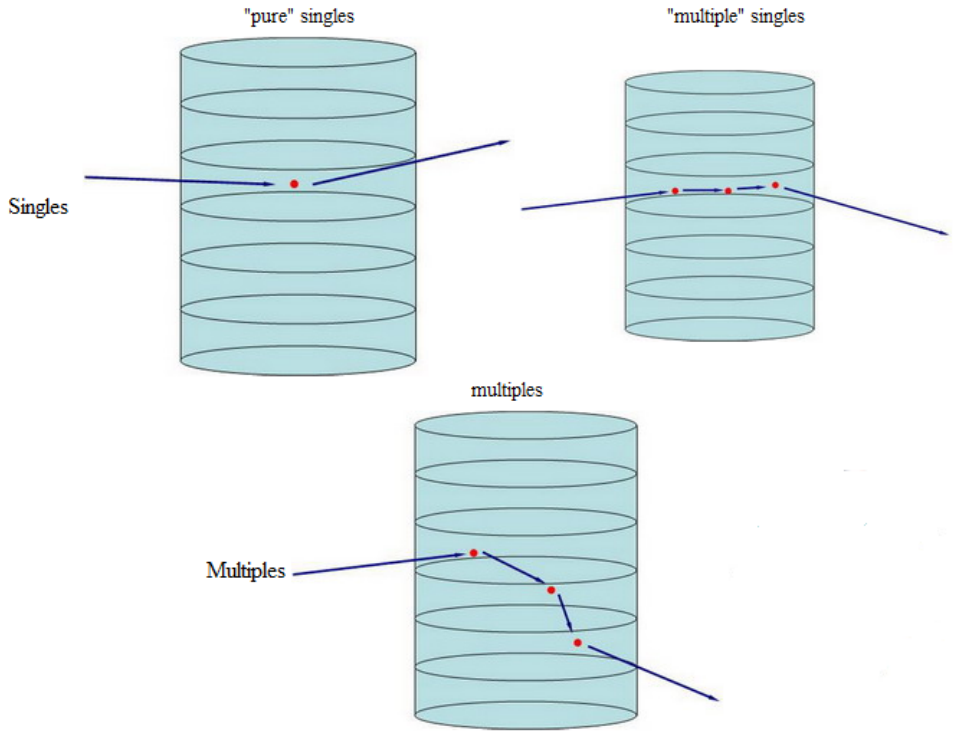

Figure 5.7: In reality, a single scattering neutron should only interact once in a detector. But in data collection, a neutron interacts multiple times within the same detector is not able to be separated from a real single scattering neutron. Thus, these two groups are both parts of single scattering neutrons (Singles) in the data analysis. Neutrons leave signals in more than one detector are referred to as multiple scattering neutrons (Multiples) in the data analysis.

where A is activity of the contaminant, V_{layer} is the volume of a specific layer, N_{prim} is the number of primaries simulated, M_{det} is the total target mass of a detector type, M_{layer} is the mass of a specific layer.

These conversion factors are dependent on the layer material, geometry, contaminant type, contamination level and background particle type. They were used to convert the single-scatter nuclear recoil (NR) and electron recoil (ER) event counts in each layer from each contaminant to event rates. These rates were then co-added together to get the total estimated NR and ER event rates as shown in Table 5.3. Given that the total target mass of Ge detectors was 155.68 kg and that of Si detectors was 23.104 kg, the total estimated rates combined together are shown in Table 5.4.

Detector	**Energy**	**Single NR** [$\mathbf{kg^{-1}\cdot\ year^{-1}}$]	**Single ER** [$\mathbf{kg^{-1}\cdot\ year^{-1}}$]
Ge	2-10 keV	9.49E-04	5.67E+01
	10-100 keV	1.72E-03	1.01E+03
Si	2-10 keV	3.42E-04	2.70E+02
	10-100 keV	1.74E-03	3.66E+03

Table 5.3: Estimated single scatter NR and ER rates in different energy ranges for Ge and Si detectors separately.

Detector	**Energy**	**Single NR**	**Single ER** [$\mathbf{kg^{-1}\cdot\ year^{-1}}$]
Ge + Si	2-10 keV	8.70E-04	8.43E+01
	10-100 keV	1.72E-03	1.35E+03

Table 5.4: Estimated single scatter NR and ER rates in different energy ranges for a combined payload of 178.784 kg.

Assuming the total experiment exposure of this study to be 385 kg-years, the estimated numbers of single scatter nuclear recoil and electron recoil events was found to be as shown in Table 5.5. In the energy range of [10, 100] keV, the estimated number of single-scatter nuclear event was less than 1 for a 385 kg-years exposure. This 25 tower configuration of mixed Ge and Si detectors with this proposed geometry of shielding layers demonstrates the feasibility of a upgraded SuperCDMS SNOLAB experiment.

Detector	**Energy**	**Single NR**	**Single ER [kg^{-1}· year^{-1}]**
Ge + Si	2-10 keV	3.35E-01	3.24E+04
	10-100 keV	6.63E-01	5.21E+05

Table 5.5: Estimated numbers of single-scatter NR and ER events in different energy ranges for an experiment exposure of 385 kg-years.

5.3. Active Neutron Veto Shield

SuperCDMS Soudan used passive shielding layers to attenuate and block background particles and an active muon veto to tag muons crossing the detectors. While this was sufficient to achieve the goals of the SuperCDMS Soudan experiment, an investigation was conducted to ascertain if an active neutron veto would be necessary to achieve the goals of SuperCDMS SNOLAB. This veto would look for interactions that are coincident between the neutron veto and the detectors to minimize the number of single-scatter neutron events observed. In addition, the neutron veto could serve as a neutron monitor to continuously monitor the neutron backgrounds in the experimental cavern.

This proposed SuperCDMS SNOLAB experiment aimed for a sensitivity to the spin-independent WIMP-nucleon interaction cross section down to 8×10^{-47} cm^2 for a WIMP mass of 50 GeV/c^2 by the end of the planned five-year operating period. Considering a target mass of 92 kg of Ge detectors, a five year running period, a 367 kg-years raw ($\sim$ 244 kg-years net) exposure, and the 8-48 keV$_r$ WIMP search range, the expected neutron

background would have been ∼0.04 events for radiogenic neutrons and ∼0.008 events for cosmogenic neutrons.

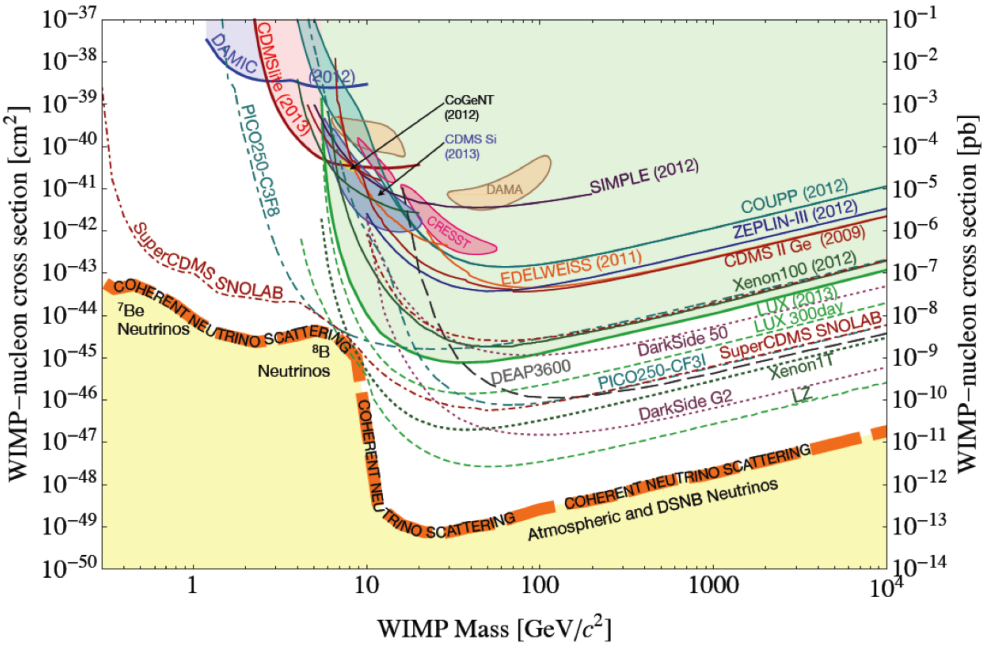

Figure 5.8: This proposed SuperCDMS SNOLAB experiment would have provided sensitivity to a WIMP-nucleon cross section that would have reached down to 8×10^{-47} cm^2 for a WIMP mass of 50 GeV/c^2 by the end of the planned five-year operating period. This Generation-2 (G2) experiment would have had unparalleled sensitivity for low-mass dark matter, with a sensitivity goal that was 100 times better than the current limits at 13 GeV/c^2, increasing to 6×10^5 times better sensitivity at 1.2 GeV/c^2. (Based on original DOE proposal in 2013 [56])

Several potential materials for the construction of an active neutron veto were considered including plastic scintillator and liquid scintillator. Several geometries were studied including different layer thicknesses and layouts. For the liquid scintillator option, the material for the vessel containing the scintillator was also studied.

5.3.1. Plastic Scintillator

In order to enhance the ability of neutron capture in the active neutron veto layer, gadolinium (Gd) with natural abundance was introduced into polyethylene as a doping

Neutron Background Type	Background Rates [event · keV^{-1}· kg^{-1}· year^{-1}]	Expected Background Number
Radiogenic Neutrons	4×10^{-6}	0.04
Cosmogenic Neutrons	8×10^{-7}	0.008

Table 5.6: Estimated neutron event number at SuperCDMS SNOLAB with the assumption of a ∼244 kg-years net exposure and an 8-48 keVr WIMP search range [56].

element in the simulations. The thermal neutron capture cross section of the ^{157}Gd isotope is about 255,000 barns, which is highest among all stable nuclide. Its abundance is around 15.68%. Another isotope ^{155}Gd also has a very high thermal neutron capture cross section, which is about 61,000 barns. Its abundance is around 14.7%. On average, natural gadolinium has a thermal neutron capture cross section of 48,890 barns [57]. When a neutron is captured by a gadolinium isotope, a gamma particle is emitted. The energy spectrum of gamma emission can be up to ∼8 MeV.

$$^{A}Gd + n \rightarrow \gamma + ^{A+1}Gd$$

A study was conducted to estimate any increased background that may be introduced to the experiment by the materials that would be needed to construct a neutron veto around the SuperCDMS SNOLAB experiment. The first step was to examine the electron recoil and nuclear recoil events in the detectors from the existing shielding layers, and determine if their rates change with potential different geometries of the active neutron veto layer. The second step was to study the efficiency of the active neutron veto layer at tagging and identifying neutron-induced nuclear recoil events in the detectors as a function of neutron veto threshold energy.

When this study took place, the maximum detector payload at SuperCDMS SNOLAB was proposed to be 400 kg. Each Ge detector was proposed to have a mass of 1.39 kg and

six of these detectors would be stacked into a tower. The maximum capacity of the cryostat was 48 towers. For this plastic neutron veto study, a configuration of a 225 kg Ge detector payload was proposed, which was equivalent to 27 towers. The towers were arranged in a formation as shown in Fig. 5.9.

The available space for the shielding layers was fixed outside the outermost copper can. With 52.5 inches available in the radial direction and 60.3 inches available for the top and bottom caps. Since the aluminum layer was 1-inch thick and the polyethylene layer was 24-inches thick in both the radial and vertical direction, there remained 13.75 inches of space available in the radial direction and 17.65 inches of space for the top and bottom caps for both the Gd-loaded polyethylene and lead layer with 13.75 inches of space available in the radial direction and 17.65 inches available for the top and bottom caps as illustrated in Table 5.7. The doping percentage of Gd in this study was 0.12% in mass fraction and the density of the Gd-loaded polyethylene was 0.94 g/cm^3.

Layer Material	**Radial Thickness (inch)**	**Top/Bottom Thickness (inch)**
Gd-loaded Poly	13.75	17.65
Lead	13.75	17.65
Aluminum	1	1
Polyethylene	24	24
Total	**52.5**	**60.3**

Table 5.7: The dimensions of each shielding layer.

In order to examine the nuclear recoil and electron recoil event rates in the detectors that originated in the shielding layers, radioactive levels for different contaminants were assumed in each layer as shown in Table 5.8.

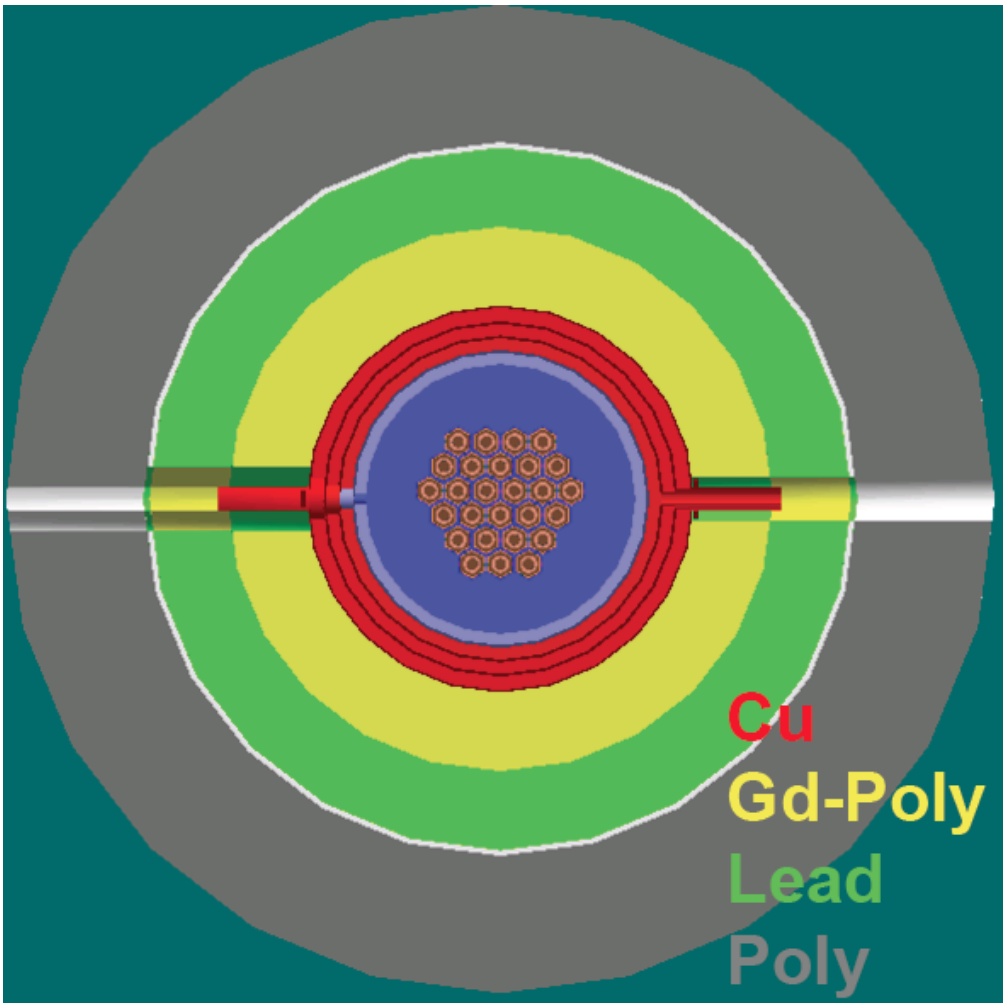

Figure 5.9: Example of one system design considered in this study for a neutron veto in the SuperCDMS SNOLAB experiment. In this study, a configuration with a 225 kg Ge detector payload in 27 towers was investigated. From the inside out, there are 27 detector towers, six copper cans, one Gd-loaded polyethylene layer, one lead layer, one aluminum layer and one polyethylene layer. Silicon photomultipliers were considered as the readout device for the active neutron veto layer. The two pipes connecting to the refrigerator and electronic box are visible on the left and right hand sides of the cryogenic region.

Material	^{238}U (mBq/kg)	^{232}Th (mBq/kg)	^{40}K (mBq/kg)
Copper	0.1	0.02	0.04
Gd-loaded Poly	0.3	0.2	1.0
Lead	2.0	0.5	7.0
Polyethylene	0.3	0.2	1.0

Table 5.8: Radioactivities of each contaminant considered in each material.

Electron recoil (ER) and nuclear recoil (NR) events in the detectors were counted according to the selection rules in Table 5.9. For an event to be classified as a multiple signal event, it was required that there was an energy deposition larger than 2 keV in at least one of the other detectors and an energy deposition between 10 and 100 keV in the primary detector. If there was only an energy deposition between 10 and 100 keV in the primary detector and none of the other detectors had an energy deposition larger than 2 keV, the event was counted as a single-scatter event.

	NR	ER
High Energy Range [keV]	[10, 100]	[10, 100]
Low Energy Range [keV]	[2, 10]	[2, 10]
E_{ER}/E_{NR}	< 0.05	-
Time Window [μs]	10	10

Table 5.9: NR, ER selection rules in detectors.

For each contaminant in each layer, a simulation of five million primary particles was run using SuperSim. Using the radioactivity numbers in Table 5.8 and the selection rules in Table 5.9, the total NR, ER and single-scatter NR, ER rate ranges in the detectors were calculated from the simulation outputs. Results of this calculation are shown in Table 5.10.

	[2, 10] keV	[10, 100] keV	Unit
Total NR	[4.99E-3, 5.18E-3]	[6.69E-03, 6.90E-03]	event kg^{-1}·$year^{-1}$
Single NR	[1.03E-3, 1.11E-3]	[1.76E-03, 1.87E-03]	event kg^{-1}·$year^{-1}$
Total ER	[3.41E+1, 1.18E+3]	[4.87E+02, 1.73E+03]	event kg^{-1}·$year^{-1}$
Single ER	[6.27E+0, 1.14E+3]	[1.78E+02, 1.36E+03]	event kg^{-1}·$year^{-1}$

Table 5.10: NR, ER and single-scatter NR, ER rate ranges in the detectors.

Low energy NR and ER events can also be counted by changing the energy range selection from [10, 100] keV to [2, 10] keV. The energy threshold for classifying multiple and single-scatter events remains as 2 keV in the other detectors. In this case, the total low energy NR, ER and single-scatter low energy NR, ER rate ranges in the detectors can be calculated. The results are shown in Table 5.10.

The purpose of adding an extra active neutron veto layer is to further tag single-scatter neutrons in the detectors via a coincidence check. In order to study the efficiency of tagging neutrons, a study was performed to check the interaction and energy deposition between neutrons and the veto layer material. Energy deposition in scintillators is quenched and this effect is described by Birk's law [58]. The degree of this quenching effect depends on the scintillator material

$$\frac{dE_{vis}}{dx} = S \frac{\frac{dE}{dx}}{1 + k_B \frac{dE}{dx}} \tag{5.3}$$

where S is the scintillation efficiency and k_B is Birk's constant. For Gd-loaded polyethylene, a k_B value of 0.001 g MeV^{-1} cm^{-2} was used. The variable dE is the actual energy deposition within a distance of dx. The variable dE_{vis} is the visible energy after the quenching effect in a particular scintillator.

The requirement of the active neutron veto system design is selected to reject over 90% single-scatter neutron-induced nuclear recoil events in the detectors. The single-scatter neu-

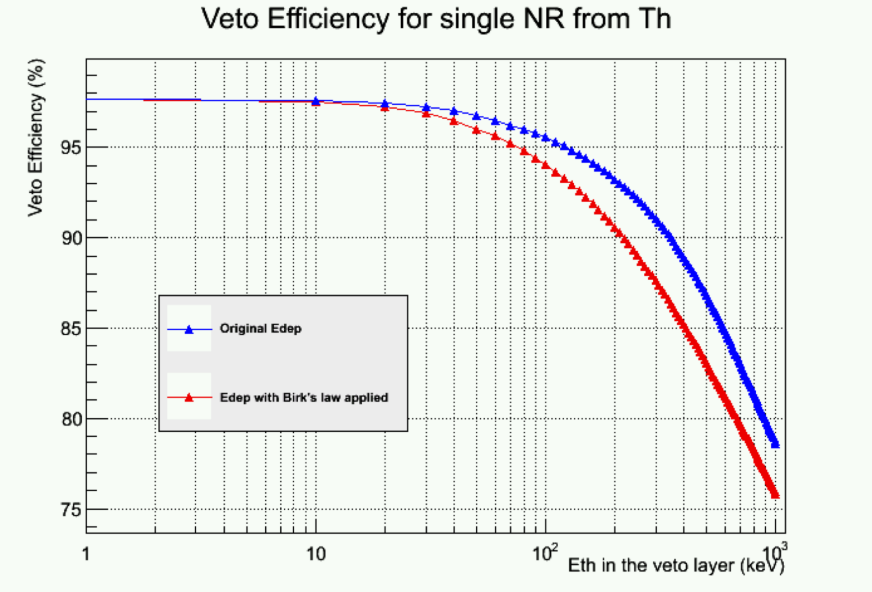

Figure 5.10: The red curve shows the single-scatter neutron capture efficiency as a function of the energy threshold (E_{th}) in the Gd-loaded polyethylene layer with Birk's law taken into account. The blue curve shows the veto efficiency without implementing Birk's law. These are the single-scatter neutrons from ^{232}Th contamination with an energy deposition in the [10, 100] keV range in a detector.

tron veto efficiency drops as the energy threshold increases as expected (see Fig. 5.10). For an energy threshold less than 100 keV, the single-scatter neutron veto efficiency stays above 90% with an assumption of 100% scintillation efficiency in the 0.12% Gd-loaded polyethylene. This result shows the feasibility of such a plastic neutron veto design to be used in the future SuperCDMS SNOLAB experiment.

5.3.2. Liquid Scintillator

A liquid scintillator is another option for the active neutron veto layer that I considered in my studies. The deployment of such a shielding layer could increase the ability to identify, monitor and reject any neutron-induced backgrounds and provide an in situ measurement of the neutron activity for the SuperCDMS SNOLAB experiment. This study considered linear alkylbenzene (LAB) as a target material. Its formula is $C_6H_5C_nH_{2n+1}$, where n could vary from 10 to 16. Thus, LAB is an organic compound family. Since LAB consists of low Z elements, it has a higher potential to capture and absorb neutrons.

In addition, similar to the polyethylene loaded with gadolinium option, doping with elements that have higher neutron capture cross sections was also considered in the liquid scintillator case. Both gadolinium (Gd) and boron (B) were candidate elements considered. One of the B isotopes, ^{10}B, has a high neutron capture cross section of 3,838 barns [59] and its natural abundance is ∼20%.

Using gadolinium as a doping element in LAB has been demonstrated in the Daya Bay experiment [60]. The gamma spectrum emitted when neutrons are captured by gadolinium extends up to 8 MeV. This end point is high enough for any energy threshold that could be set for the liquid neutron veto module. However, there are some challenges in using gadolinium. The liquid scintillator module has a limited volume, so it may be hard to fully contain high energy gammas.

Boron-doped LAB had not been demonstrated at a large scale by any experiment at the time of this study. As a new option, it was carefully studied. Boron is purer than gadolinium. Once a neutron is captured by a boron isotope, its capture products, ^{7}Li and α, could be fully contained in the liquid scintillator volume. Due to the quenching effect described by the Birk's law, the light output in the module may be as low as around 50 keVee. To collect such a low energy deposition within the module sufficiently is one of the challenges if a selected 90% single-scatter neutron veto efficiency needs to be maintained.

Unlike the plastic scintillator case, a tank would be needed to hold the liquid scintillator. This new component could become an additional contamination source. It may also block the neutrons emanating from the detectors and affect the neutron veto efficiency in the liquid scintillator module.

In order to investigate the tank material candidates, a geometry of a proposed experiment setup was used as shown in Fig. 5.11. From the inside out, there were 27 Ge detector towers

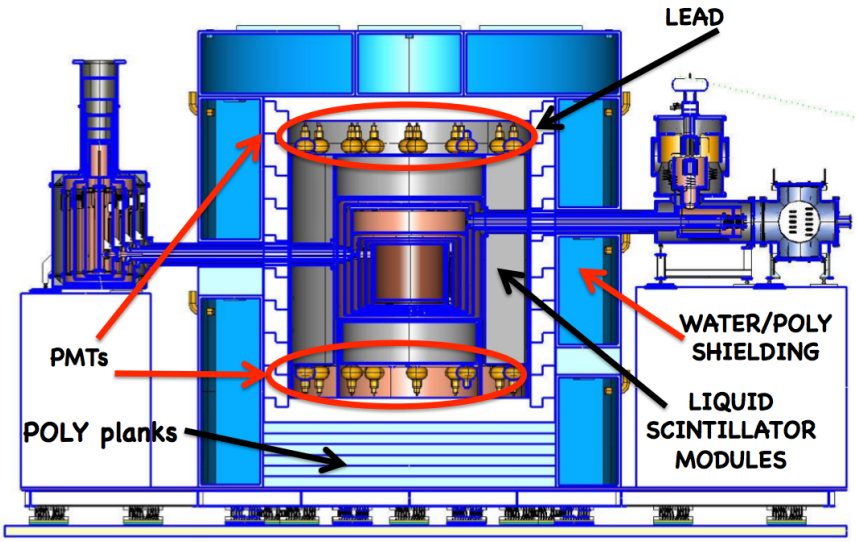

Figure 5.11: This is an illustration of the experiment setup with an active neutron veto layer using liquid scintillator.

with a 225 kg payload, six copper cans, one active neutron veto layer with liquid scintillator, one lead layer, and one polyethylene (and/or water) layer. The radial and top/bottom thickness of the neutron veto layer was 32 inches in this configuration.

Three tank materials each of thickness of 0.25 inches were considered. They were stainless steel, titanium, and acrylic. The densities and contamination levels of these tank materials are shown in Table 5.11. The energy range of interest for nuclear recoil events was [10, 100] keV. For an event to be classified as a nuclear event in the simulation, its ionization energy deposition was required to be less than 5% of its non-ionization energy deposition. For a nuclear recoil event to be classified as a single-scatter nuclear recoil event, it was required that there was no energy deposition larger than 2 keV in any of the other detectors. The energy collection time window was set to be at 10 μs.

The simulation results are shown in Table 5.11. As can be seen, acrylic introduces the lowest nuclear recoil event rates in the detectors, but this result is highly dependent on the low radioactivity levels of ^{238}U, ^{235}U and ^{232}Th used in the calculation. It is the best option

	Stainless Steel		Titanium		Acrylic	
Density [g cm^{-3}]	8.0		4.54		1.18	
Contaminant	U	^{232}Th	U	^{232}Th	U	^{232}Th
Radioactivity Level [mBq kg^{-1}]	15	30	0.25	0.2	0.014	0.005
Total NR [n kg$^{-1}\cdot$ year^{-1}]	4.81E-02	8.48E-02	1.22E-03	1.38E-03	4.34E-06	1.74E-08
Single NR [n kg$^{-1}\cdot$ year^{-1}]	1.31E-02	2.31E-02	3.36E-04	3.77E-04	1.17E-06	4.44E-09

Table 5.11: The total NR and single-scatter NR rates in the detectors from the contaminants in stainless steel, titanium, and acrylic. Natural uranium consists of ∼99.3% ^{238}U and ∼0.7% ^{235}U.

for introducing the least amount of new contamination to the experiment but it requires a high level of cleanness be met when constructing the tank. In addition, acrylic has a low density and as such engineering considerations of the material strength would also need to be addressed before selecting an acrylic vessel.

Stainless steel has the advantage of being the strongest material among the three candidates. However, the neutrons generated from the ^{238}U, ^{235}U and ^{232}Th decay chains in it produce the highest nuclear recoil event rates in the detectors. The radioactive levels of ^{238}U, ^{235}U and ^{232}Th used in the stainless steel in Table 5.11 are about a factor of 10 conservative. Thus, the expected NR rates in detectors from the use of stainless steel could be one order of magnitude lower if considering radioactive levels of one-tenth of the current numbers. These corrected NR rates are acceptable but still not as good as acrylic or titanium.

Titanium has an acceptable nuclear recoil event rate in the detectors and its density is about 3 times higher than that of acrylic. Compared to acrylic and stainless steel, the performance of titanium lies in the middle, which is a good option.

In order to further investigate these three tank material candidates, the performance of vetoing neutron was studied for each one. One million primary particles are simulated for the ^{238}U, ^{235}U and ^{232}Th contaminants in the inner layer of the tank. For the nuclear recoil events generated by neutrons in the detectors, Fig. 5.12 shows the comparison of single-scatter neutron veto efficiencies as a function of energy threshold in a liquid scintillator module filled with 0.12% Gd-doped LAB.

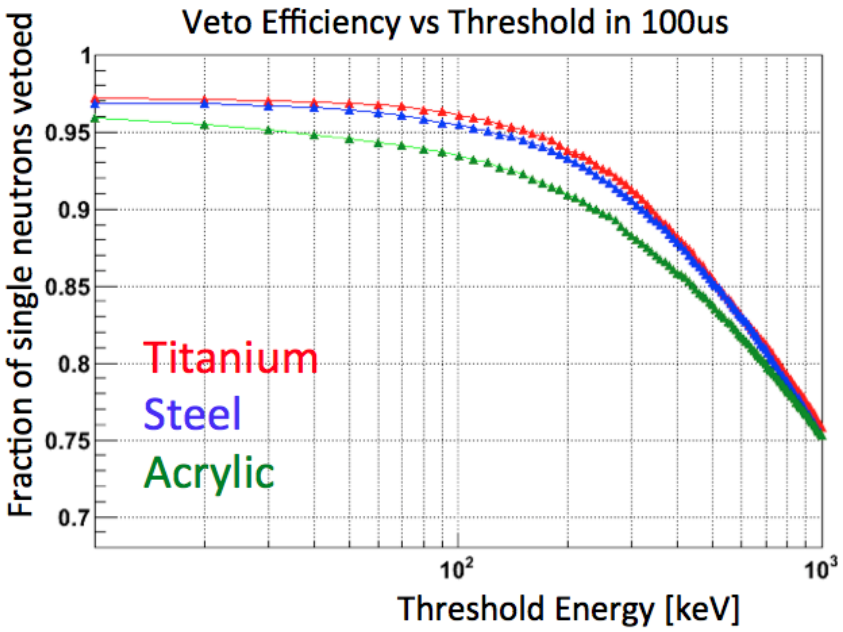

Figure 5.12: Single-scatter neutron veto efficiencies in the 0.12% Gd-doped LAB liquid scintillator module as a function of the energy threshold when using different tank materials (titanium (red), stainless steel (blue) and acrylic (green)). An energy collection time window of 100 μs was applied.

The neutron veto efficiencies using stainless steel and titanium are compatible with each other. Acrylic itself has a higher probability to absorb and reduce neutrons. Thus, neutrons coming from the detector region may get captured in acrylic before reaching the liquid scintillator. This causes a reduction of neutrons entering the veto layer from the experimental setup. A 90% rejection rate is maintained to over 100 keV energy threshold in the liquid scintillator for all three tank material candidates.

At the time of this study, when combining the neutron veto efficiencies (see Fig. 5.12) with the total and single-scatter NR rates in the detectors (see Table 5.11), titanium was considered the most preferred tank material for the active neutron veto layer to hold the liquid scintillator. Its neutron veto efficiency is the highest among the three candidates. The total and single-scatter NR rates introduced by titanium is in an acceptable range. The rates are better than those from stainless steel even after taking into account a conservative factor of 10. Although the rates from acrylic is extremely low, it highly depends on the radioactive levels used for the contaminants. If this high purity was not met at the time of construction, the difference in rates between titanium and acrylic would be reduced. In addition, the density of acrylic is low, causing concern of whether it is strong enough to hold the liquid scintillator. Compared to acrylic, the density of titanium is nearly four times higher, making it a better candidate. Thus, titanium is the best option for the tank construction of a liquid neutron veto system for SuperCDMS SNOLAB.

Chapter 6

Data Sets and Livetime Cuts

Unlike the earlier SuperCDMS Soudan Low Threshold [28] and CDMSlite [61] analyses, which focused their searches on low mass WIMPs interacting in our detectors using subsets of the Soudan data, the SuperCDMS Soudan high mass WIMP search analysis searches for high mass WIMPs using available SuperCDMS data taken between March 2012 and May 2014. The data taken during this period constitute run 133 (R133) and run 134 (R134). This high mass WIMP search analysis attempts to search for WIMPs whose mass is greater than 10 GeV/c^2 while maintaining a near-zero background level in the detectors.

6.1. Raw Livetime and Target Mass

The data used by the high mass WIMP search analysis was collected during a two-year span of the experiment starting in March 2012 and ending in May 2014. During a calibration run in July 2013, the ^{133}Ba source became detached from the deployment wire. To remove the source that was stuck between the icebox and inner poly layer, run 133 was stopped and the fridge was warmed up so that the shielding could be removed in order to retrieve the source. After returning the fridge to base temperature, run 134 data collection started. The SuperCDMS collaboration defines the raw livetime as the time period that its detectors are in an operating mode and ready to record any interaction signal. The cumulative raw WIMP search livetime for the entire run 133 and run 134 data collection periods is ∼534.11 days.

A total of 15 iZIP detectors operated in the SuperCDMS Soudan experiment and the mass of each iZIP detector was ∼0.6 kg. As shown in Fig. 6.1, the 15 detectors are divided into five towers and each tower contains three iZIP detectors. The collaboration employs

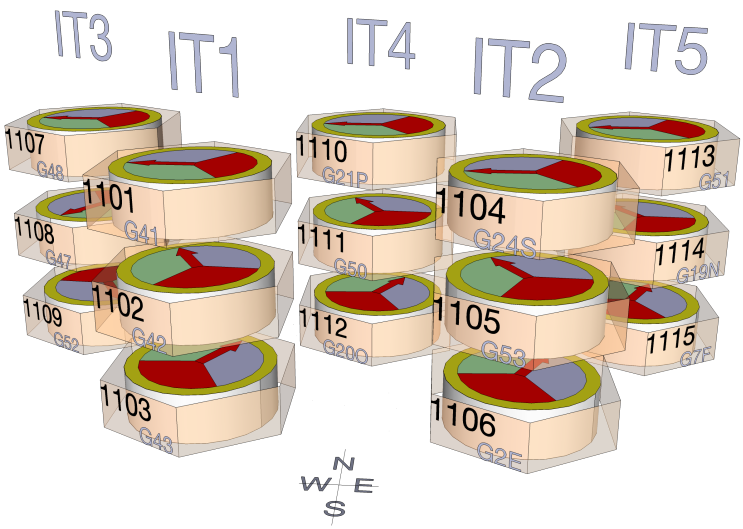

Figure 6.1: This is an illustration of the detector orientation and tower arrangement for the SuperCDMS Soudan experiment. A total of 15 detectors were arranged into 5 towers, each tower containing three detectors. Detector names using two different nomenclatures are listed on each detector.

multiple naming schemes to refer to a particular detector. The first scheme takes the form iT#Z#, where "i" indicates that the tower contains iZIP detectors, T# indicates the tower number and Z# indicates the detector position in the tower. Detector 1 is the detector at the top of the tower and detector 3 is at the bottom of the tower. The second scheme labels each detector as 11##, where "11" indicates that it is an iZIP style detector and ## is a number from 1 to 15, where 1 is the top detector in tower 1, 15 is the bottom detector in tower 5, and each detector is sequentially numbered in between. For example, the middle detector in tower 2 is referred to as both iT2Z2 and 1105.

6.2. Particle Identification

In SuperCDMS, various particles are classified into three categories: bulk electron recoils, surface electron recoils, and nuclear recoils. Figure 6.2 shows how these three categories of events distribute in the yield (`ytNF`) vs phonon energy (`precoiltNF`) plane.

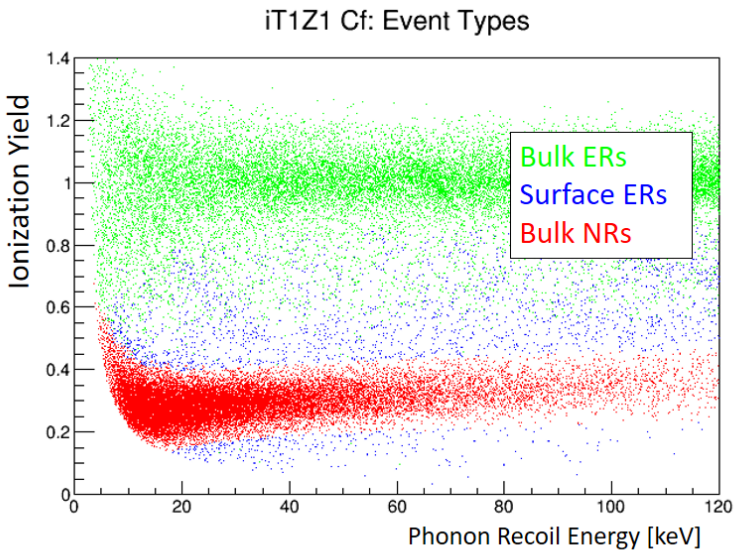

Figure 6.2: This is an illustration of the yield-energy distributions for bulk ERs, surface ERs, and NRs in iT1Z1 in the Cf data set. The yield of surface ERs can have any value from 1 down to 0, which covers the yield region of the bulk NRs. Thus, a surface ER can fall into the NR band and mimic a WIMP signal event.

The electron recoil (ER) band is defined using the ^{133}Ba calibration data. Events that fall into the 3σ ER band are classified as bulk electron recoils [62]. The nuclear recoil (NR) band is defined using the ^{252}Cf calibration data. Events that fall into the 3σ NR band are classified as nuclear recoils [62]. If an electron recoil event locates below the lower 3σ ER band, it is classified as a surface electron recoil event. Thus, the surface electron recoils can have a chance to leak into the NR band and mimic a nuclear recoil event.

6.3. Blinding Scheme

The high mass WIMP search analysis is a blinded analysis. The entire data with no events removed from analyzers is referred to as "restricted" WIMP search data in SuperCDMS. No analyzers have access to this data until the analysis development has been frozen and the final stage for unblinding is ready. Since WIMPs may exist in this data, a separate "unrestricted" data set is generated. This data has a blinding scheme applied that removes all signal-like events. This unrestricted data set is used to develop the analysis.

Because the probability for a WIMP to interact twice in the detectors is nearly zero, a WIMP candidate event needs to be a single-scatter nuclear recoil event. Several selection criteria are applied to determine whether an event is signal-like or not. This event cannot be an electronic glitch event or a low-frequency event. It cannot be recorded within 25 μs of an event in the muon veto system. The phonon energy has to be less than 150 keV but larger than the noise. It needs to deposit most of its energy in the inner channel and have its charge energy symmetrically distributed on the top and bottom face of the detector. Last but not least, it has to be a nuclear recoil event without any energy deposition in a second detector. A summary of the blinding criteria is listed in Table 6.1.

Cut	**Definition**
No glitch	$\sim$`cGlitch_133` and $\sim$`cGlitch1_v53`
No LF noise	$\sim$`cLFnoise1_v53`
No muon veto signal	`VTTime20` $\notin$ [-25, 0] μs for a given event
Upper energy limit	`precoilsum0F` $<$ 150 keV
Radial fiducial volume	(`qi10F` $> \mu + 2\sigma$ or `qo10F` $< \mu + 8\sigma$) and
	(`qi20F` $> \mu + 2\sigma$ or `qo20F` $< \mu + 8\sigma$)
Charge symmetry	(`qsum10F` $> \mu + 2\sigma$ or `qsum20F` $< \mu + 8\sigma$) and
	(`qsum20F` $> \mu + 2\sigma$ or `qsum10F` $< \mu + 8\sigma$)
Nuclear recoil band	`ysum0F` $\in [\mu - 3\sigma, \mu + 3\sigma]$ and `precoilsum0F` $>$ 0 keV
Minimum phonon energy	`psum0F` $> \mu + 3\sigma$
Single-scatter event	$\sim$`cPmultTight_blind_v53`

Table 6.1: Summary of the cuts required to blind the conventional WIMP search data [63].

As discussed in Chapter 4, the possible background event types that could appear are neutrons, gammas, gamma-induced electrons, alphas, betas, and ^{206}Pb nucleus. These backgrounds are grouped into three categories: nuclear recoil, surface electron recoil and bulk electron recoil events. In order to keep the cut development and tuning unbiased, analyzers

work on both this "permitted" WIMP search data and the calibration data to gain knowledge and model the various background particles in SuperCDMS detectors.

6.4. Detector Calibration

When an interaction occurs in a detector, the signals are read out as pulses. The amplitude and the area under a pulse do not directly provide any physical meaning to the analyzer. In order to make this event information more meaningful, SuperCDMS also takes calibration data using radioactive sources. In R133 and R134, removable ^{133}Ba, ^{252}Cf sources and two ^{210}Pb source plates were used.

^{133}Ba sources provide a source of gamma particles to the detectors. Its spectrum has three gamma peaks over 300 keV (i.e. 302.9, 356.0 and 383.3 keV), which allow the experiment to calibrate its detectors. They were inserted through the shielding layers to the outside of the icebox via two tubes in parallel to the two stems. Data was taken routinely with the ^{133}Ba source throughout the entire high mass WIMP search data period, which enables the experiment to monitor the stability of the detector responses. In the mean time, due to the high gamma rate from the ^{133}Ba source, this calibration data is also useful for studies of the gamma background.

^{252}Cf source is a neutron source mainly used to learn the detector response to neutron-induced nuclear recoil events. Since a single-scatter nuclear recoil event produced by a neutron is indistinguishable from that produced by a WIMP, ^{252}Cf calibration data is an excellent proxy for use in defining the WIMP signal region.

This type of data is not taken as often as the ^{133}Ba calibration data, because the neutrons from ^{252}Cf activate the Ge nucleus. When the activated nucleus decays, a gamma is emitted. The half life of this Ge activation is about 11 days. Thus, even with the ^{252}Cf source removed, the WIMP search data that are collected during the following weeks will

have elevated background levels. Data quality checks are performed on this post-Cf period to determine when the Ge activation becomes insignificant to the WIMP search. This post-Cf data within the WIMP search data is not included in the final high mass WIMP search analysis.

In order to understand the detector response to the ^{210}Pb surface contamination, two silicon wafers implanted with ^{210}Pb isotopes were installed. One was placed above iT3Z1, and the other was placed below iT3Z3. As a result of the installation of these two ^{210}Pb plates, the WIMP search data on iT3Z1 side 1 and iT3Z3 side 2 are not included in the final analysis.

6.4.1. Pile-up

The gamma rate is very high resulting in pileup when both ^{133}Ba sources are fully inserted into the calibration tubes. Pile-up occurs when two pulses are so near in time that they overlap with each other. These pile-up events are removed by the good event selection cut, which then results in a reduction of gamma particle statistics.

In order to maintain comparable statistics within the interested energy region while potentially reducing the pile-up event rate, a study on the ^{133}Ba source positions was conducted. In SuperCDMS, a data series normally contained data collected in $\sim$3 hours detector operation time. This investigation studied the pile-up rate when the sources were fully inserted and inserted at positions 1-inch, 2-inches, 4-inches, 8-inches and 10-inches out from fully-inserted. The statistics and run times of the investigated data series are shown in Table 6.2 and Fig. 6.3.

The events were divided into four categories based on each event's ionization yield and phonon energy. Category 1 contained low energy and low yield, category 2 contained low energy and high yield, category 3 contained high energy and low yield, category 4 contained

Data Set	Series Number	Stats	Configuration
1	11404090811	304596	Both sources fully inserted
2	11404091129	308481	Both sources fully inserted
3	11404150805	297358	Both 1-inch out
4	11404151122	295762	Both 2-inches out
5	11404160748	241896	Both 4-inches out
6	11404161105	57900	Both 8-inches out
7	11404180911	20462	Both 8-inches out
8	11404181343	20561	Both 8-inches out
9	11404220909	10016	Both 10-inches out
10	11404221226	10733	Both 10-inches out

Table 6.2: Stats and configuration of each examined data series.

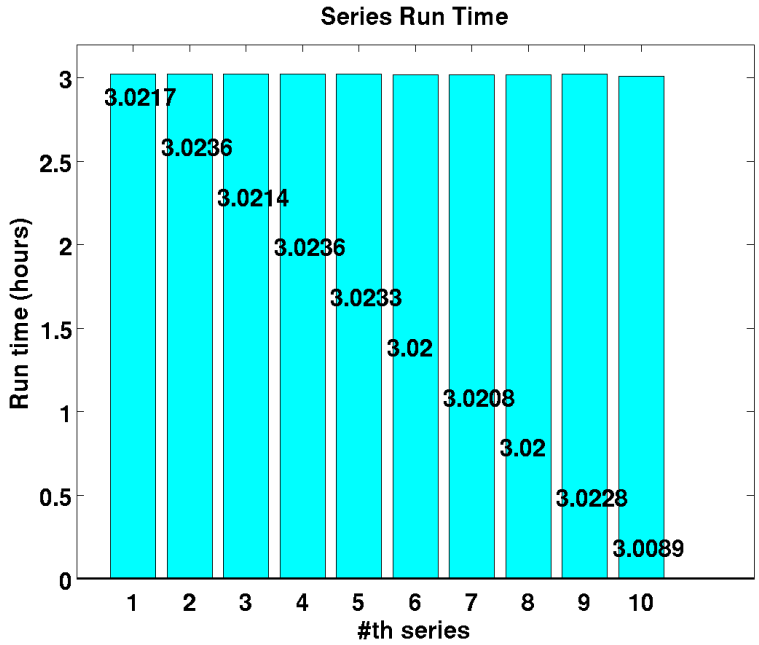

Figure 6.3: The run time for each data series in Table 6.2 is approximately 3 hours.

high energy and high yield as illustrated in Table 6.3 and Fig. 6.4. Data series 2-10 are compared with data series 1, which was taken with the source fully inserted, on a series-by-series basis respectively.

	10 - 80 keV	**80 - 150 keV**
yield > 0.8	Region 2	Region 4
yield < 0.8	Region 1	Region 3

Table 6.3: The division of four regions in the ionization yield vs phonon energy plane.

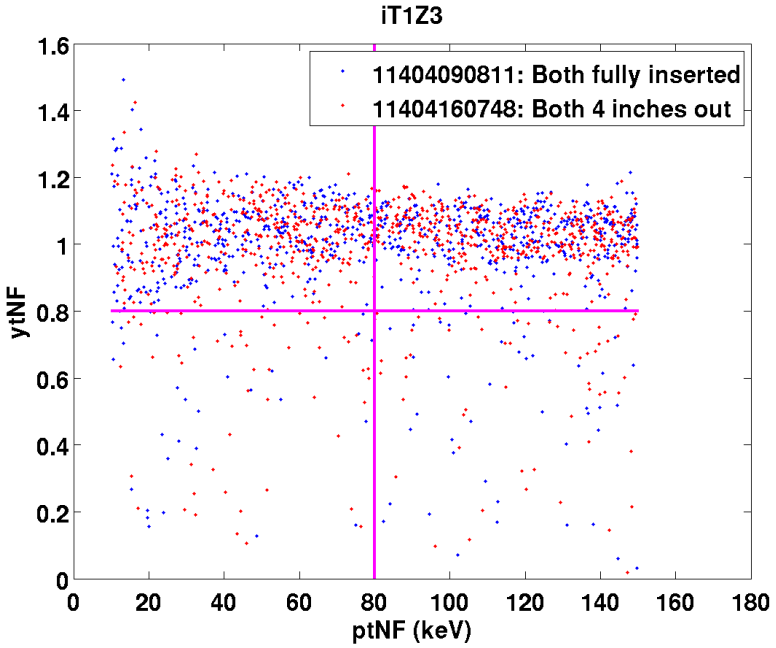

Figure 6.4: The ionization yield [ytNF] vs total phonon energy [ptNF] plane is divided into four regions for statistics comparison.

The statistics (see Fig. 6.5) and distributions (see Fig. 6.6) of 10 different physics quantities were examined and compared in all four regions. These quantities include charge energy, charge radial and depth partition, phonon energy, phonon radial and depth partition, phonon depth signal time delay and ionization yield. Figure 6.6 shows the distribution of events on side 1 as a function of radial partition for detector iT3Z3. Radial partition is defined as the

outer charge energy divided by the summed charge energy on the same side. Comparable statistics are maintained for the 2-inches and 4-inches configurations. When retracting both sources further out, the 8-inches and 10-inches configurations show significant decrease in statistics.

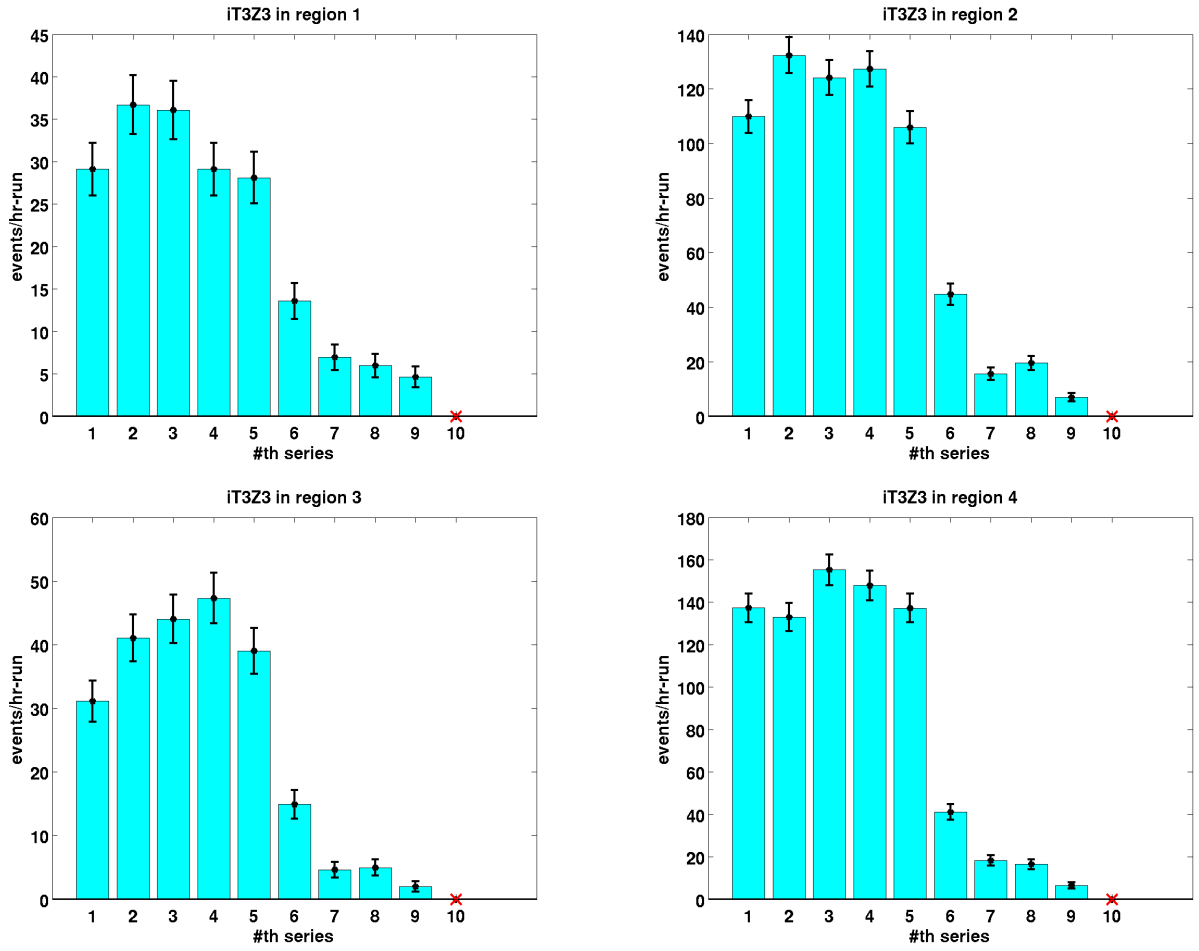

Figure 6.5: Statistics comparison among different ^{133}Ba source configurations show that retracting the sources back as far as 4-inches maintains comparable statistics in all four regions. Data series 10 has no data in iT3Z3 due to the existence of abnormal energy χ^2 values.

Thus, if the statistics of gamma particles need to be maintained in the 10-150 keV energy range while minimizing the affect from pile-up events in the ^{133}Ba calibration, a retraction up to 4 inches out of both ^{133}Ba sources is a probable option to achieve this goal. After

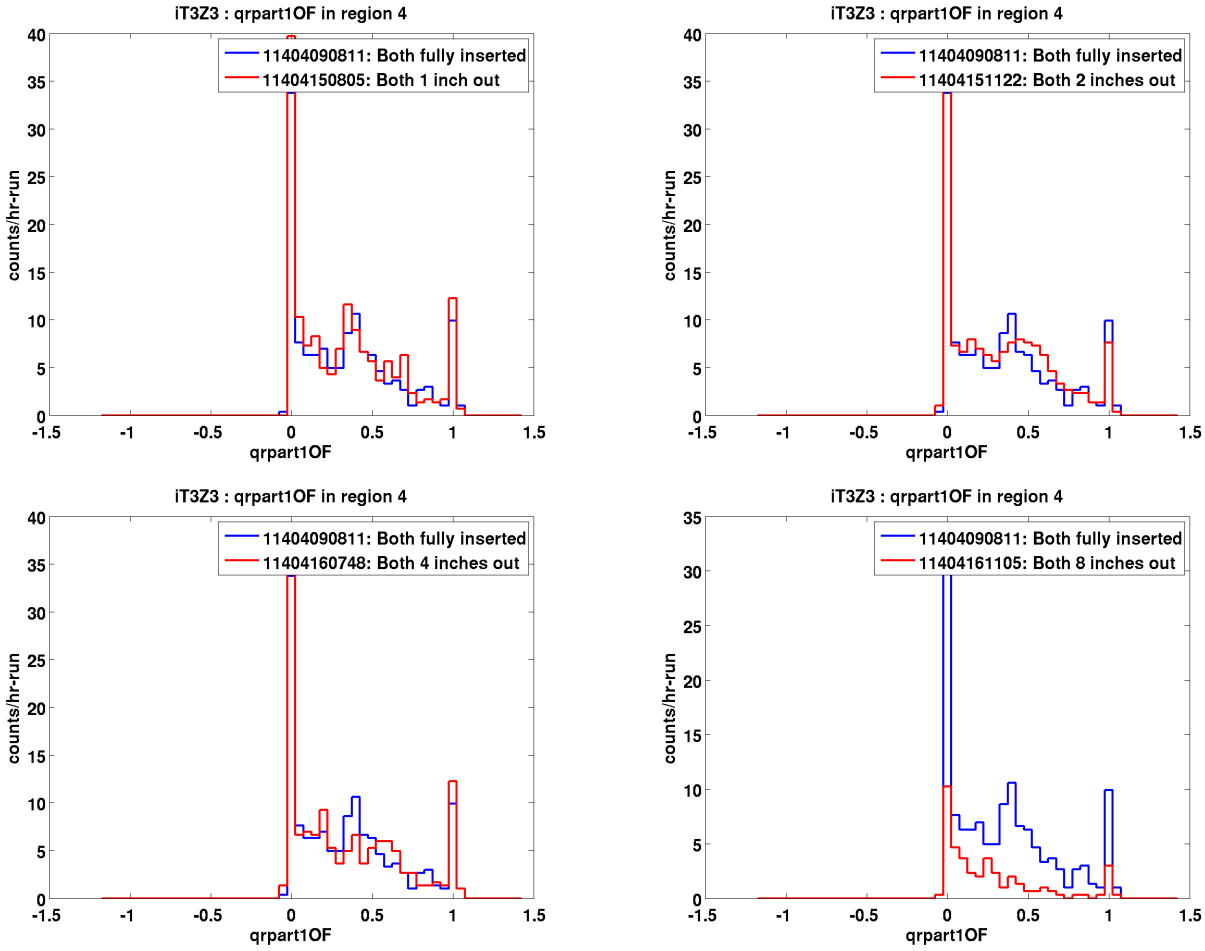

Figure 6.6: Distribution comparison between four ^{133}Ba source configurations and the fully-inserted configuration. For the radial charge energy partition quantity on side 1 [`qrpart1OF`] in region 4, the 1-inch (top left), 2-inches (top right) and 4-inches (bottom left) configurations show comparable statistics to the fully-inserted configuration, while the 8-inches (bottom right) configuration shows an obvious decrease in statistics.

finishing the data collection of run 134, ^{133}Ba calibration data were taken for over a month to obtain high statistics of gamma particles for the high mass WIMP search analysis. Two ^{133}Ba sources were inserted into the two tubes with retractions not greater than 4 inches during this period.

6.4.2. Charge and Phonon Calibration

Detector calibration is an important process to convert the pulses into some physical quantities. Since the iZIP detectors have both ionization and phonon signal channels, both channels must be calibrated.

The ^{133}Ba calibration data is used in SuperCDMS for the charge calibration [64, 65]. Due to existence of the Compton plateau at low energy the three peaks at 302.9, 356.0 and 383.3 keV are used to calibrate the ionization channels. Once charge calibration is done, the next step is to do the phonon calibration [66], which involves a relative gain compensation of all eight phonon channels and an absolute phonon calibration using the ionization yield from bulk gammas. The eight phonon signal collection channels on each detector are designed to have the same surface coverage. Since phonons are not affected by the external electric field and migrate isotropically, the phonon energy collected in each phonon channel after the phonons become ballistic is expected to be the same. In practice, the gains of different channels are not the same and this effect needs to be corrected. In order to align the gains on a given detector, the eight phonon channels are calibrated amongst themselves, which means that one phonon channel is selected as a reference channel and then the gains of the other seven phonon channels are aligned relatively to it. The gain difference is believed to result from the readout process or detector fabrication activities. After the relative gain compensation, a total phonon signal can be obtained by summing the phonon signals collected in different channels from an event. Since the ionization yield for bulk gammas is set to one in the detectors, a phonon energy quantity that is estimated from the charge energy can be derived.

6.5. Data Selection

When the detectors were in operation, the data acquisition (DAQ) system recorded every event that passed certain triggering requirements. These events were stored as raw data. Later they was processed into calibrated data. Selection criteria ("cuts") were developed to select events that are considered good for the following data analysis. Short descriptions of the functionalities of a majority of cuts can be found in Appendix B.

Two new cuts that were specific developed for this high mass WIMP search analysis are selected and highlighted below. They both affect the livetime of the data but one cuts on a continuous time period while the other cuts on an event-by-event basis. The data series or events removed are considered not suitable to search for WIMP signals.

a) Good Random χ^2 cut [cGoodRandomChi2_v53_HT]

The cGoodRandomChi2_v53_HT cut removes data on a series basis. Thus, the total livetime of events in a series is removed. It is applied to select data series whose χ^2 values for charge and phonon energies from optimal filter behave normally.

In order to obtain the charge energy of an event, a charge pulse template is derived from a selection of events with known good charge pulses. The charge energies of other events are then estimated by fitting their pulses with this template using an optimal filter in frequency space. Since the number of time bins for an inner or outer charge pulse is 2048 (i.e. 2^{11}), the χ^2 value of the charge energy (Q[I/O]S[1/2]OFChisq) from a good event is expected to be centered around 2047 (i.e. nDOF-1). For the summed inner and outer energy on one detector side, a χ^2 value near 4094 for QS[1/2]OFChisq is considered good. However, through the normal data taking periods, several data series were observed to have abnormally degraded charge energy χ^2 distributions (see Fig. 6.7). This behavior was also observed in the phonon energy χ^2 distributions (PTNFChisq).

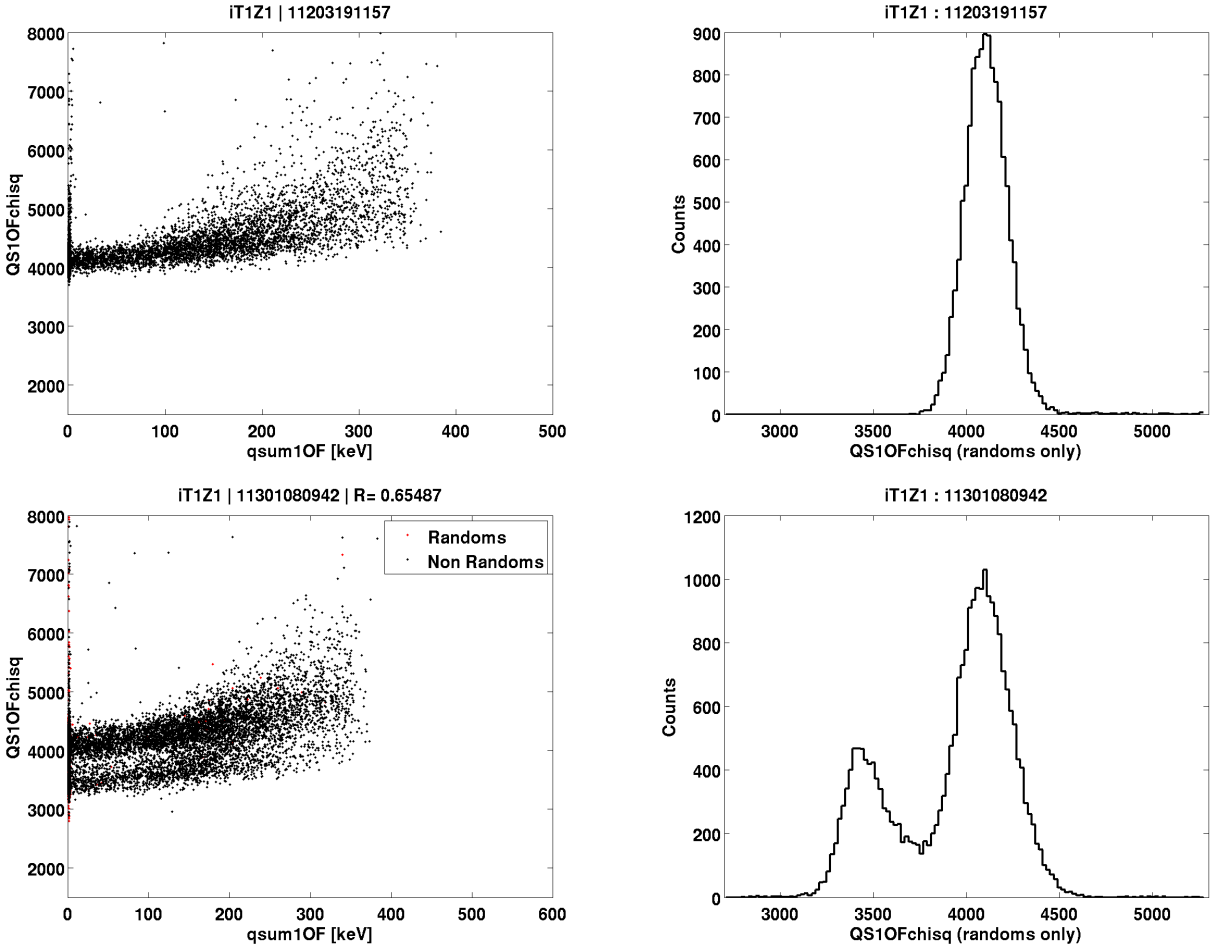

Figure 6.7: The top left and right plots are examples of a good charge energy χ^2 distribution. The bottom left and right plots are examples of a degraded charge energy χ^2 distribution. `QS1OFchisq` is the side 1 charge energy χ^2 quantity. `qsum1OF` is the summed side 1 charge energy.

As energy increases, the χ^2 values start to rise upwards. This is due to the sharp feature in the rising edge of this high energy charge pulse. In order to develop a selection cut that is not affected too much by the change of charge energy, random trigger events are chosen. Random trigger events are issued periodically by the DAQ system throughout a data collection run to monitor the noise level. They are expected to be consistent with the noise and have energies close to zero, which provides an unshifted peak of the χ^2 values.

A ratio cut based on the ratio of random event statistics near the expected χ^2 peak over all random events was studied. Three data series with good charge energy χ^2 distributions were selected to develop statistics acceptance boundaries. A Gaussian was used to fit the peak in each series to achieve the mean value and the standard deviation (see Fig. 6.8). The $\mu \pm 3\sigma$ ranges among these three series were compared and the narrowest range was selected as the template.

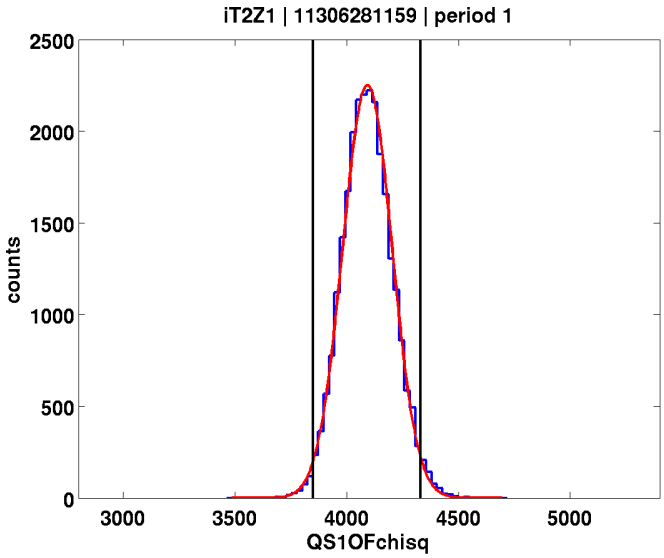

Figure 6.8: A Gaussian fit is applied to the χ^2 peak, where `QS1OFchisq` is the side 1 charge energy χ^2 quantity. The $\mu \pm 3\sigma$ boundaries are compared among three selected data series with good performance.

	iT1	**iT2**	**iT3**	**iT4**	**iT5**
Z1	274.19(95.11%)	272.85(94.65%)	271.90(94.31%)	274.03(95.06%)	283.76(98.43%)
Z2	281.55(97.66%)	270.13(93.70%)	274.85(95.33%)	279.66(97.01%)	285.44(99.01%)
Z3	280.84(97.42%)	277.10(96.12%)	276.76(96.00%)	280.35(97.25%)	276.81(96.02%)

Table 6.4: Detector livetime after the application of the `cGoodRandomChi2_v53_HT` cut on the R133 WIMP search data.

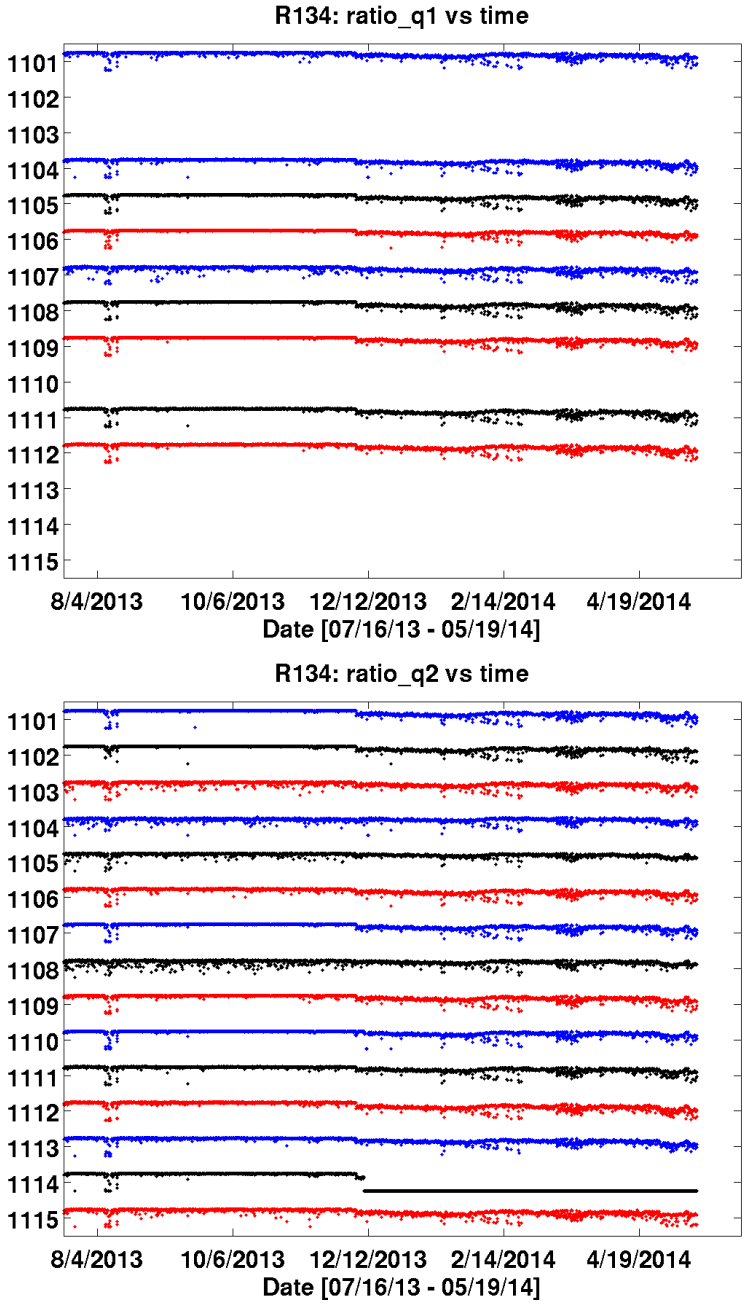

Figure 6.9: The ratios of `QS1OFChisq` (top) and `QS2OFChisq` (bottom) in run 134 (R134) for all functional charge channels in the 15 detectors. The ratio of a charge energy χ^2 quantity is defined as the random triggered events within a range near the peak over all random triggered events.

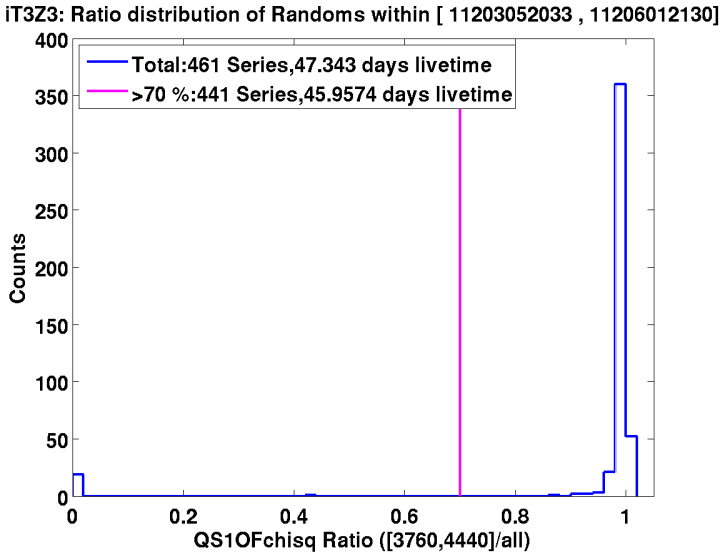

Figure 6.10: A ratio cut is set at 0.7 (i.e. 70%) for iT3Z3 (pink vertical line). 20 data series have `QS1OFChisq` statistics less than 70 % within [3760, 4440] are removed. `QS1OFchisq` is the side 1 charge energy χ^2 quantity. The ratio of a charge energy χ^2 quantity is defined as the random triggered events within a range near the peak over all random triggered events.

	iT1	**iT2**	**iT3**	**iT4**	**iT5**
Z1	197.58(94.62%)	195.96(93.84%)	194.88(93.32%)	191.00(91.46%)	202.14(96.80%)
Z2	201.68(96.58%)	201.03(96.27%)	193.59(92.70%)	198.88(95.24%)	206.12(98.75%)
Z3	197.60(94.62%)	199.90(95.73%)	198.97(95.28%)	195.38(93.56%)	190.12(91.04%)

Table 6.5: Detector livetime after the application of the `cGoodRandomChi2_v53_HT` cut on the R134 WIMP search data.

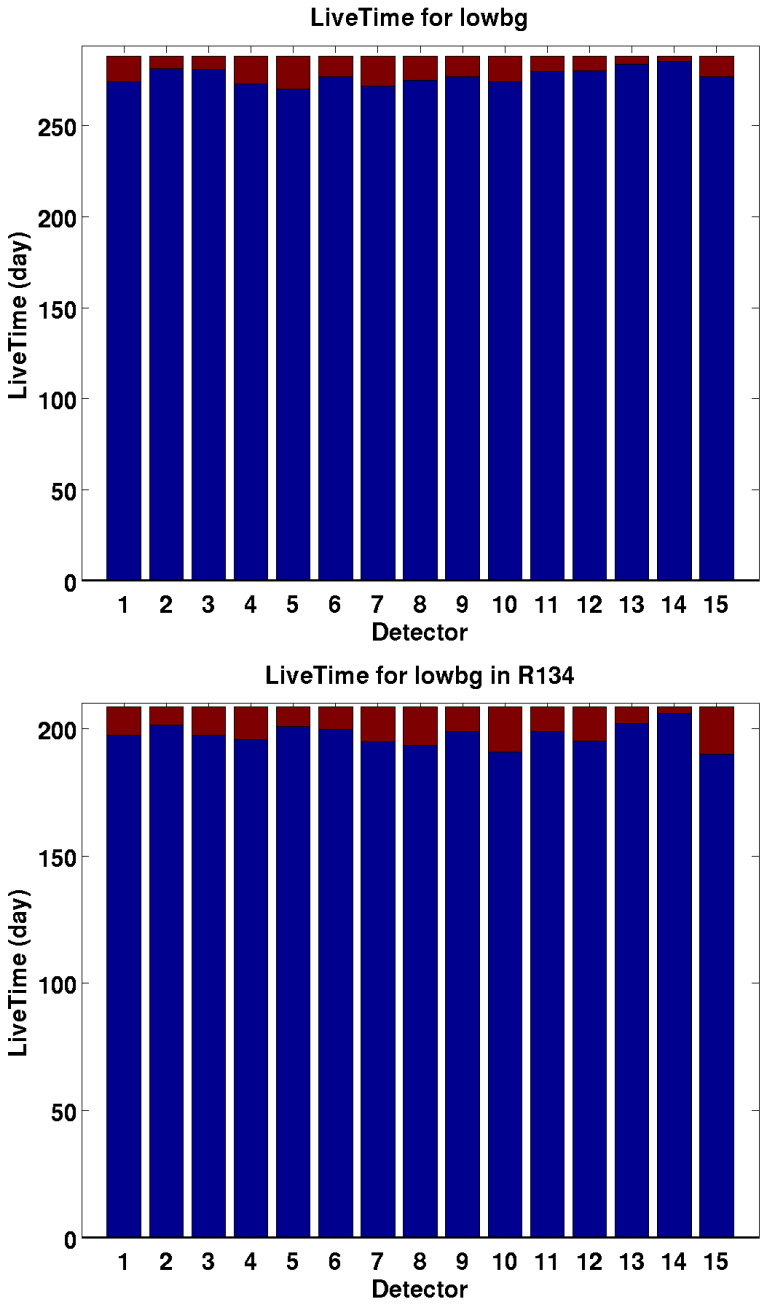

Figure 6.11: This plot illustrates the effect of the `cGoodRandomChi2_v53_HT` cut on the livetime of R133 and R134 WIMP search (lowbg) data.

The ratios of random events within this range over all random events for all data series were calculated. Its distribution as a function of the data collection time is shown in Fig. 6.9. Correlation of degradations among all detectors can be observed in several time periods, indicating that a global effect causes the extra observed χ^2 peak.

Ratio cuts can be set for `QS1OFChisq`, `QS2OFChisq` and `PTNFChisq` respectively in all detectors. Figure 6.10 illustrates a ratio cut for `QS1OFChisq` in iT3Z3. In order to ensure unaffected charge and phonon energy estimations in a detector, a data series is required to pass all three ratio cuts. An average of 5% livetime is removed in R133 and R134 respectively due to this abnormal energy χ^2 behavior, which is consistent with the expectation. The retaining livetime after the application of the `cGoodRandomChi2_v53_HT` cut is shown in Fig. 6.11, Table 6.4 and Table 6.5.

b) No Trigger Enable cut [`cNoTrigEnable_v53`]

The `cNoTrigEnable_v53` cut removes livetime on an event basis. It is applied to remove the group of events whose livetime is not calculated correctly and resulted in a zero value by the DAQ system.

The `livetime` RQ is used to record the livetime of every event in the data (see Table 3.2). During the ^{133}Ba source position study (see Section 6.4.1), we observed an average of 20% of events in each Ba data series removed by an event selection cut `livetime>0` (see Table 6.6). This cut was traditionally used to remove non-physical events in the data. However, the number of events removed by this `livetime>0` cut was surprisingly high and demanded further investigation.

Performances and distributions between the non-zero livetime events and zero livetime events were checked in various parameter spaces for clues to the cause of the anomalous

Series Number	Total Events	Zero livetime Events	Fraction
11309200802	259164	60168	23.22%
11309201119	283401	65362	23.06%
11404240953	266552	36596	13.73%
11405050936	285183	97340	34.13%

Table 6.6: The fractions of zero livetime events in some example Ba data sets.

behavior. Figure 6.12 illustrates two of these distribution checks. The zero livetime events occurred uniformly throughout the entire series and do not burst in a particular period. They are distributed in a similar pattern as events with non-zero livetime in the yield vs energy plane and do not grouped in a restricted area. No difference was observed between these two groups of events.

The `livetime` distribution was also checked by combining all events in the Ba data as illustrated in Fig. 6.13. These two groups of events formed a quasi exponential decrease together. Another check on the `TimeBetween`, which is defined as the time interval between two event triggers, was performed as well. The `TimeBetween` values of the zero livetime events are distributed within the range of those of the non-zero livetime events and do not fall below 20 ms. No abnormal behavior was observed between these two groups of events.

After a series of performance checks and comparisons, there is no support for removing these zero livetime events as non-physical events. They behave similar as those non-zero livetime events. Thus, the fraction of events with zero livetime was calculated for the WIMP search data, Ba calibration data and Cf calibration data. The Ba calibration suffered significantly more efficiency loss as shown in Table 6.7.

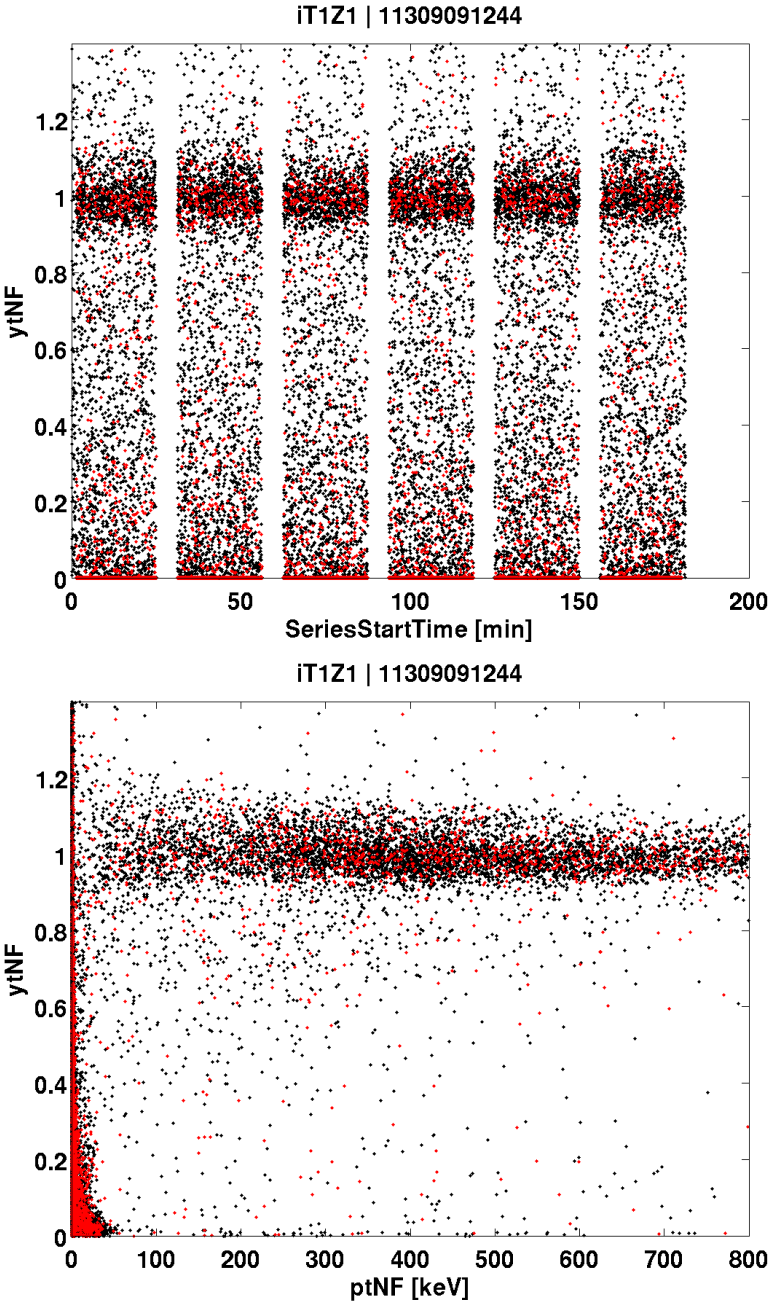

Figure 6.12: The top plot is the yield [ytNF] distribution as a function of data collection time for non-zero livetime events (black dots) and zero livetime events (red dots). The bottom plot is yield [ytNF] vs phonon energy [ptNF] plane. Both plots show no difference in the distributions between these two groups of events.

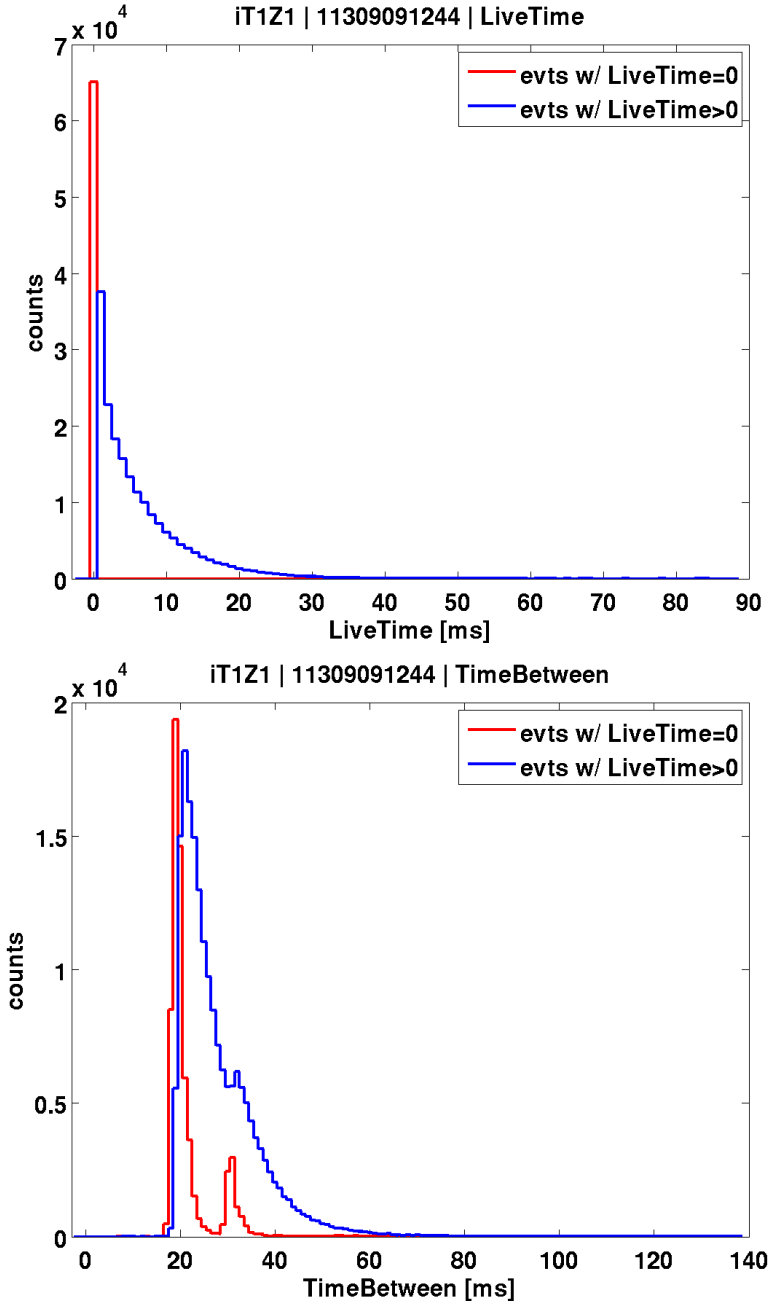

Figure 6.13: The top plot shows the `livetime` distribution of all events. These two groups of events form a quasi exponential decrease together. The bottom plot illustrates differences in the triggering between non-zero livetime events (blue) and zero livetime events (red). The `TimeBetween` values of the zero livetime events are distributed within the range of those of the non-zero livetime events. `TimeBetween` is a time measurement between two triggers. It equals to the deadtime of DAQ following last event trigger plus the livetime of the current event.

Data Sets	Total Events	Zero livetime Events	Fraction
R133 WS	18477856	490054	2.65%
R134 WS	14217827	345553	2.43%
R133 Ba	71382667	14207771	19.90%
R134 Ba	55934618	14949154	26.73%
R133 Cf	1548175	120464	7.78%
R134 Cf	2514154	114403	4.55%

Table 6.7: The fractions of zero livetime events in WIMP search (WS), Ba and Cf data, calculated for data runs 133 and 134.

In order to decide whether these zero livetime events should be included in the data analysis or not, an understanding of their physical meaning is required. This lead to an investigation into how the DAQ system records trigger information for each event.

When an event triggers, the DAQ system needs some amount of time to read out the event information. During this short period of time, the DAQ is immune to all other event triggers. This amount of time is called deadtime. When DAQ finishes recording the current event and is ready to record the next event, a global command called TrigEnable [1] is issued to all detectors. When the next event triggers one of the detectors, the DAQ will issue a global trigger to every detector and start reading out this event's information. At this point the DAQ is in another deadtime period. The time period between the global trigger and the TrigEnable command is defined as this event's livetime.

$$livetime = (global\ trigger\ time) - (TrigEnable\ time)$$

Closer examination of the calculation above reveals what exactly happens to the zero livetime events. When the DAQ system records the trigger time information, it stores this information in units of microsecond. When calculating the `livetime` RQ, a `floor` function

[1] Trigger Enable

is applied to the result to convert it to a unit of millisecond. This `floor` function always rounds the result towards negative infinity, i.e. the results of floor (2.9 ms) and floor (2.2 ms) are both equal to 2 ms. Thus, if an event has a livetime number between 0 and 999 μs, its livetime becomes a zero once its `livetime` RQ is constructed. This means that the livetime of every event in the WIMP search and calibration data is underestimated up to an amount of 999 μs. As a result, the total livetime of the entire data set is underestimated as well. This means that a livetime correction is needed on not only the zero livetime events, but every event.

In order to retrieve the "missing" livetime due to the rounding from μs to ms when constructing the `livetime` RQ, physics quantities for the global trigger and the TrigEnable command with trigger time information stored in units of microsecond are needed.

The history buffer of the DAQ can store up to 100 triggers. If the number of triggers between the TrigEnable command and the global trigger is less than 99, the livetime of an event can be correctly calculated. All events in this case can have their livetimes corrected up to an amount of 999 μs. The history buffer has a circular buffer system, which means that after the TrigEnable command is issued if there are 99 triggers and no global trigger has been issued, the 100th trigger will be stored in the first spot and erase TrigEnable information. In the latter case, the DAQ cannot calculate the livetime of an event and it will set its livetime to zero. This group of events are the actual zero livetime events and their livetimes cannot be corrected.

There are five different energy thresholds in an event trigger. The charge channel has two levels of thresholds called `Qlow`, `Qhigh`. The phonon channel has three levels of thresholds called `Pwhisper`, `Plow`, and `Phigh`. The energy thresholds vary from channel-to-channel. For a given detector, not all five thresholds are used for event triggering. For example, if a

detector is selected to trigger on `Plow`, even there are tens of `PWhisper` triggers after the TrigEnable command, the global trigger would still not be issued by the DAQ.

Two RQs are selected and used in the livetime correction. The first RQ called `T*TGTime##` is used to store time information of ten triggers for a given event in each detector in units of microsecond. The "*" represents the tower number and the "`##`" is a number that varies from 16 to 25 and represents trigger timing information. The time of the global trigger is stored in `T*TGTime20`. Thus, `##`=16-19 hold the timing information for the four triggers recorded before the global trigger, and `##`=21-25 stores timing information about the five triggers occurring after the global trigger. The second RQ called `T*TGMask##` is used to store information of ten triggers in a form of 36 bit binary number (0 or 1) for each event. The meaning of each bit is explained in Table 6.8.

	DIB1	**DIB2**	**DIB3**	**DIB4**	**DIB5**	**DIB6**	**Others**
`Qhigh`	0	5	10	15	20	25	
`Qlow`	1	6	11	16	21	26	
`Phigh`	2	7	12	17	22	27	33=Veto Multiplicity Trigger
`Plow`	3	8	13	18	23	28	34=Global
`Pwhisper`	4	9	14	19	24	29	35=Random

Table 6.8: The definition of each bit information in `T*TGMask##` RQ.

Because the history buffer is hard to access, a moderated livetime correction is implemented based only on the four triggers before the global trigger. Thus, if a TrigEnable command is issued within four triggers before the global trigger of an event, bit 34 of at least one of the `T*TGMask##` with `##`=16-19 should have a value of 1. In this case, a livetime in units of microsecond could be recalculated for all events, including those zero livetime events.

In the case that the TrigEnable bit does not exist within the last four triggers before the global trigger, if it is a non-zero livetime event, its livetime value still uses its `livetime` value; if it is a zero livetime event, it would get tagged and removed. In the latter situation, the TrigEnable bit is missing due to the high trigger rate before the global trigger.

Data Sets	**Total Events**	**Zero livetime Events**	**No TrigEnable**
R133 WS	18477856	490054	7 (155236)
R134 WS	14217827	345553	2
R133 Ba	71382667	14207771	18
R134 Ba	55934618	14949154	5
R133 Cf	1548175	120464	1
R134 Cf	2514154	114403	1

Table 6.9: Numbers of real zero livetime events without TrigEnable bits found. For R133 WIMP search data, 155236 events with no TrigEnable bits found occur in five out of 39 data series taken between 2012/07/31 and 2012/08/14. There were many tests taking place onsite in this period. Thus, these five data series were removed entirely. This leaves only seven events in the remaining R133 WIMP search data with no TrigEnable bits found.

Compared to the third column in Table 6.9, nearly 100% of the zero livetime events retrieve their true livetimes back in units of microsecond. In addition to increasing the statistics of the WIMP search and Ba and Cf calibration data, the event livetime and total livetime of the experiment get corrected as shown in Table 6.10.

Data Sets	**livetime (day)**	**Corrected livetime (day)**	**Fraction**
R133 WS	287.19	287.25	0.019%
R134 WS	208.82	208.90	0.038%
R133 Ba	7.34	7.74	5.38%
R134 Ba	4.62	4.92	6.62%
R133 Cf	0.45	0.46	1.93%
R134 Cf	1.42	1.44	1.01%

Table 6.10: The corrected livetime for each data set.

Chapter 7

High Mass WIMP Search

The SuperCDMS experiment searches for WIMPs in a wide mass range from a few GeV/c^2 to several hundreds GeV/c^2. Since the detector response and backgrounds vary according to the energy deposited in the crystal, especially for small energy depositions, different analysis strategies are used when searching for WIMPs with different masses. This chapter describes an analysis conducted with a focus on WIMPs whose masses are above 10 GeV/c^2 but below 1 TeV/c^2.

This high mass WIMP search uses the SuperCDMS Soudan data with a raw exposure of 1657.54 kg-days collected between March 2012 and May 2014. An analysis based on a profile likelihood ratio technique is performed on this data and an exclusion limit is set on the spin-independent WIMP-nucleon cross section at 1.32 $\times 10^{-44}$ cm^2 for a 75 GeV/c^2 WIMP at a 90% confidence level.

7.1. Event selection

During the experiment operation, several detectors experienced shorts in either ionization collection channels, phonon collection channels, or both. Such issues affect these detector's ability to attain good fiducialization or discrimination between signal and background events. A total of five iZIP detectors were not included in the high mass WIMP search analysis. These detectors and their issues were summarized in Table 7.1.

The remaining ten best performing detectors were selected for the high mass WIMP search analysis as shown in Table 7.2. Although they were mostly free of channel shorts, a few of the detectors had issues that required special consideration (see Table 7.3). The top

half of iT3Z1 and the bottom half of iT3Z3 were excluded from the analysis because of the existence of lead source plates.

Detector	Ionization Shorts	Phonon Shorts
iT1Z2	inner and outer channels, top face	channels A and C, bottom face
iT1Z3	inner and outer channels, top face	channel A, top face
iT4Z1	inner channel, top face	
iT5Z1	inner and outer channels, top face	channel A, top face
iT5Z3	outer channel, top face	channel C, bottom face

Table 7.1: Shorts that prevent these five detectors to be included in the final high mass WIMP search analysis.

T1	T2	T3	T4	T5
iT1Z1	iT2Z1	iT3Z1 (bottom half)		
	iT2Z2	iT3Z2	iT4Z2	iT5Z2
	iT2Z3	iT3Z3 (top half)	iT4Z3	

Table 7.2: The ten best performing detectors selected for the high mass WIMP search analysis.

In order to select a sample of good events for the analysis, several event selection criteria (cuts) were applied to the data. Since the SuperCDMS Soudan data types included WIMP search, ^{252}Cf calibration and ^{133}Ba calibration, a common cut set was selected for all data types to avoid systematic errors. A brief introduction of this cut set is summarized in the following list (see Appendix B for a more detailed cut list and Table 3.3 for quantity definitions).

- Data quality cut: to select good quality events.
  - `cPreSelection`: It consists of a large number of data quality cuts.

Detector	Special Notes
iT2Z3	Some phonon issues on channels B and D, top face
iT3Z1	Side 1 data excluded due to the ^{210}Pb source plate
iT3Z3	Side 2 data excluded due to the ^{210}Pb source plate
iT5Z2	CDMSlite operating mode takes a significant amount of livetime

Table 7.3: Special notes for some good detectors being selected in the high mass WIMP search analysis.

- Charge radial fiducial volume selection cuts: a combination of charge cuts to select events within a charge radial fiducial volume and remove the low yield high-radius events.
  - `cQin1_blind_v53`
  - `cQin2_blind_v53`
  - -0.2 < `qrpart1OF` < 0.5
  - -0.2 < `qrpart2OF` < 0.5
- Charge depth fiducial volume selection cuts: a combination of charge energy symmetry cuts to select events within a charge depth fiducial volume and remove the low yield surface events.
  - `cQsym_blind_v53`
  - -0.3 < `qzpartOF` < 0.3
- Single-scatter event selection cut: select events that have energy deposition in only one detector since a WIMP only interacts once in the detector.
  - ∼`cPmultTight_blind_v53`
- Non-source side cuts: select events on the non-source side of two detectors to avoid the large amount of low yield surface events from the ^{210}Pb source plates installed.
  - `pzpartOF` <0 for iT3Z1 and `pzpartOF` >0 for iT3Z3

In order to search for WIMPs, a two-dimensional parameter space constructed from phonon recoil energy (`precoiltNF`) and ionization yield (`ytNF`) were selected to model WIMP signals and background sources. In the phonon recoil energy dimension, WIMPs with different masses have different spectra, which provides us a possibility to model them individually. An energy range between 20 keV and 150 keV was selected for this analysis. In the ionization yield dimension, the ionization yield of a nuclear recoil event was about one third of that of a bulk electron recoil with the same total energy deposition according to Lindhard theory [44]. Since the yield of bulk electron recoils were calibrated to be 1, a yield range between 0.05 and 1.2 were selected for this analysis. Phonon recoil energy and ionization yield were assumed to be uncorrelated within this two-dimensional interested range.

7.2. Background Modeling

In this analysis we considered three background sources, which were neutrons, gammas and surface events. They have different distributions in the phonon recoil energy and the ionization yield dimensions. Thus, different data types were selected to model them individually. In order to generate probability density functions (PDFs) of these background models for the likelihood function, Gaussian fit (see Appendix C.1) and kernel density estimation (KDE) method [67] were first used to achieve 1-D continuous background event distributions in both dimensions separately. Then the 1-D PDF in the phonon recoil energy dimension was generated by normalizing the distribution function between 20 keV and 150 keV and 1-D PDF in the ionization yield dimension was generated by normalizing the distribution function between 0.05 and 1.2. The probability outside the interested range was set to zero in both dimensions.

a) Neutron Background Modeling

The neutron background model was constructed using the ^{252}Cf calibration data. ^{252}Cf was a neutron source, which could provide a sample of neutron-induced nuclear recoil events in the detectors. In the yield dimension, the neutron-induced nuclear recoil events in the

range of `precoiltNF` $\in$ [20, 150] keV distributed symmetrically around $\sim$0.3, which appeared to be a Gaussian. A fitting range of `ytNF` $\in$ [0.15, 0.45] was selected to enclose the center region of these nuclear recoil events and a Gaussian was performed. The result Gaussian would then be normalized to a PDF that was the neutron background model in the yield dimension. In the phonon recoil energy dimension, a nuclear recoil band cut (`cNR_ytNF_3sigma_v53_HT`, see Appendix B) was used to select the the neutron-induced nuclear recoil events. A KDE was calculated to generate a continuous distribution in the range of `precoiltNF` $\in$ [10, 160] keV, which was intentionally selected to avoid the potential inconsistent feature of the KDE at the energy boundaries. Once the 1-D yield and phonon recoil energy distributions were derived, they were normalized to 1-D PDFs within the interested ranges separately, which were used to model neutron background in these two dimensions (see Fig. 7.1 and 7.2).

b) Gamma Background Modeling

The gamma background model was constructed using both the ^{133}Ba calibration data and blinded WIMP search data. ^{133}Ba was a gamma source, which could provide a sample of electron recoil events in the range of `precoiltNF` $\in$ [20, 150] keV in the detectors. Since it could produce both bulk and surface electron recoil events, it was only used to generate the gamma background model in the yield dimension. In the range of `ytNF` $\in$ [0, 1.4], a KDE was calculated to achieve a continuous yield distribution for the gammas. In phonon recoil energy distribution blinded WIMP search data was used to generate the gamma background model. A yield selection cut `ytNF` $\in$ [0.85, 1.2] was applied in order to select a clean bulk electron recoil event sample. A continuous phonon recoil energy distribution was generated from the calculation of a KDE in the range of `precoiltNF` $\in$ [10, 160] keV. Once the 1-D yield and phonon recoil energy distributions were derived, they were normalized to 1-D PDFs within the interested ranges separately, which were used to model gamma background in these two dimensions (see Fig. 7.3 and 7.4).

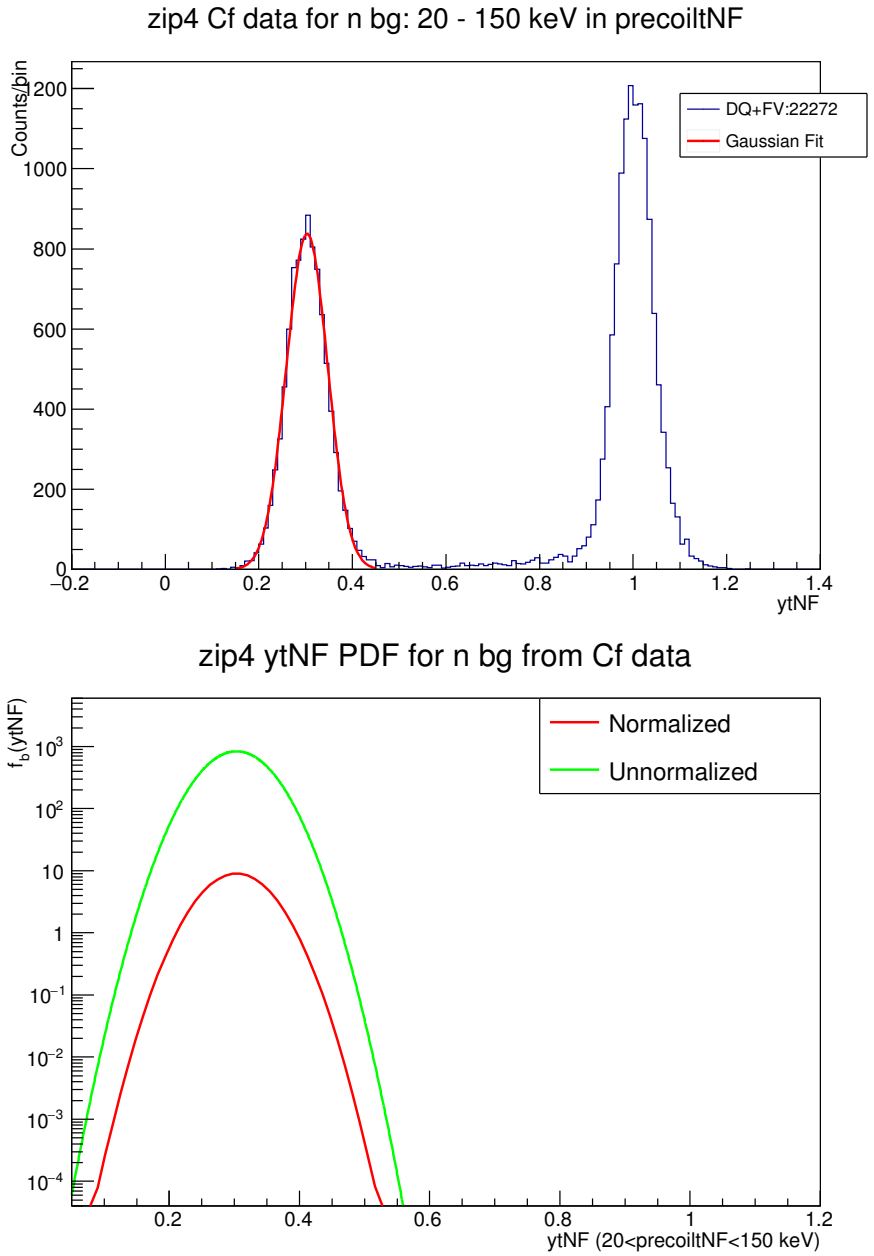

Figure 7.1: The top plot shows a Gaussian is fit from the NR sample in the yield (`ytNF`) dimension in iT2Z1 using the ^{252}Cf calibration data. The bottom plot shows that a PDF is calculated from the above fit.

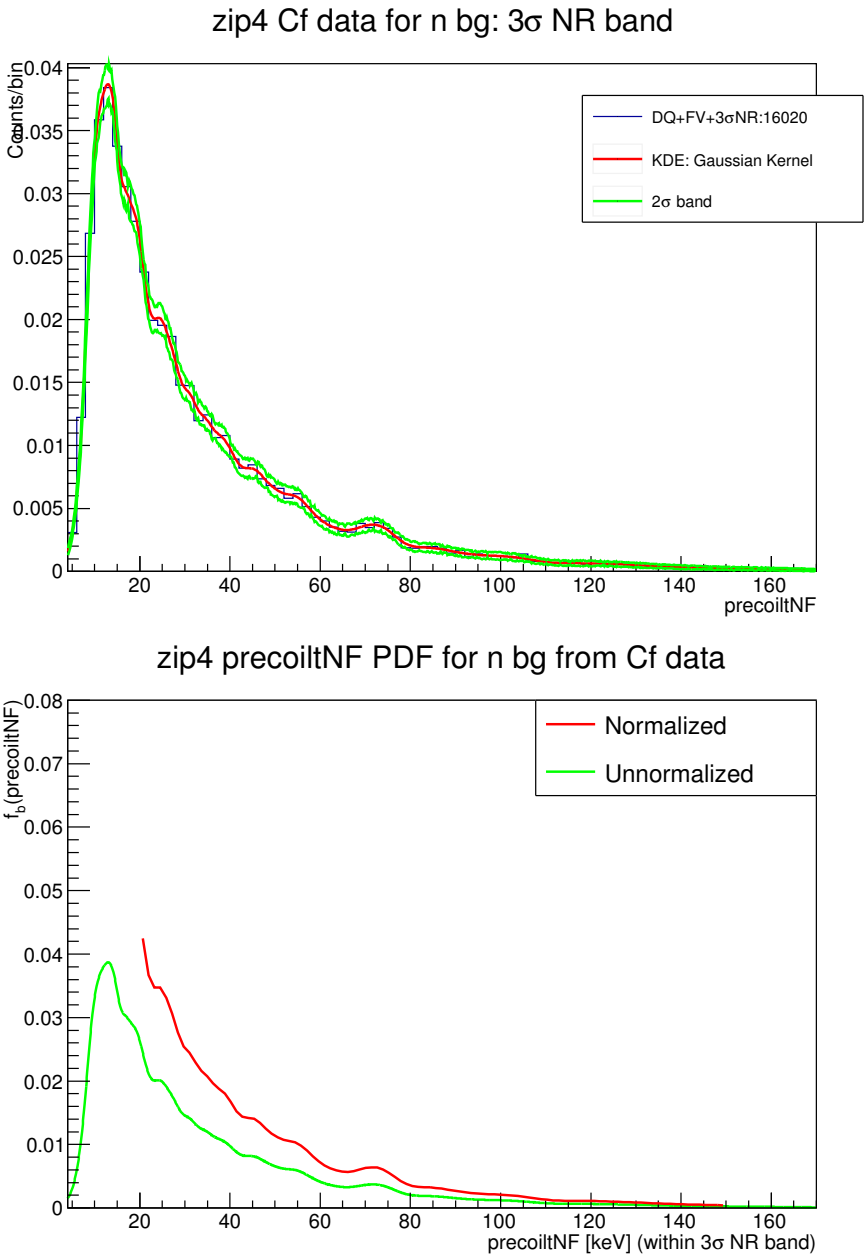

Figure 7.2: The top plot shows a KDE is calculated from the NR sample in the phonon recoil energy (`precoiltNF`) dimension in iT2Z1 using the ^{252}Cf calibration data. The bottom plot shows that a PDF is calculated from the above KDE.

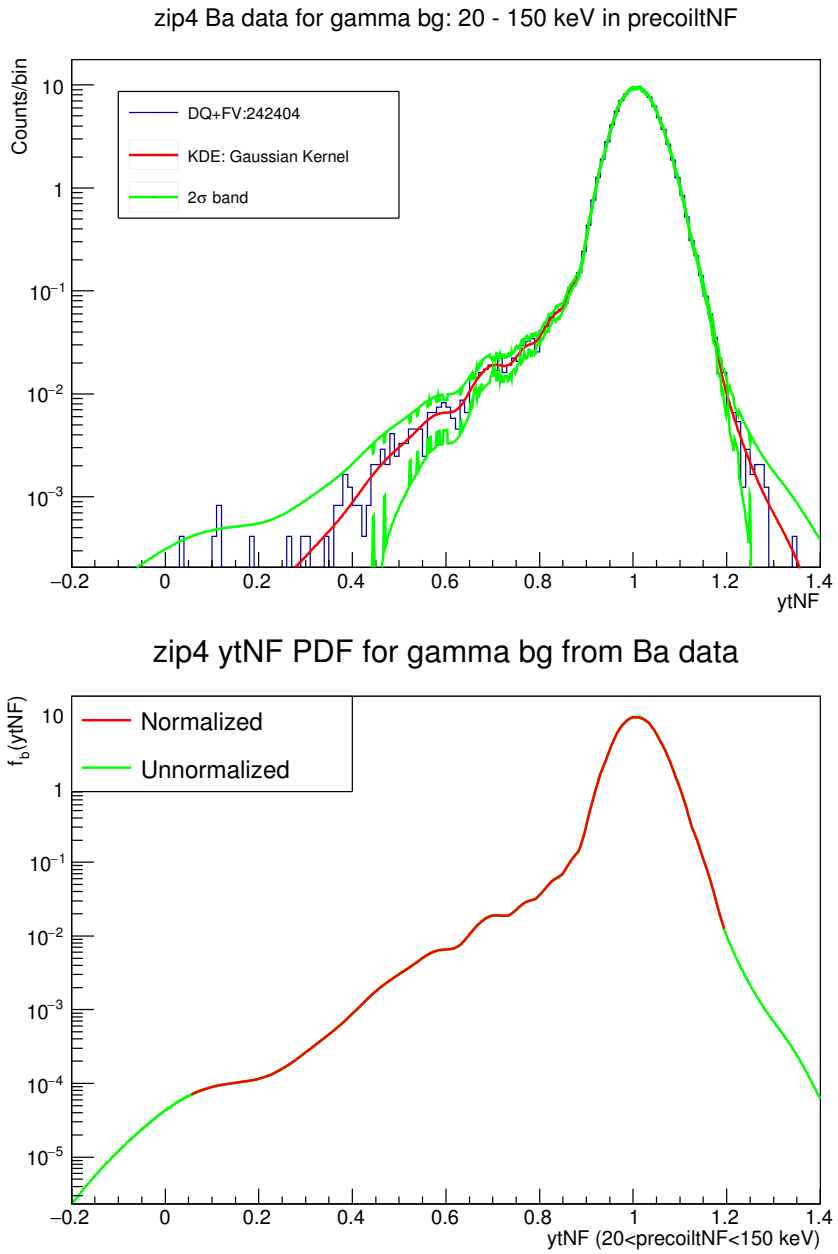

Figure 7.3: The top plot shows a KDE is calculated to from the bulk ER sample in the yield (`ytNF`) dimension in iT2Z1 using the ^{133}Ba calibration data. The bottom plot shows that a PDF is calculated from the above KDE.

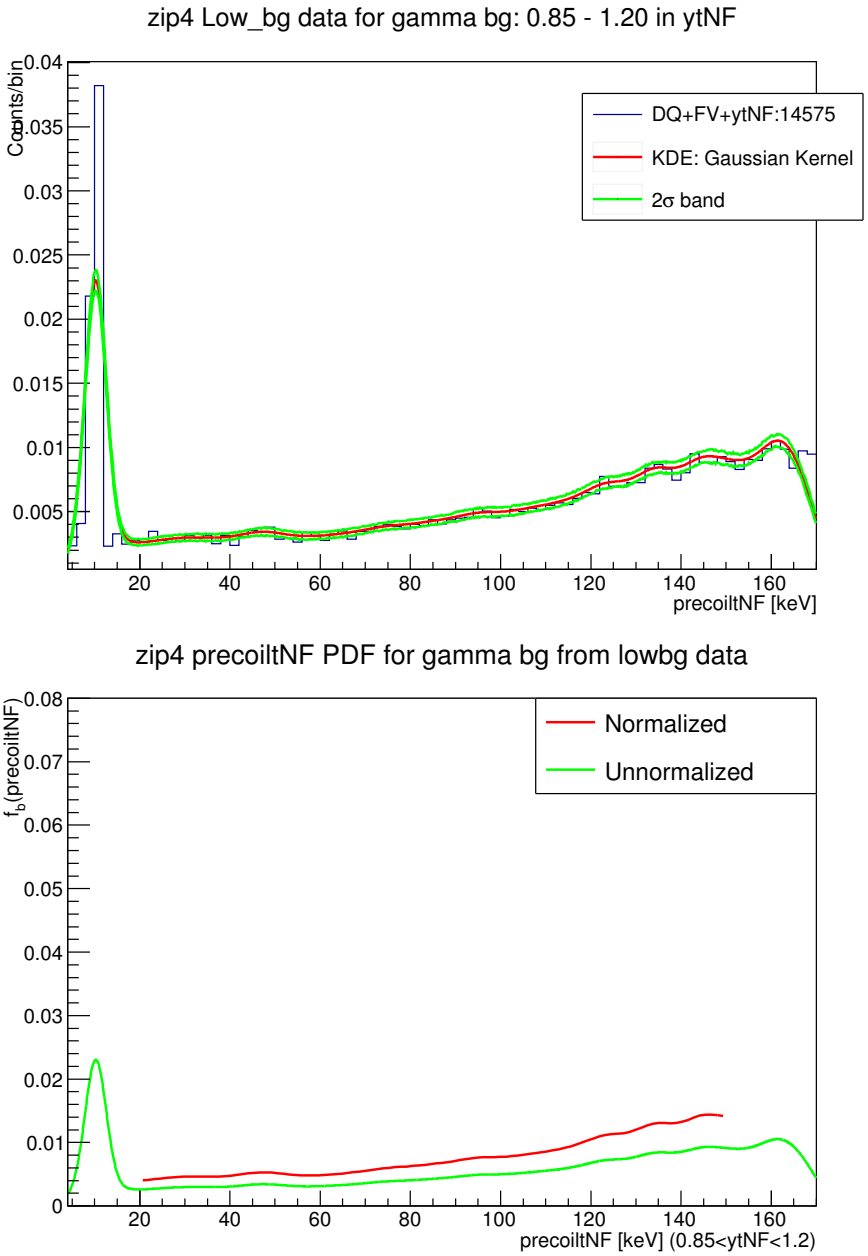

Figure 7.4: The top plot shows that a KDE is calculated from the bulk ER sample in the phonon recoil energy (`precoiltNF`) dimension in iT2Z1 using the blinded WIMP search data. The bottom plot shows that a PDF is calculated from the above KDE.

c) Surface Background Modeling

The surface background model was constructed using a surface event data set that was generated from the open WIMP search data [68]. The two source detectors, which had a large number of surface event sample, were used to map to the other detectors and generate weighted surface events in them. Since one ^{210}Pb source plate was above the side 1 of iT3Z1, the surface events on this side of iT3Z1 were used to map to the top sides of all other detectors. Similarly, the surface events on the bottom sides of all other detectors were mapped from those on the side 2 of iT3Z3.

In the yield dimension, a KDE was calculated for the surface events with `precoiltNF` $\in$ [20, 150] keV in a yield range of `ytNF` $\in$ [0, 1.4] to achieve a continuous distribution. In the phonon recoil energy dimension, another KDE was calculated for the surface events with `ytNF` $\in$ [0.05, 1.2] in `precoiltNF` $\in$ [10, 160] keV. Then they were normalized to 1-D PDFs within the interested ranges separately, which were used to model surface background in these two dimensions (see Fig. 7.5 and 7.6).

7.3. WIMP Signal Modeling

For the WIMP signal model, we also needed 1-D PDFs in both yield and phonon recoil energy dimensions. Since the yield distribution of the neutron-induced nuclear recoil events was indistinguishable from that of the WIMP-induced nuclear recoil events, the 1-D PDF of neutron background model in the yield dimension was used as WIMP signal model in the yield dimension. In the recoil energy dimension the 1-D PDF was derived from the WIMP spectrum corrected by a signal efficiency.

In order to derive the WIMP spectrum, a calculation proposed by Lewin and Smith [42] was used. Among a number of parameters that go into the WIMP spectrum calculation, the spin-independent WIMP-nucleon cross section, σ_{SI}, and the WIMP mass, M_{WIMP}, were the two of most interest to us. Since σ_{SI} was linear in the differential WIMP event rate

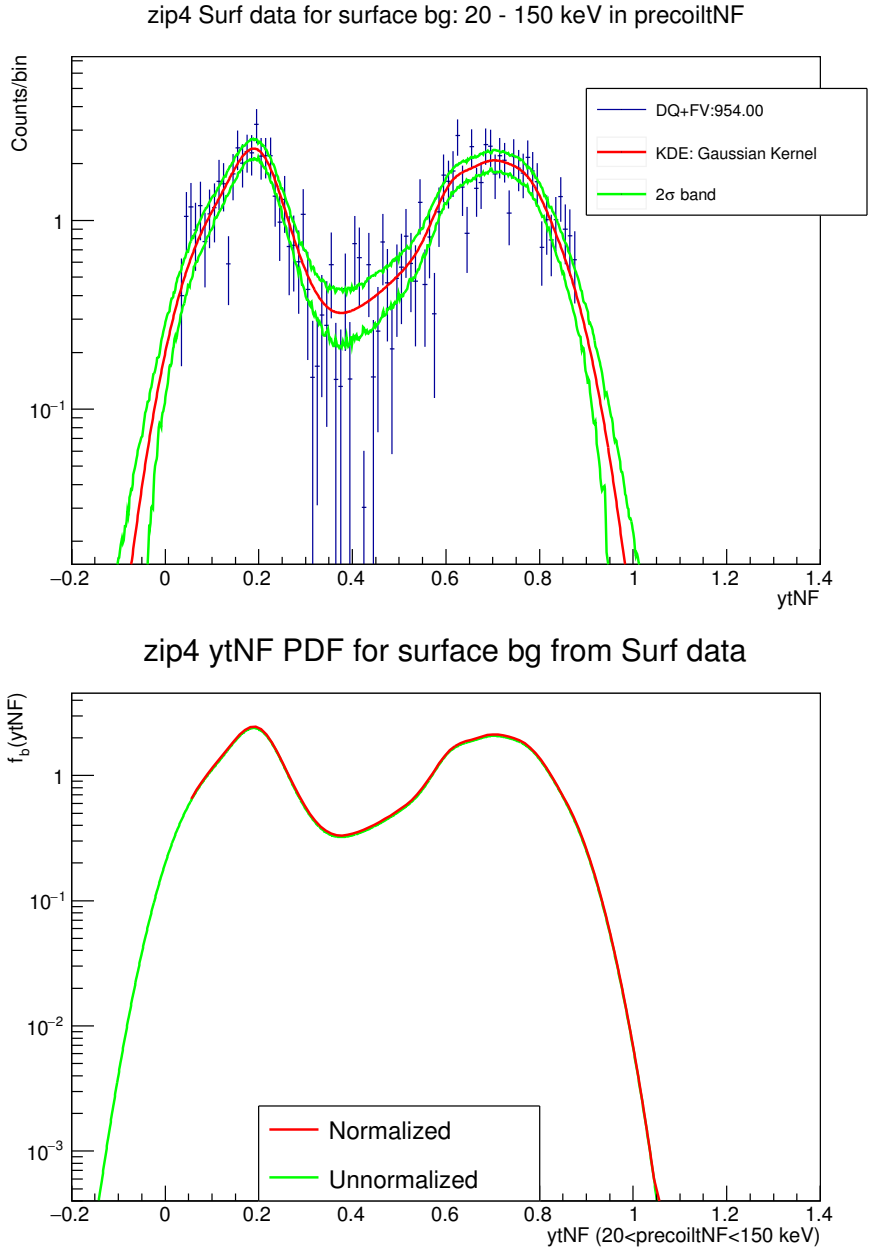

Figure 7.5: The top plot shows a KDE is calculated from the surface event sample in the yield (`ytNF`) dimension in iT2Z1 using the surface event data set. The bottom plot shows that a PDF is calculated from the above KDE.

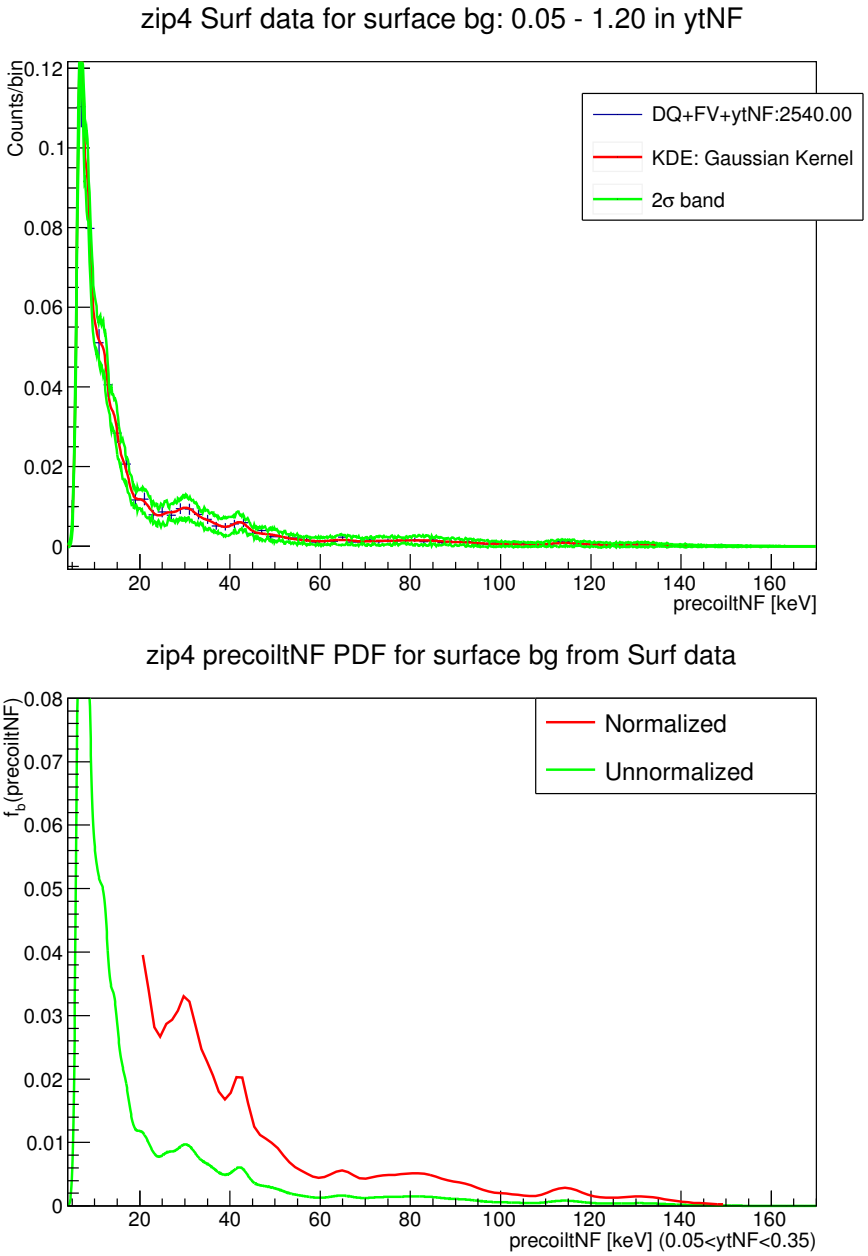

Figure 7.6: The top plot shows a KDE is calculated from the surface event sample in the phonon recoil energy (`precoiltNF`) dimension in iT2Z1 using the surface event data set. The bottom plot shows that a PDF is calculated from the above KDE.

calculation, a σ_{SI} value of 10^{-45} cm^2 was selected for the generation of WIMP signal model in this analysis. The WIMP spectra with other σ_{SI} values could be derived from this by a simple linear scaling.

For a Ge target, whose atomic number is ~76, and a spin-independent WIMP-Ge cross section σ_{SI}=10^{-45} cm^2, WIMP spectra in the iZIP detector were calculated. Figure 7.7 illustrates the differential WIMP event rate in Ge for ten different WIMP masses. In this analysis, WIMP signal models of nine WIMP masses were built and studied, which were 25, 50, 75, 100, 125, 150, 250, 500 and 750 GeV/c^2.

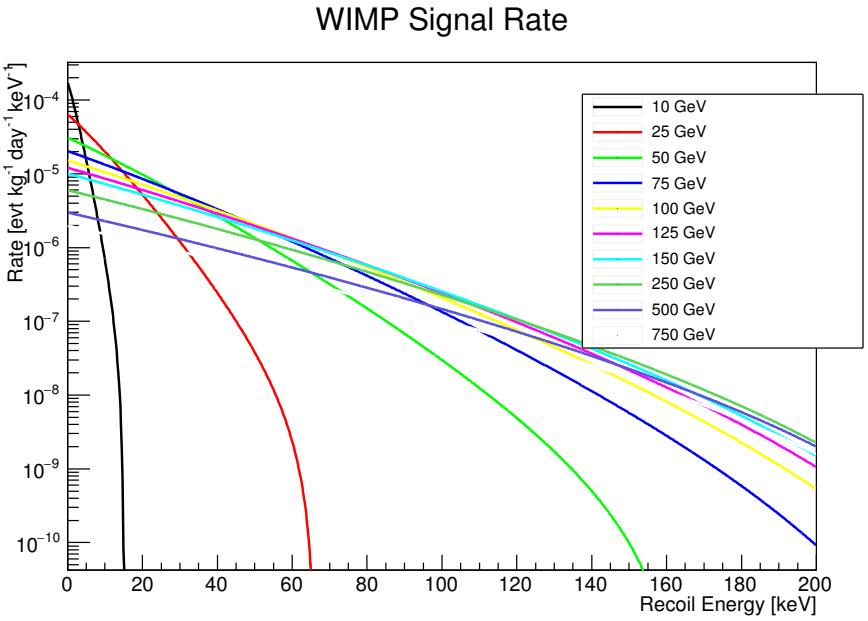

Figure 7.7: Calculated WIMP spectra in Ge target for different WIMP masses [42] with an assumption that the spin-independent WIMP-nucleon cross section is 10^{-45} cm^2.

In order to avoid systematic effect among different background models, a common set of event selection cuts was applied to different data sets when deriving these three background models. Thus, an efficiency on the WIMP signal needed to be accounted for due to the application of this cut set. In addition to the data quality, fiducial volume and single-scatter selection cuts listed in Section 7.1, the selection of interested yield range `ytNF` $\in$ [0.05,

1.2] and the trigger efficiency were also considered in the signal efficiency calculation. By combining all these efficiencies together, an energy-dependent signal efficiency for each iZIP detector was derived (see Fig. 7.8). Integrating this signal efficiency with a WIMP spectrum for a given WIMP mass from the theoretical calculation, a WIMP spectrum within the same parameter space as the background models in a iZIP detector was calculated (see Fig. 7.9). Thus, by normalizing the efficiency-corrected WIMP spectrum between 20 and 150 keV recoil energy, the WIMP signal model for a given WIMP mass was generated (see Fig. 7.10). The probability of the WIMP signal outside the interest range is set to zero in both yield and recoil energy dimensions.

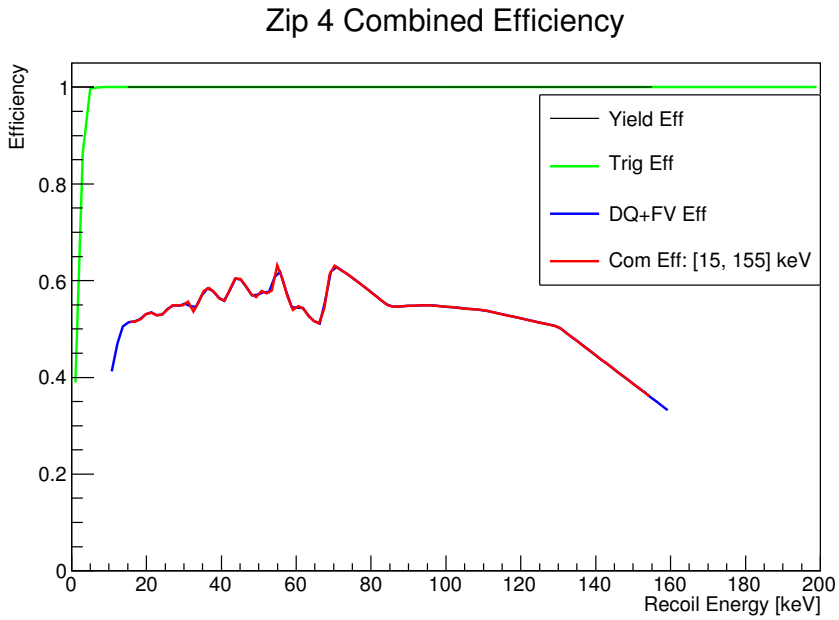

Figure 7.8: Combined cut efficiency (red) for the WIMP signal within 15 and 155 keV phonon recoil energy in iT2Z1.

7.4. Likelihood Ratio

According to the Neyman-Pearson lemma [69], if a test statistic is constructed in the form of likelihood ratio, then this likelihood ratio test is the most powerful test when rejecting H_0 and accepting H_1 at a significance level α. This applies to both simple hypotheses and composite hypotheses. Take a distribution function $f(x_1, x_2, ..., x_n; \theta_1, \theta_2, ..., \theta_m)$ as an ex-

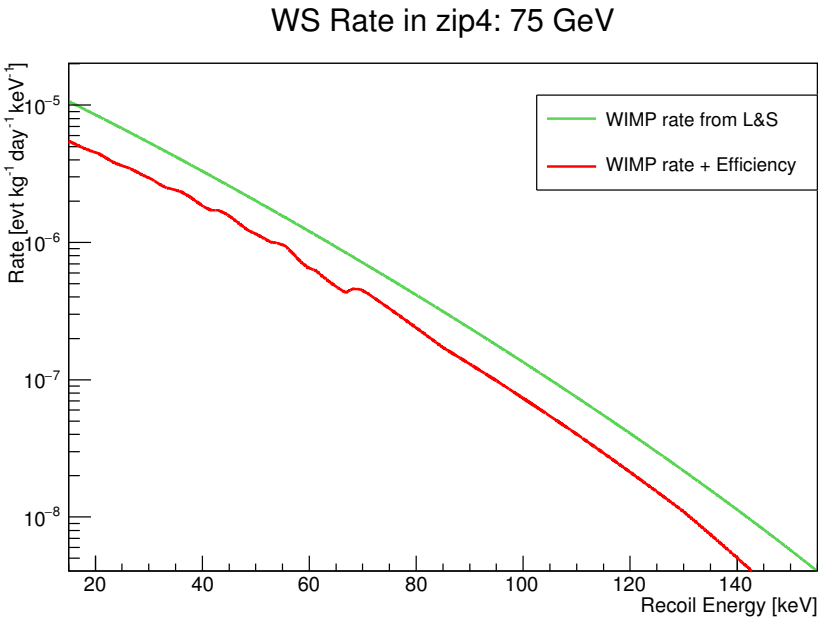

Figure 7.9: This plot shows the comparison between the WIMP spectrum for a 75 GeV WIMP in iT2Z1 after taking the efficiency into account (red) and the WIMP spectrum from theoretical calculation (green) .

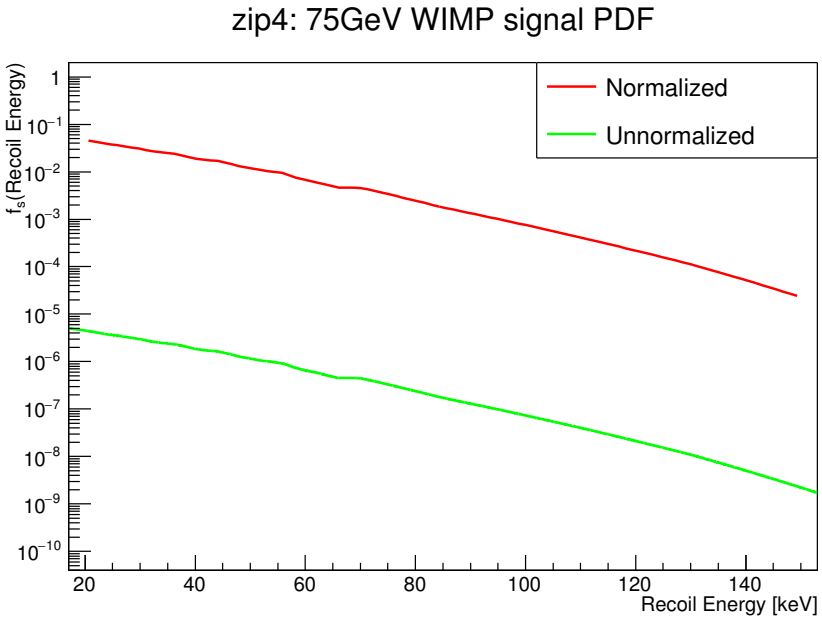

Figure 7.10: This plot shows the generation of WIMP signal PDF (red) from the efficiency-corrected WIMP spectrum in iT2Z1 for a 75 GeV WIMP between 20 and 150 keV phonon recoil energy with the assumption of σ_{SI}=10^{-45} cm^2.

ample, if in a hypothesis where the θ's have specified values, then this test is called a simple hypothesis. If the θ's have a set of values, then this test is called a composite hypothesis.

Composite hypothesis is more general and complicated. Assuming the parameter θ is in the parameter space of a set Ω and Ω_0 is a subset of Ω, a hypothesis test could be stated as

- H_0: $\theta \in \Omega_0$
- H_1: $\theta \in \Omega$

With the likelihood function $L(\theta; x) = f(x; \theta) = f(x_1, x_2, ..., x_n; \theta_1, \theta_2, ..., \theta_m)$, a likelihood ratio test statistic could be constructed as

$$\lambda(x) = \frac{sup\{L(\theta; x), \theta \in \Omega_0\}}{sup\{L(\theta; x), \theta \in \Omega\}} \tag{7.1}$$

where `sup` indicates the maximum value of $L(\theta; x)$ in Ω or Ω_0 if they do have one.

After Neyman and Pearson suggested this likelihood ratio method for composite hypotheses by applying the principle of maximum likelihood, Wilks went one step further to suggest that if one constructed a test statistic in the form of

$$\begin{aligned} q_{stat} &= -2\, Ln(\lambda(x)) \\ &= -2\, Ln \frac{sup\{L(\theta; x), \theta \in \Omega_0\}}{sup\{L(\theta; x), \theta \in \Omega\}} \end{aligned} \tag{7.2}$$

If the parameter θ has n degrees of freedom in Ω and m in Ω_0, then q_{stat} approximates a χ^2 distribution with $n - m$ degrees of freedom at a large sample size [70].

$$q_{stat} = -2\, Ln(\lambda(x)) \approx \chi^2_{n-m} \tag{7.3}$$

7.5. Analysis

Since the ten best performing iZIP detectors were used in this high mass WIMP search analysis, they were combined in the likelihood function $L(N_s(\sigma_{SI}), N_b)$, which was constructed in the following way

$$L(N_s(\sigma_{SI}), N_b) = \prod_{det=1}^{10} [Poisson(N_d; N_{s,d} + N_{b,d}) \times \prod_{i=1}^{N_d} \frac{N_{s,d} f_{s,d} + N_{b,d} f_{b,d}}{N_{s,d} + N_{b,d}} \times Gauss(\mu_{n,d}, \sigma_{n,d})] \tag{7.4}$$

where

- the indices s,b,d represent signal, background, detector respectively.
- N_s is the total number of signal events, which is the parameter of primary interest. It is the sum of the expected signal number, $N_{s,d}$, in each detector. $N_{s,d}$ differs from detector-to-detector because of detector-dependent efficiency and exposure.
- $N_{b,d}$ is the total number of background events N_b in detector d, which equals to $N_{n,d} + N_{g,d} + N_{sf,d}$ with n, g, sf stand for neutrons, gammas and surface events. There are 30 background nuisance parameters in total.
- N_d is the number of events that pass the selection cuts in detector d.
- Poisson(N_d; $N_{s,d}$ + $N_{b,d}$)= $\frac{(N_{s,d}+N_{b,d})^{N_d}}{N_d!} e^{-(N_{s,d}+N_{b,d})}$ is the constraint on the observed event N_d in each detector.
- $f_{s,d}$ is the 2-D PDF of the WIMP signal model, which equals to $f_{s,d,p} \cdot f_{s,d,y}$ assuming the recoil energy and yield dimensions are independent. The indices p, y stand for `precoiltNF`, `ytNF` respectively.
- $f_{b,d}$ is the 2-D PDF of background models, where the background source b can be n,g,sf. It equals to $f_{b,d,p} \cdot f_{b,d,y}$ with p, y stand for `precoiltNF`, `ytNF` respectively.
- Gauss($\mu_{n,d}$, $\sigma_{n,d}$) is the constraint on the number of expected neutron events.

From this likelihood function, a test statistic $q(N_s(\sigma_{SI}))$ for this analysis was constructed in the form of

$$q(N_s(\sigma_{SI})) = -2ln\frac{L(N_s; \sum_b \sum_{d=1}^{10} \hat{\hat{N}}_{b,d})}{L(\hat{N}_s, \sum_b \sum_{det=1}^{10} \hat{N}_{b,d})} \tag{7.5}$$

where $\hat{\hat{N}}_{b,d}$ (b = n, g, sf; d= 1,...,10) is the conditional optimal value for each background in each detector when the total signal number N_s is fixed, and $\hat{N}_{b,d}$ (b = n, g, sf; d= 1,...,10) is the unconditional optimal value when every parameter is not constrained.

In order to search for the optimal values for all the parameters, the likelihood function was expanded, simplified, and then converted to a log-likelihood form. Since the test statistic consists of two independent log-likelihood function terms, the maximization of each of them were performed separately. The extended likelihood function was in the form of

$$\begin{aligned}
&L(N_s(\sigma_{SI}),N_b) \\
&\quad = \prod_{det=1}^{10} [Poisson(N_d; N_{s,d} + N_{b,d}) \times \prod_{i=1}^{N_d} \frac{N_{s,d}f_{s,d} + N_{b,d}f_{b,d}}{N_{s,d} + N_{b,d}} \times Gauss(\mu_{n,d}, \sigma_{n,d})] \\
&\quad = \prod_{det=1}^{10} [\frac{(N_{s,d} + N_{b,d})^{N_d}}{N_d!} e^{-(N_{s,d}+N_{b,d})} \times \prod_{i=1}^{N_d} \frac{N_{s,d}f_{s,d} + N_{b,d}f_{b,d}}{N_{s,d} + N_{b,d}} \\
&\qquad \times \frac{1}{\sqrt{2\pi}\sigma_{n,d}} exp(-\frac{(N_{n,d} - \mu_{n,d})^2}{2\sigma_{n,d}^2})] \\
&\quad = \prod_{det=1}^{10} [\frac{e^{-(N_{s,d}+N_{b,d})}}{N_d!} \times \prod_{i=1}^{N_d} (N_{s,d}f_{s,d} + N_{b,d}f_{b,d}) \\
&\qquad \times \frac{1}{\sqrt{2\pi}\sigma_{n,d}} exp(-\frac{(N_{n,d} - \mu_{n,d})^2}{2\sigma_{n,d}^2})]
\end{aligned} \tag{7.6}$$

From this, the form of the log-likelihood function was derived as

$$
\begin{aligned}
&ln(L(N_s(\sigma_{SI}), N_b)) \\
&= \sum_{det=1}^{10} [-(N_{s,d} + N_{b,d}) - ln(N_d!) + \sum_{i=1}^{N_d} ln(N_{s,d} f_{s,d} + N_{b,d} f_{b,d}) \\
&\quad + (-\frac{(N_{n,d} - \mu_{n,d})^2}{2\sigma_{n,d}^2} - ln(\sqrt{2\pi}\sigma_{n,d}))] \\
&= - N_s(\sigma_{SI}) - \sum_{det=1}^{10} (N_{n,d} + N_{g,d} + N_{sf,d}) \\
&\quad + \sum_{det=1}^{10} \sum_{i=1}^{N_d} ln(N_{s,d} f_{s,d,p} f_{s,d,y} + N_{n,d,p} f_{n,d,p} f_{n,d,y} + N_{g,d,p} f_{g,d,p} f_{g,d,y} + N_{sf,d,p} f_{sf,d,p} f_{sf,d,y}) \\
&\quad - \sum_{det=1}^{10} \frac{(N_{n,d} - \mu_{n,d})^2}{2\sigma_{n,d}^2} + \text{constant}
\end{aligned}
\tag{7.7}
$$

Thus, the test statistic $q(N_s(\sigma_{SI}))$ could be expressed in two terms as

$$
\begin{aligned}
q(N_s(\sigma_{SI})) &= -2ln \frac{L(N_s; \sum_b \sum_{d=1}^{10} \hat{\hat{N}}_{b,d})}{L(\hat{N}_s, \sum_b \sum_{det=1}^{10} \hat{N}_{b,d})} \\
&= [-2ln(L(N_s; \sum_b \sum_{d=1}^{10} \hat{\hat{N}}_{b,d}))] - [-2ln(L(\hat{N}_s, \sum_b \sum_{det=1}^{10} \hat{N}_{b,d}))]
\end{aligned}
\tag{7.8}
$$

where the conditional log-likelihood function term was in the form of

$$
\begin{aligned}
&-2ln(L(N_s; \sum_b \sum_{d=1}^{10} \hat{\hat{N}}_{b,d})) \\
&= -2[-N_s(\sigma_{SI}) - \sum_{det=1}^{10} (\hat{\hat{N}}_{n,d} + \hat{\hat{N}}_{g,d} + \hat{\hat{N}}_{n,d}) \\
&\quad + \sum_{det=1}^{10} \sum_{i=1}^{N_d} ln(N_{s,d} f_{s,d,p} f_{s,d,y} + \hat{\hat{N}}_{n,d,p} f_{n,d,p} f_{n,d,y} + \hat{\hat{N}}_{g,d,p} f_{g,d,p} f_{g,d,y} + \hat{\hat{N}}_{sf,d,p} f_{sf,d,p} f_{sf,d,y}) \\
&\quad - \sum_{det=1}^{10} \frac{(\hat{\hat{N}}_{n,d} - \mu_{n,d})^2}{2\sigma_{n,d}^2} + \text{constant}]
\end{aligned}
\tag{7.9}
$$

and the unconditional log-likelihood function term was in the form of

$$
\begin{aligned}
&-2ln(L(\hat{N}_s, \sum_{b}\sum_{det=1}^{10}\hat{N}_{b,d})) \\
&= -2[-\hat{N}_s(\sigma_{SI}) - \sum_{det=1}^{10}(\hat{N}_{n,d} + \hat{N}_{g,d} + \hat{N}_{sf,d}) \\
&\quad + \sum_{det=1}^{10}\sum_{i=1}^{N_d} ln(\hat{N}_{s,d}f_{s,d,p}f_{s,d,y} + \hat{N}_{n,d,p}f_{n,d,p}f_{n,d,y} + \hat{N}_{g,d,p}f_{g,d,p}f_{g,d,y} + \hat{N}_{sf,d,p}f_{sf,d,p}f_{sf,d,y}) \\
&\quad - \sum_{det=1}^{10}\frac{(\hat{N}_{n,d} - \mu_{n,d})^2}{2\sigma_{n,d}^2} + \text{constant}]
\end{aligned}
\tag{7.10}
$$

Notice that the two constant terms cancelled out when these two log-likelihood function terms added up together. Since the background parameters, $N_{b,d}$, were nuisance parameters and the signal event number, N_s, in the conditional log-likelihood function was the only parameter that could be given a preset value, according to the Wilks′ theorem, the test statistic $q(N_s(\sigma_{SI}))$ approximates χ_1^2 distribution at a large sample size.

With the signal and background models available, the expected signal number in each detector, $N_{s,d}$, was the only parameter that needed to be determined beforehand, which would sum up to get the total expected signal number N_s. Since the differential signal event rate was the same in each iZIP detector for a given WIMP, the expected signal number in each detector, $N_{s,d}$, was linked to each other through the spin-independent WIMP-Ge cross section, σ_{SI}. Since σ_{SI}=10^{-45} cm^2 was selected in this analysis, $N_{s,d}$ could be calculated using the signal efficiency-corrected signal rate between 20 keV and 150 keV recoil energy and the exposure. The exposure of each detector were calculated from its target mass and WIMP search livetime as shown in Table 7.4. Thus, the expected WIMP number, $N_{s,d}$, in each detector was calculated (see Table 7.5).

In order to generate pseudo data sets that could represent the unblinded WIMP search data, the blinded WIMP search data (i.e. the bg-permitted data) was used a proxy for us

Detector	Mass (kg)	Livetime (day)	Raw Exposure (kg day)
iT1Z1	0.6095	285.73	174.152
iT2Z1	0.5974	317.29	189.549
iT2Z2	0.5913	322.37	190.617
iT2Z3	0.5791	313.15	181.345
iT3Z1	0.6034	206.01	124.306
iT3Z2	0.5913	307.77	181.984
iT3Z3	0.6095	210.58	128.349
iT4Z2	0.5974	322.84	192.865
iT4Z3	0.5943	347.52	206.531
iT5Z2	0.6065	144.83	87.8394

Table 7.4: Mass and livetime information of the ten best performing detectors in the high mass WIMP search analysis.

	25 GeV/c^2	**75 GeV/c^2**	**250 GeV/c^2**
iT1Z1	0.00319683	0.0158515	0.00914458
iT2Z1	0.00360323	0.0184497	0.0107192
iT2Z2	0.0031119	0.0160296	0.0093617
iT2Z3	0.00321227	0.0162816	0.00941594
iT3Z1	0.00105217	0.00517096	0.00298276
iT3Z2	0.00299828	0.0153303	0.00885563
iT3Z3	0.000804943	0.00436748	0.00256811
iT4Z2	0.00314924	0.016161	0.00940785
iT4Z3	0.00355983	0.0179366	0.010357
iT5Z2	0.00151446	0.00678244	0.00364566
Total	**0.0262031**	**0.132361**	**0.0764585**

Table 7.5: Expected WIMP number in each detector between 20 and 150 keV recoil energy after efficiency correction in each detector for three studied WIMP masses with the assumption of σ_{SI}=10^{-45} cm^2.

to get an idea of what the unblinded data should look like. Since there was a ROOT minimizer package 'Minuit' [71] available, we switched the maximization of the unconditional log-likelihood function to the minimization of it by multiplying it with -1, which was then in the form of $-2Ln(L(\hat{N}_s, \sum_b \sum_{det=1}^{10} \hat{N}_{b,d}))$. An algorithm 'Migrad' was selected to perform the minimization and search for the optimal value of each background component, $\hat{N}_{b,d}$.

Since $\hat{N}_{b,d}$ was fit from the blinded data, it was biased due to existence of the blinding region. Thus, some correction was needed to account for the events in the blinding region. The gamma background had a high yield which made it contribute less in the blinding region so its optimal numbers $N_{g,d}$, which was different in each detector, could be used directly in the generation of pseudo data sets. The neutron and surface background sources were both needed to account for the blinding region. The estimated neutron numbers from the SuperCDMS Soudan data [72] were used as the expected neutron numbers $N_{n,d}$. The surface events, $N_{sf,d}$, were accounted for using a scaling factor calculated from the high yield region, which made it unaffected by the blinding. After the blinding region was accounted for, the mean value of each background component in each detector, $\hat{N}_{b,d}$, was shown in Table 7.6.

In order to determine how many events to be generated for each pseudo experiment, the mean value of each background component in each detector was treated as the mean value of a Poisson distribution, then an integer random number was generated from it. In this way, the event number of each of these 30 backgrounds in a pseudo data set was calculated. For each background particle, its phonon recoil energy (`precoiltNF`) and ionization yield (`ytNF`) values were generated using random numbers sampled from the two 1-D PDFs in these two dimensions in each detector, which were within 20 and 150 keV for `precoiltNF` and within 0.05 and 1.2 for `ytNF`.

In order to check whether our models had the ability to quantify a signal if there was an excess, we performed a bias test on the input and measured signal event numbers. Pseudo

Detector	Neutrons	Gammas	Surface
iT1Z1	0.01172	6386	1.86176e-08
iT2Z1	0.011995	7222.68	0.942091
iT2Z2	0.010693	3931.01	3.92105e-08
iT2Z3	0.017685	17086.5	3.32758
iT3Z1	0.00327	1465.96	2.1551e-06
iT3Z2	0.01107	3893.08	6.63579
iT3Z3	0.00392	2117.75	71.232
iT4Z2	0.01313	3949.7	0.346243
iT4Z3	0.01928	16121.1	0.00942946
iT5Z2	0.0065	1659.77	2.27882

Table 7.6: The mean number of each background in each detector for pseudo data generation after compensating for the blinding region in the bg-permitted data.

data sets were generated by artificially inserting signal events into different detectors randomly according to their signal efficiencies and exposures. For each of the nine WIMP masses studied, a variation of signal events with numbers of 1 through 4 were tested, where this upper limit N_s=4 was derived from the CDMS II-Edelweiss limit [73]. 80 pseudo data sets were generated for each input signal number from each of the nine WIMP masses. In Fig. 7.11, the signal events that were estimated by the models (measured N_s) followed the change of the input signal event numbers (input N_s) approximately linearly. This result from the bias test indicated that when there was a WIMP signal excess in the detectors, our model had the ability to detect it.

7.6. Exclusion Limit

Before unblinding the high mass WIMP search data, the sensitivity of this analysis was estimated by pseudo experiments. 50 pseudo data sets were generated based on the mean

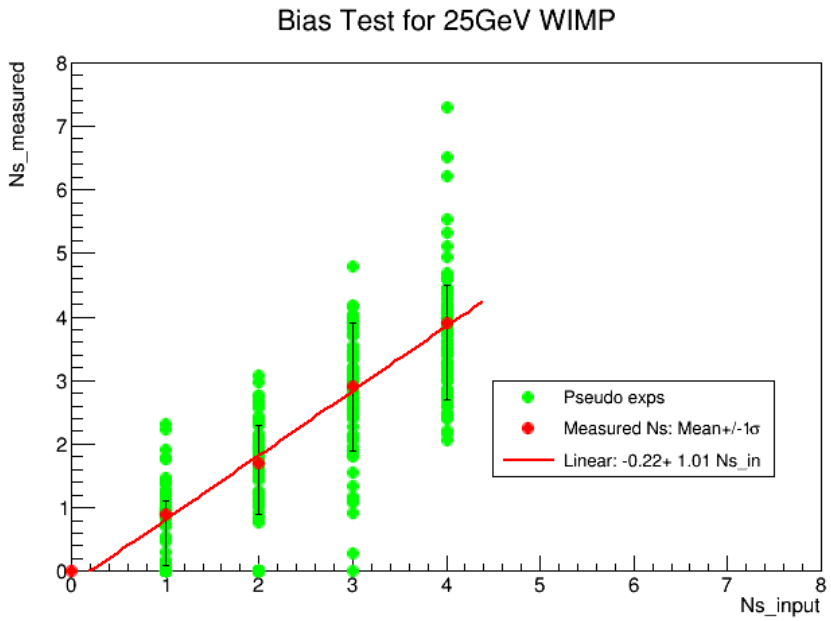

Figure 7.11: This plot shows a linear relation between the measured signal numbers (Ns_measured) and the input signal numbers (Ns_input) for a 25 GeV WIMP. For each input signal number, 80 pseudo data sets are generated to test the model.

values of background sources in Table 7.6. The value of the test statistic $q(N_s(\sigma_{SI}))$

$$q(N_s(\sigma_{SI})) = -2ln\frac{L(N_s; \sum_b \sum_{d=1}^{10} \hat{\hat{N}}_{b,d})}{L(\hat{N}_s, \sum_b \sum_{det=1}^{10} \hat{N}_{b,d})} \tag{7.11}$$

can be calculated when a signal event number N_s is preset.

Since $q(N_s(\sigma_{SI}))$ asymptotically approximates the distribution of χ_1^2 [74], an upper limit of N_s at a 90% confidence level gives a χ_1^2 value of 2.706. By varying the value of N_s in the nominator, an intersection point of $q(N_s(\sigma_{SI}))$ and 2.706 can be scanned as shown in Fig. 7.12. Since the expected WIMP number in the detectors are calculated with the assumption of σ_{SI}=10^{-45} cm^2, the ratio between this N_s upper limit and total expected WIMP number from a particular WIMP mass is the ratio of the σ_{SI} upper limit to the value of 10^{-45} cm^2. Based on the results of the likelihood ratio, a projected sensitivity of this high threshold analysis can be estimated.

After unblinding, the same procedure was run on the high mass WIMP search data. An exclusion limit is set for a WIMP-nucleon spin-independent cross section of 1.32 $\times 10^{-44}$ cm^2 with a WIMP mass of 75 GeV/c^2 at 90% confidence level by the profile likelihood ratio technique as shown in Fig. 7.13 .

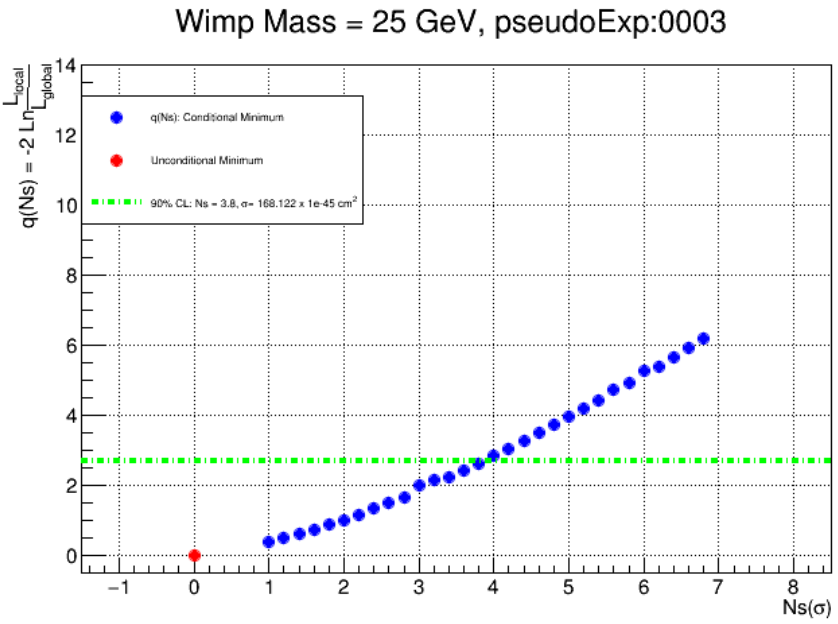

Figure 7.12: This plot shows the scan of a signal event number (Ns) upper limit in a pseudo experiment at a 90% confidence level for a 25 GeV WIMP with the assumption of σ_{SI}=10^{-45} cm^2.

There are a few aspects to be noted about the profile likelihood analysis presented in this thesis. The first is the correlation between the phonon recoil energy and yield spaces. The second is the shape uncertainty of the KDEs in the background models.

A 20 keV recoil energy threshold was chosen to avoid the correlation between energy and yield at low energy region, where we know that the ER and NR distributions would flare. The yield of bulk ERs are calibrated to be one so it is energy independent. However, in the energy range of [20, 150] keV, the NR yield distribution increases gradually as the energy increases. The neutron yield model was derived using the whole energy range of

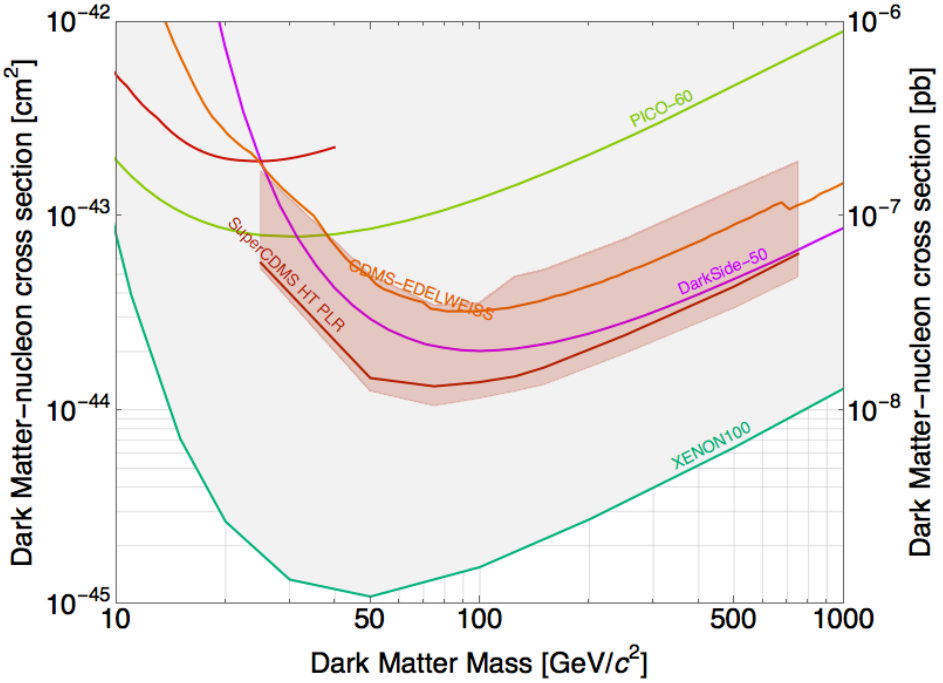

Figure 7.13: This plot shows the exclusion limit of this high mass WIMP search analysis from the profile likelihood ratio technique (dark red curve). A WIMP-nucleon spin-independent cross section of 1.32 $\times 10^{-44}$ cm^2 with a WIMP mass of 75 GeV/c^2 at 90% confidence level is reached. The shaded area between 25 and 750 GeV/c^2 WIMP masses is the sensitivity with 2σ uncertainties from the profile likelihood ratio technique. The exclusion limit is consistent with the sensitivity estimation before unblinding. The curve in orange is the CDMS-Edelweiss combined limit. The short curve in dark red at the top left is the limit from SuperCDMS Soudan Low-mass WIMP search analysis. The curve in light green is the limit from PICO-60. The curve in magenta is the limit from DarkSide-50. The curve in green is the limit from XENON100.

interest, and the WIMP yield model was the same as the neutrons. Thus, both the signals and neutrons can be either overestimated or underestimated. This would have an effect on the final exclusion limit. However, a study on the estimated neutron numbers gave a total of 0.1 neutrons in the entire WIMP search data, which restricts this correlation effect on the limit to a small amount.

This exclusion limit curve has not had the KDE shape uncertainty propagated into it yet. A description of the KDE shape uncertainty needs to be incorporated into the analysis. The uncertainties at each point are independent. Thus, the shape uncertainty cannot be described by one Gaussian constraint in the likelihood function.

One possible method is to do this in a binned way. For example, a KDE can be divided into ten bins in its range and the uncertainty in each bin is described using the uncertainty (σ) at its center value. The KDE in each bin would then be scaled up or down by f(y)+kσ, where k is the scaling factor in this bin. This factor k would be treated as a nuisance parameter in a Gaussian constraint on the KDE in this bin, which is in the form of Gauss(k|0,1). Since we have three backgrounds, ten detectors, two dimensions, and ten bins for each KDE, there would be an additional $3 \times 10 \times 2 \times 10 = 600$ nuisance parameters introduced into the current likelihood function, where it has already had 31 parameters. In addition, here I only assume a ten-bin division of the KDEs, and it has already given us 631 parameters in total. If we want more bins to better approximate the continuous case, there would be even more parameters in the likelihood function. This is quite unpractical when maximizing it.

However, in order to quantify how well the background models represent the data at the low statistic region, I did a check on the background numbers predicted by the models with the actual event numbers from direct counting in the low yield region. The results show that the predictions from the models match the actual event counts quite well within the Poisson error range except for detector iT3Z3. This indicates that the KDE shape uncertainty is

not that significant for nine of the ten detectors. The cause of the mismatch of the KDE prediction and the direct counting in iT3Z3 is still unknown, and further investigation is needed if this analysis is to be improved.

At this point I did not propagate any shape uncertainty of the background models into the final limit. If In the future there is a more practical way to incorporate the background model shape uncertainty, it is absolutely necessary to propagate it into the limit.

Chapter 8

Conclusion and Future

In this dissertation, I have described and discussed many selected studies that I have done on both SuperCDMS Soudan and SuperCDMS SNOLAB. Among them, the high mass WIMP search analysis using a profile likelihood ratio method and the simulation efforts on a potential active neutron veto system at SNOLAB are the two biggest and most futuristic projects. Although these works have reached some conclusions and come to a temporary stop point, there are still lots of space to move forward and improve.

8.1. Analysis with a Profile Likelihood Ratio Method

This is the first effort in the SuperCDMS collaboration to perform a WIMP search analysis using a profile likelihood ratio method with background and signal models in two unbinned dimensions. Many detailed directions were tried and searched along the way. There are a few aspects to notice for future improvements.

In this high mass WIMP search analysis, the reduction of signal efficiency, or spectrum average exposure, was over 50% due to the cut set selected, especially the tight charge fiducial volume cuts. In order to make the WIMP signal region as clean as possible so the model would be sensitive to the change of signal number N_s in it, a combination of six charge fiducial volume cuts were set and used. This analysis did not make a large effort to optimize the cut settings and this is one area that could be improved in a future analysis.

The next aspect to notice is the selection of data to generate background models. Compared to the traditional way of using only the ^{133}Ba calibration data to model the gamma background, we selected to use a strip of WIMP search open data to model the gamma

background distribution in the phonon energy dimension. This makes the gamma model less affected by the surface events. In the future, an investigation into mixing both the traditional method and the method used in this analysis may produce a better gamma background model.

The third aspect is the working parameter space. In this analysis we selected to work in the phonon recoil energy and the ionization yield space with an assumption that these two dimensions are uncorrelated. In a future analysis, a combination of more parameters could be considered and explored to see which ones provide the most powerful discrimination. Furthermore, it could be beneficial to incorporate correlated quantities into the algorithm.

The fourth aspect is the energy threshold and the low-mass WIMP region. Currently, the energy threshold of this analysis is set at 20 keV due to the energy dependent resolution and trigger efficiency of the detectors at low energy. If the detector performance at low energy was improved, this analysis could easily be extended to lower energies.

The fifth aspect is the minimization algorithm for searching the unconditional and conditional minimums and the best-fit values for all the parameters. With over 30 parameters in the likelihood function, the Migrad minimization algorithm needs thousands of function calls to find the true minimum. There are many other minimization packages and algorithms being developed. The Minuit package and the Migrad algorithm are examples of these. A new choice may shorten the running time of the script needed to find the true minimum.

The sixth aspect is to implement a safeguard against overestimating or underestimating your background in the likelihood function as described by Ref. [75]. At the earlier stage of this analysis, safeguards were implemented on both the neutron and surface backgrounds. However, at that time the tuning of cuts and the 1-D PDFs were the largest affect on the stability of the models. The protection provided by this safeguard method was only on the

order of ∼1% and introduced 20 additional nuisance parameters into the minimization process. This added significant computation time to the analysis with minimum benefit, thus it was not used in the final analysis. Further investigation into this technique in the future could result in better protection against signal-like background sources.

Last but not least, a more effective and efficient way is highly suggested to scan the interception point where the test statistic distribution meets the χ_1^2=2.706 line (90% confidence level). The interception points in different pseudo data sets may vary and different WIMP masses can affect these as well. A large interval in N_s could make the cross section limit fluctuate more, while a delicate step size may cost your computing consumption increase dramatically.

8.2. Future Experiment at SNOLAB

Lots of designs have been proposed for the geometry of the experimental setup at SuperCDMS SNOLAB. The current proposed design has changed significantly compared to years ago. An active neutron veto layer is still a promising structure but will not be available at SNOLAB due to the budget factor. The current design uses all passive shielding layers.

Since a material itself is also a source of contamination, a balance need to be made between introducing a new structure and deal with the change of background rates in the detectors. Compared to the option of plastic neutron veto layer, a liquid neutron veto system brings in a tank to hold it as well. Even with this new introduction, the ability of an neutron veto system to identify, tag and reduce those single-scatter neutrons in the detectors with at least 90% efficiency is still much more beneficial. If possible, the implementation of an active neutron veto system at SuperCDMS SNOLAB will greatly reduce the single-scatter neutron background in the detectors.

Appendix A

Neutron Emission Spectra from Uranium and Thorium Decays

In order to investigate the effect changes to the SuperCDMS SNOLAB experiment design have on the experiment's neutron background, neutron emission spectra from a number of materials are generated using SOURCES-4A software. Below are the neutron spectra I generated using SOURCES-4A for a variety of materials that were investigated during the design process. The calculations are based on the assumptions that the uranium and thorium decay chains are in secular equilibrium and that their concentration is 1 ppb.

a) Carbon Fiber Rod

Density	**Component**
1.80 g/cm^3	Carbon

Table A.1: Information about Carbon Fiber Rod.

	Uranium [$\mathbf{n{\cdot}s^{-1}{\cdot}cm^{-3}}$]	**Thorium** [$\mathbf{n{\cdot}s^{-1}{\cdot}cm^{-3}}$]
(α, n) process	3.762×10^{-11}	1.719×10^{-11}
Spontaneous fission	2.435×10^{-11}	2.814×10^{-16}
Total	6.197×10^{-11}	1.719×10^{-11}

Table A.2: Neutron Yield in Carbon Fiber Rod (see Fig. A.1).

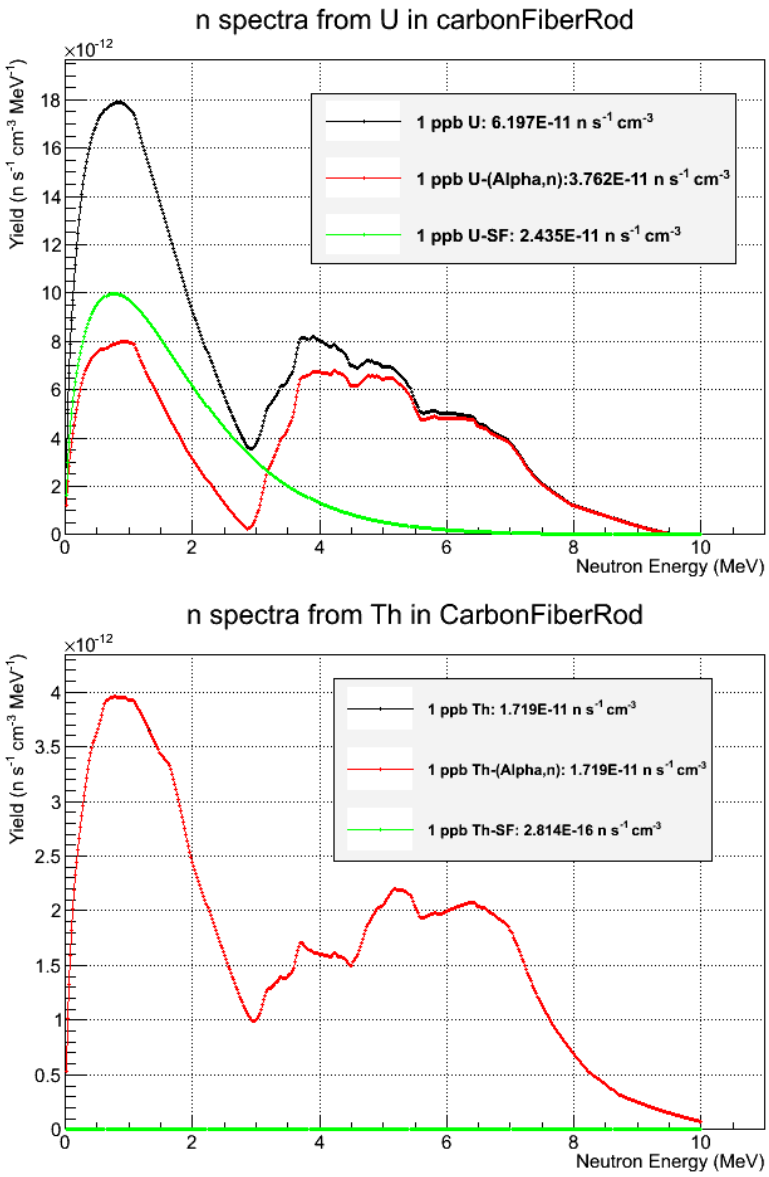

Figure A.1: Neutron emission spectra from uranium (top) and thorium (bottom) in Carbon Fiber Rod

b) Kapton

Density	**Formula**
1.42 g/cm^3	$[C_{22}H_{10}N_2O_5]_n$

Table A.3: Information about Kapton.

	Uranium [n·s^{-1}·cm^{-3}]	**Thorium [n·s^{-1}·cm^{-3}]**
(α, n) process	2.351×10^{-11}	1.296×10^{-11}
Spontaneous fission	1.921×10^{-11}	2.220×10^{-16}
Total	4.272×10^{-11}	1.296×10^{-11}

Table A.4: Neutron Yield in Kapton (see Fig. A.2).

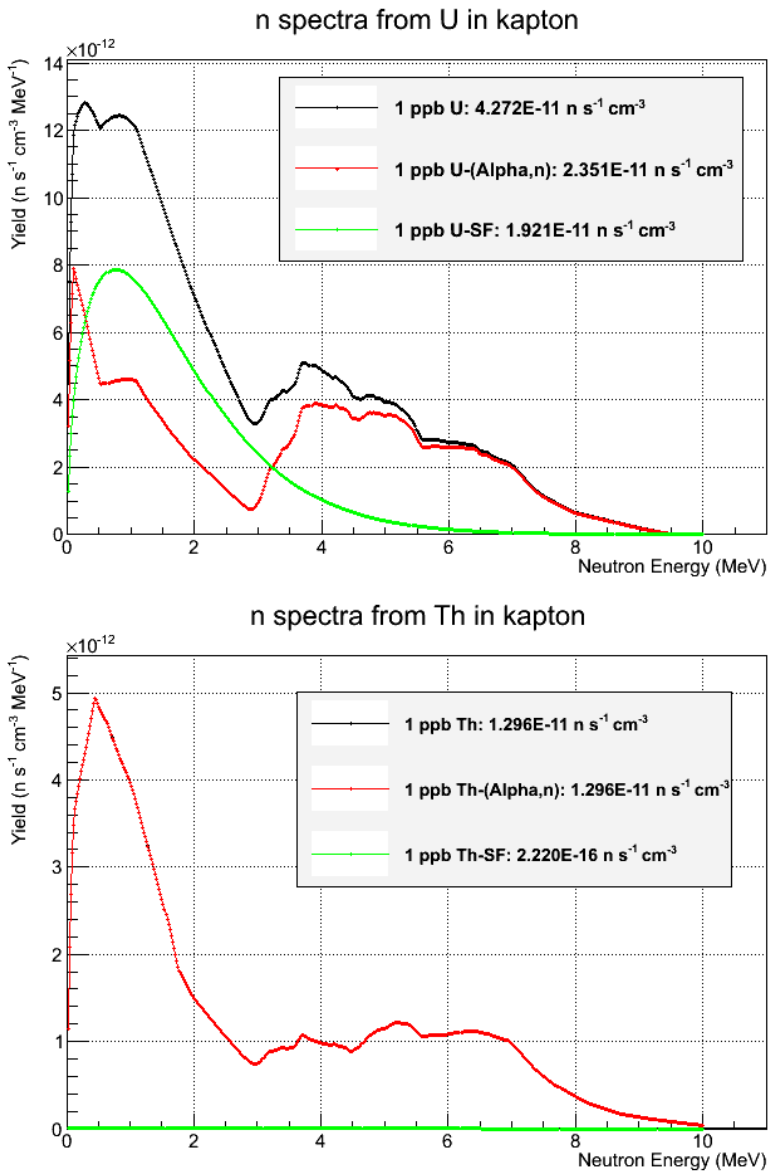

Figure A.2: Neutron emission spectra from uranium (top) and thorium (bottom) in Kapton

c) MuMetal

Element	**Mass Fraction**
C	0.02%
Si	0.35%
Mn	0.50%
Fe	14.93%
Ni	80.00%
Mo	4.20%

Table A.5: Components of MuMetal with a density of 8.747 g/cm^3.

	Uranium [$\mathbf{n{\cdot}s^{-1}{\cdot}cm^{-3}}$]	**Thorium** [$\mathbf{n{\cdot}s^{-1}{\cdot}cm^{-3}}$]
(α, n) process	1.087×10^{-11}	1.604×10^{-11}
Spontaneous fission	1.183×10^{-10}	1.367×10^{-15}
Total	1.292×10^{-10}	1.604×10^{-11}

Table A.6: Neutron Yield in MuMetal (see Fig. A.3).

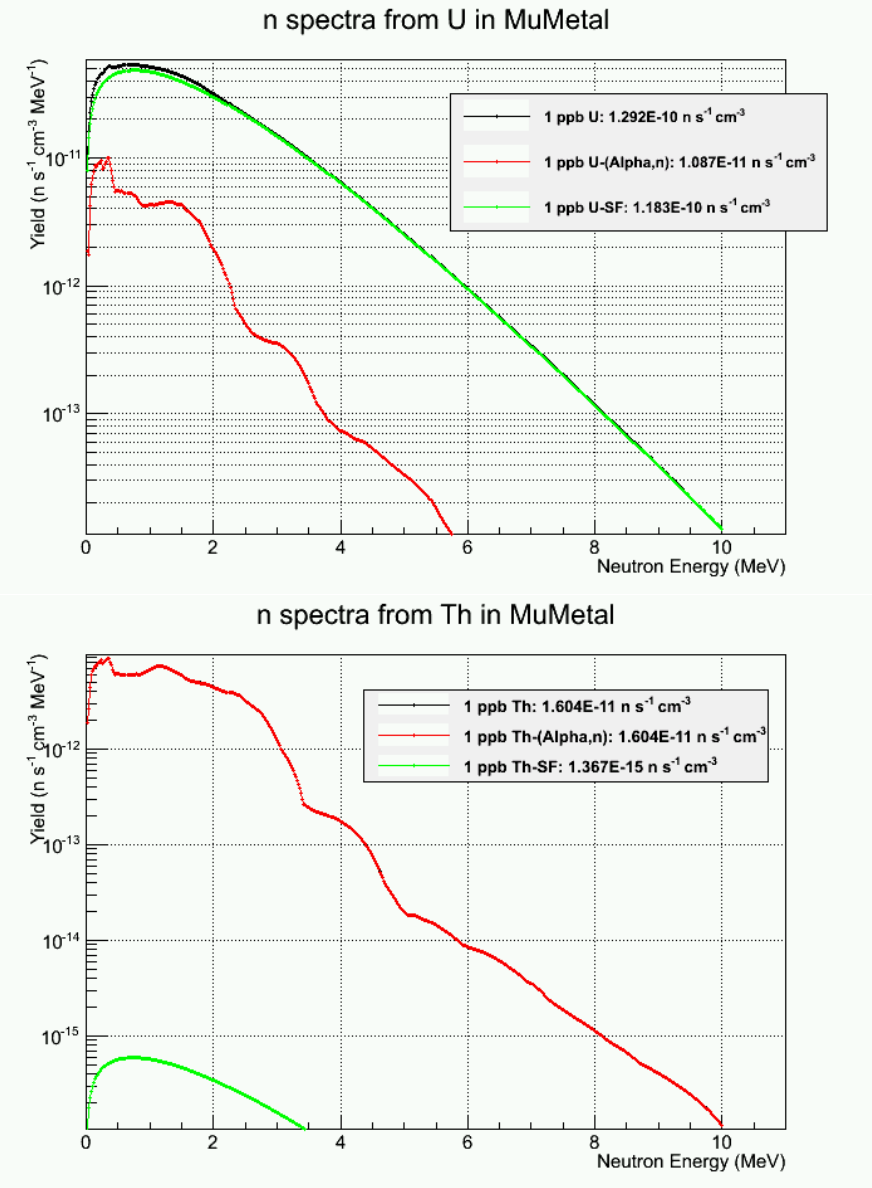

Figure A.3: Neutron emission spectra from uranium (top) and thorium (bottom) in MuMetal.

d) Shotcrete at SNOLAB

Element	Mass Fraction
Al	6.04%
Ca	9.54%
Fe	2.54%
K	1.76%
Mg	1.18%
Mn	0.37%
Na	2.25%
Si	27.9%
H	0.04%
C	0.04%
O	48.0%

Table A.7: Components of Shotcrete with a density of 2.30 g/cm^3 [76].

	Uranium [$\mathbf{n{\cdot}s^{-1}{\cdot}cm^{-3}}$]	**Thorium** [$\mathbf{n{\cdot}s^{-1}{\cdot}cm^{-3}}$]
(α, n) process	7.484×10^{-11}	1.512×10^{-11}
Spontaneous fission	3.111×10^{-11}	3.595×10^{-16}
Total	1.059×10^{-10}	1.512×10^{-11}

Table A.8: Neutron Yield in shotcrete (see Fig. A.4).

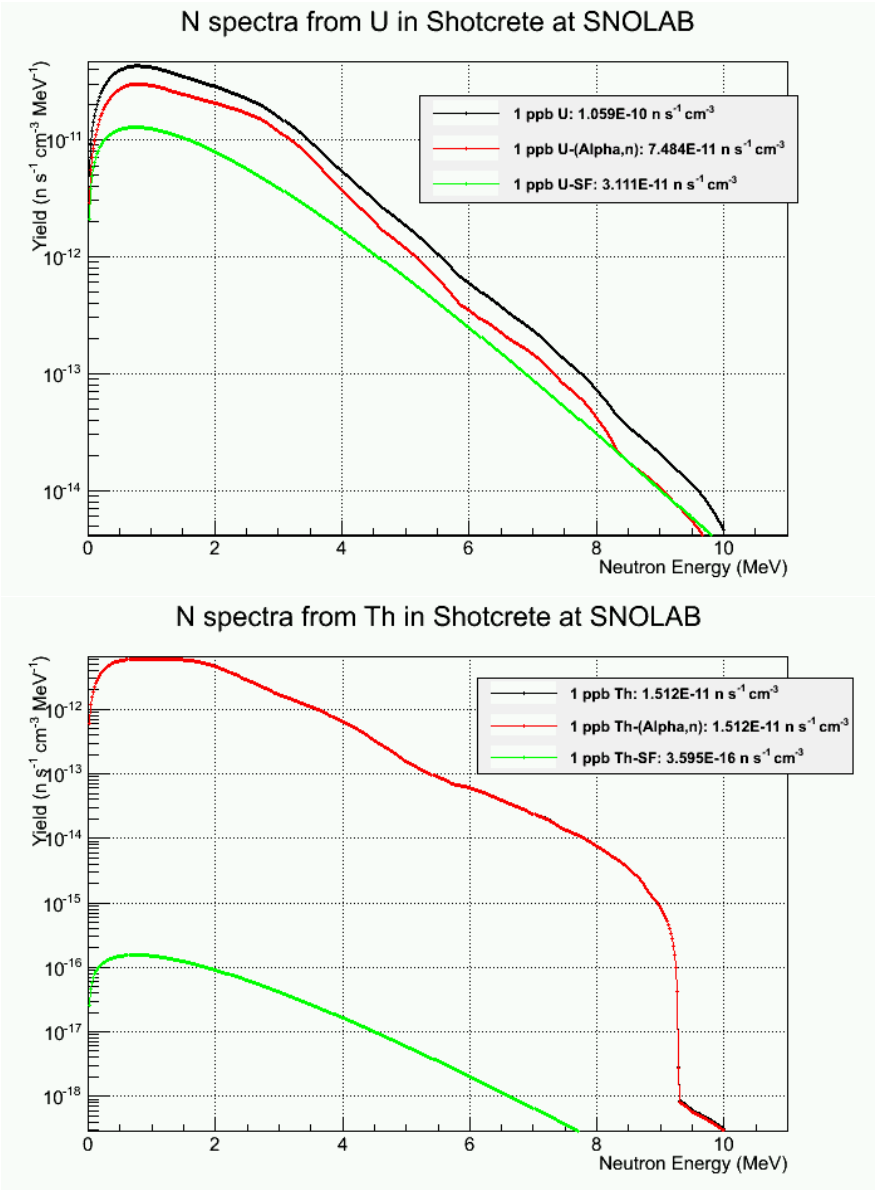

Figure A.4: Neutron emission spectra from uranium (top) and thorium (bottom) in shotcrete at SNOLAB.

Appendix B

Data Selection Criteria for the High Mass WIMP Search Analysis

We define cuts based on data quality and fiducial volume. Frequently used cuts are grouped into high level cuts such as `cGoodEv_v53` and `cLiveTime_v53_HT` to help maintain consistency. Each cut in the list below comes with a short description in one sentence. The purpose of this section is to provide a brief introduction to the cut's purpose. A "$\sim$" sign is placed in front of cuts where the "NOT" condition applies. More detailed cut development summary can be found in this dissertation [77].

Cut Category	**Table**
Fundamental Data Quality	B.2, B.3, B.4, B.5
Fiducial Volume Signal Selection	B.6, B.7, B.8
Muon Veto	B.9
Single-scatter NR Selection	B.10

Table B.1: A summary guide to cut tables.

Individual Cut	Description
cPChiSq_v53	Removes events with high phonon χ^2 values
cPstd_v53	Removes events with phonon prepulse noise not consistent with series phonon noise
∼cGlitch1_v53	Removes high frequency phonon glitches based on optimal filter template comparison
Empty=0	Removes events in the detectors with no trigger (except for the WIMP search data)
∼cLFnoise1_v53	Removes low frequency noise based on optimal filter template comparison
∼cGlitch_133	Removes events with large differences between charge and phonon trigger numbers
cGoodPStartTime_v53	Removes events with PTOFdelay outside a time range around the global phonon trigger
∼cPsat_133	Removes events having saturated pulse in at least one phonon channel
cQChiSq_v53	Removes events with high charge χ^2 values
cQstd_v53	Removes events with charge pre-pulse noise not consistent with series charge noise
∼cQsat_133	Removes events having saturated pulse in at least one charge channel

Table B.2: Individual Cuts in cGoodEv_v53 umbrella cut.

Individual Cut	Description
c133	Selects series in the run 133 time period (01/01/2012-07/10/2013)
c134	Selects series in the run 134 time period (07/10/2013-07/17/2014)
c135	Selects series in the run 135 time period (after 09/08/2014)
cGoodBiasTime_133	Removes series with too long data collection time
∼cBadSeries_133	Removes series marked as "bad" in the DQ table and a few other bad problems
∼cBadGPStime_133	Removes events with abs(GPS_time-EventTime)>17 s
cFinalPhononSettings_133	Removes bad series related to QET and SQUID settings
∼cTrigBurst_133	Removes series experiencing trigger bursts or partial trigger bursts
∼cErrMask_133	Removes problematic events identified by the ErrorMask RQ
cGoodDCOffset_v53	Removes events with a DC offset larger than a certain distance from the mean DC offset
cGoodBaseTemp_v53	Removes events or short period of events collected when the base temperature was not in the good range
∼cQhighnoise_v53	Removes events or short period of events occurring in a high charge noise environment
∼cBadLED_v53	Removes periods with not-good LED status
∼cSquarePulse_v53	Removes events showing square pulses in the phonon channels
∼cBadOFRes_v53	Removes series with poor optimal filter energy resolutions
cGoodHV_v53	Removes events with non-consistent CDMSlite HV bias
∼cNoTrigEnable_v53	Removes zero livetime events with no trigger-enable bits found
∼cGlitch_133	Removes events with large differences between charge and phonon trigger numbers

Table B.3: Individual Cuts in cLiveTime_v53_HT umbrella cut (continue in the next page).

Individual Cut	Description
cPstd_v53	Removes events with phonon pre-pulse noise not consistent with series phonon noise
cQstd_v53	Removes events with charge pre-pulse noise not consistent with series charge noise
cWSBias_133_HT	Removes series not with +2V/-2V voltage bias configuration
cGoodRandomChi2_v53_HT	Removes series with abnormal charge/phonon χ^2 behaviors
Empty=0	Removes events in the detectors with no trigger (except for the WIMP search data)
∼EventCategory=1	Removes Random events
cDataPeriod_v53_HT	Removes series not to be used in the HT analysis
∼cPostCf_133_HT	Removes series within 48 hours after a Cf calibration
cStableTrigThresh_133_HT	Removes series from the periods when trigger thresholds change rapidly
∼cCDMSlite_v53	Removes series in iT5Z2 when CDMSlite mode is on
∼cNuMI_133	Removes events within 200 μs of an event in the NuMI beam
cGoodKStest_v53_HT	Removes series failing the standard Kolmogorov-Smirnov (KS) test
cGoodQStest_v53_HT	Removes series falling the KS-style test on the ionization quantities

Table B.4: Individual Cuts in cLiveTime_v53_HT umbrella cut.

Individual Cut	Description
cAnalysisThreshold_v53_HT	Removes low energy events
cTriggeredEvent_133_HT	Removes events not having a trigger near the global trigger within a certain period of time
∼cRandom_133	Removes Random events

Table B.5: Individual Cuts in parallel with cGoodEv_v53 and cLiveTime_v53_HT umbrella cuts.

Individual Cut	Description
∼cSpot_v53_HT	Removes events located in the DIB2 hot spot
cPCfSVM_2pct_Sandbox_v53_HT	Removes outliers not consistent with real events using phonon partition values
cQthresh_v53_HT	Removes events with charge energies below selected charge energy thresholds
20<precoiltNF<150 keV	Selects events with phonon recoil energy within 20 and 150 keV selected phonon energy thresholds
-0.2<qrpartOF<0.5	Removes events with charge radial partition values outside [-0.2, 0.5]
-0.3<qzpartOF<0.3	Removes events with charge depth partition values outside [-0.3, 0.3]
pzpartOF<0 in iT3Z1	Removes events within the upper half of iT3Z1 using phonon depth partition
pzpartOF>0 in iT3Z3	Removes events within the lower half of iT3Z3 using phonon depth partition

Table B.6: List of pre-selection cuts.

Individual Cut	Description
cQin1_blind_v53	Removes events outside the blinding charge radial fiducial volume using side 1 charge energies
cQin2_blind_v53	Removes events outside the blinding charge radial fiducial volume using side 2 charge energies
cQsym_blind_v53	Removes events outside the blinding charge depth fiducial volume using summed charge energies from side 1 and side 2

Table B.7: List of Ionization Fiducial Volume cuts.

Individual Cut	Description
cNR_ytNF_3sigma_v53_HT	Removes events outside the 3σ NR bands in ytNF-precoiltNF plane

Table B.8: Nuclear Recoil Event Selection cut.

Individual Cut	Description
∼cVT_strict_v53	Selects events with veto triggers NOT in a [-50, 0] μs time window with respect to the global trigger

Table B.9: Veto cut.

Individual Cut	Description
∼cPmultTight_v53_HT	Selects events with triggers in only one detector and neither a glitch nor low frequency noise

Table B.10: Single Scattering Event Selection cut.

Appendix C

Statistical Methods

Statistical methods are widely used in the data analysis of physics field. From probability, distribution, to hypothesis test, limit setting and discovery claim, statistics provide powerful tools and techniques for data analyzers. In this section, a brief introduction to some common used statistical tools is presented [78].

C.1. Some Common Distributions

When interactions happen in the detectors, events are recorded if they pass certain selection criteria. Not all good event candidates pass these selections. There is an efficiency associated with each selection criteria. This could be described by a binomial distribution. With a detector efficiency ϵ, a number of m good events are expected to be recorded when a number of N events hit on a detector.

A multinomial distribution can be used to describe a given number of physics events plotted as a histogram of a variable (e.g. phonon recoil energy). It is natural that detectors have non-zero resolutions. When an event is recorded, there is an uncertainty with each of its true physics variable value. A Gaussian distribution is a great tool to describe detector resolutions. Once you have a histogram and want to look at the information in each bin, this acts as a counting problem. SuperCDMS is a rare event search experiment and often it has to deal with low statistics situation, which brings the Poisson distribution onto the analysis stage.

A **Binomial distribution** can be used to describe our detector efficiency. As in the classic coin flip experiment or the dice rolling experiment, one either gets the desired result

or doesn't get it. If one does the same experiment N times, the probability to get the desired result each time is p, then at the end of these N experiments, the probability one could get the desired result m times is

$$P(m; N, p) = \frac{N!}{m!\,(N-m)!} p^m (1-p)^{N-m} \tag{C.1}$$

The mean value of m is

$$< m >= N\,p \tag{C.2}$$

and its variance is

$$Var[m] = N\,p\,(1-p) \tag{C.3}$$

A **Multinomial distribution** can be used to describe the event distribution among the different bins in a histogram when the total number of events N is fixed. If there are k bins in total in the histogram and an event falls into the ith bin is p_i, with m_i events in the ith bin, the joint distribution is

$$P(m_1, m_2, ..., m_k; N) = N! \prod_{i=1}^{k} \frac{p_i^{m_i}}{m_i!} \tag{C.4}$$

A **Gaussian distribution** is widely used in many areas. One application is to describe energy resolution in our detectors. Unlike the above two distributions, Gaussian is a continuous distribution and its parameters are not restricted to be positive only. The general form of a Gaussian distribution, also called a normal distribution, is as following

$$G(x; \mu, \sigma) = \frac{1}{\sqrt{2\pi}\,\sigma}\, e^{-\frac{(x-\mu)^2}{2\sigma^2}} \tag{C.5}$$

where μ is the mean value of x and σ is the standard deviation of x. There is a special case when $\mu = 0$ and $\sigma = 1$, and this is called a **standard normal distribution**. Its form is much simpler

$$G(x; \mu = 0, \sigma = 1) = N(0, 1) = \frac{1}{\sqrt{2\pi}}\, e^{-\frac{x^2}{2}} \tag{C.6}$$

when selecting a Gaussian kernel to do a kernel density estimate for a variable, the standard normal distribution is often an excellent choice.

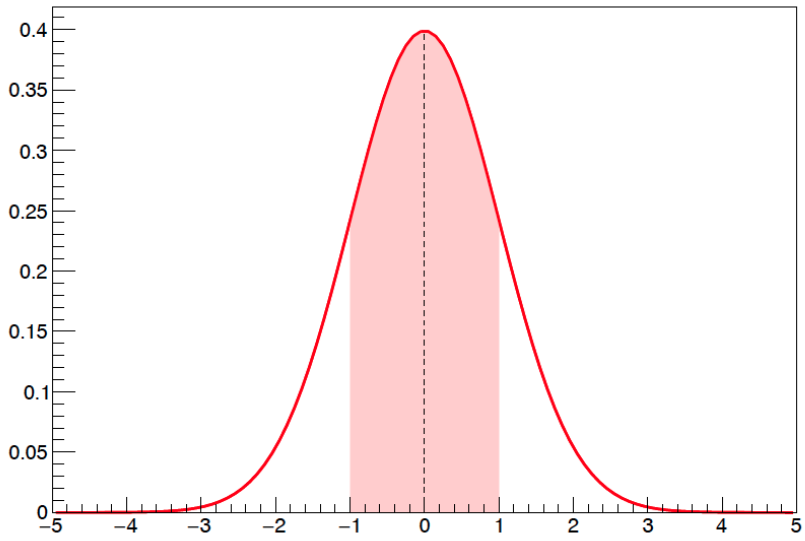

Figure C.1: Example of a standard normal distribution. The colored area corresponds to the distribution within $\pm 1\sigma$.

A **Poisson distribution** is often used in low statistic counting. When dealing with a large sample size, the distribution of the random variable approaches approximately a Gaussian distribution due to the central limit theorem. One could still use a Poisson distribution on a large sample, but it would be less efficient compared to using a Gaussian distribution approximation. The Poisson distribution is given by

$$P(n;\nu) = \frac{\nu^n}{n!}\, e^{-\nu} \tag{C.7}$$

where ν is the expected value of n and $\sqrt{\nu}$ is the standard deviation of n. When looking at the information of a single bin in a histogram, Poisson distribution is a quite useful tool.

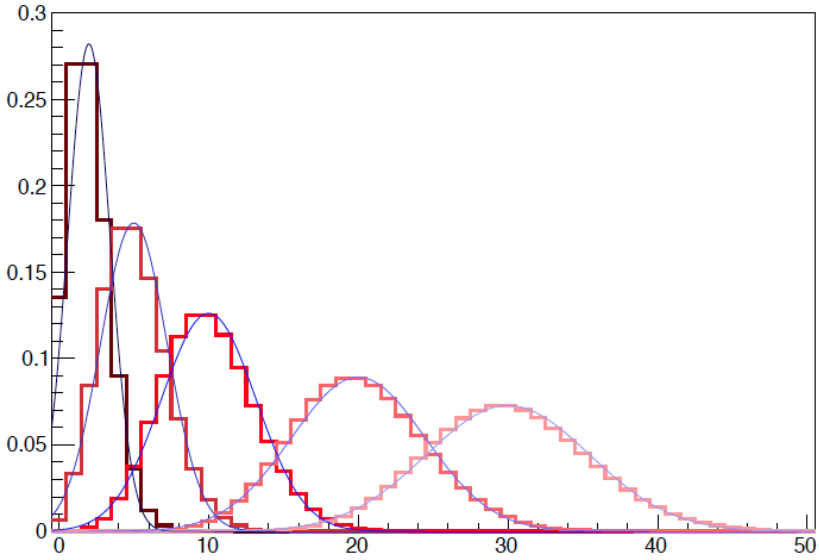

Figure C.2: Example of Poisson distributions with different expected values ν in histograms. In comparison, the continuous curves are Gaussian distributions with $\mu = \nu$ and $\sigma = \sqrt{\nu}$.

C.2. Extended Likelihood

In a real experiment, there are a group of random variables $x_1, x_2, ..., x_n$ of interest. These variables are also called the parameters of interest for the experiment. There are many other variables $\theta_1, \theta_2, ..., \theta_m$ in the experiment that are not of interest, but the parameters of interest are dependent on them. This group of variables are called nuisance parameters. Their values may be unknown. For each interested event, a likelihood function can be used to describe it as

$$L = f(x_1, x_2, ..., x_n; \theta_1, \theta_2, ..., \theta_m) \tag{C.8}$$

If in the experiment there are N independent observations, the combined likelihood function of the experiment is the product of all the individual likelihood functions

$$L = \prod_{i=1}^{N} L_i = \prod_{i=1}^{N} f(x_1^i, x_2^i, ..., x_n^i; \theta_1, \theta_2, ..., \theta_m) \tag{C.9}$$

In most experiments, even the total sample size N is a variable and it follows a Poisson distribution with an expected value of ν. Thus, the extended likelihood function is introduced to describe this situation

$$L_{extended} = Poisson(N; \nu(\theta_1, \theta_2, ..., \theta_m)) \prod_{i=1}^{N} L_i \tag{C.10}$$

where Poisson(N; $\nu(\theta_1, \theta_2, ..., \theta_m)$) puts a constraint on the variable N in the extended likelihood function

$$Poisson(N; \nu(\theta_1, \theta_2, ..., \theta_m)) = \frac{\nu(\theta_1, \theta_2, ..., \theta_m)^N}{N!} e^{-\nu(\theta_1, \theta_2, ..., \theta_m)} \tag{C.11}$$

In an experiment like SuperCDMS, the expected value of N is the sum of signal candidate N_s and background candidate N_b. In this case, with the notations $\vec{x} = (x_1, x_2, ..., x_n)$ and $\vec{\theta} = (\theta_1, \theta_2, ..., \theta_m)$ and $\nu = N_s + N_b$, the extended likelihood function converts to

$$L_{extended}(\vec{x}; N_s, N_b, \vec{\theta}) = \frac{(N_s + N_b)^N}{N!} e^{-(N_s + N_b)} \prod_{i=1}^{N} [f_s \times P_s(x_i; \vec{\theta}) + f_b \times P_b(x_i; \vec{\theta})] \tag{C.12}$$

where f_s and f_b are the relative fractions of signal and background expected events

$$\begin{aligned} f_s &= \frac{N_s}{N_s + N_b} \\ f_b &= \frac{N_b}{N_s + N_b} \end{aligned} \tag{C.13}$$

With some derivation, the form of the above extended likelihood function can easily be simplified to

$$L_{extended}(\vec{x}; N_s, N_b, \vec{\theta}) = \frac{e^{-(N_s + N_b)}}{N!} \prod_{i=1}^{N} [N_s \times P_s(x_i; \vec{\theta}) + N_b \times P_b(x_i; \vec{\theta})] \tag{C.14}$$

where P_s and P_b are the best-fit probability distribution functions for signal and background events.

C.3. Hypothesis Test

When doing data analysis, what the analyzers really want to figure out is that whether the result from analysis is compatible with the theory model they assume or an alternate theory model. These two models are called the null hypothesis, H_0, and the alternative hypothesis, H_1. Below are some examples of H_0 and H_1.

- Example 1:
  - H_0: A particle is an electron
  - H_1: A particle is a tauon
- Example 2:
  - H_0: A data sample consists of only background
  - H_1: A data sample consists of background and the Higgs boson
- Example 3:
  - H_0: A nuclear recoil event is caused by a neutron
  - H_1: A nuclear recoil event is caused by a WIMP

Usually the alternative hypothesis is what the analyzers want to prove to be true from the data. But in order to reach that conclusion, they have to reject the null hypothesis. This process is called hypothesis test. A variable that is selected to perform this test is called a test statistic. Its value can be calculated from the data sample and used as a discriminator between H_0 and H_1. For example, the ionization yield quantity in SuperCDMS is such a variable that can be used to discriminate nuclear recoil events from electron recoil events. If more than one variable is used in the discrimination procedure and they are combined, it would be called as a multi-variate analysis.

There are two quantities that are mostly used in the hypothesis test. They could help analyzers to determine whether they would prefer the null hypothesis or accept the alternative

hypothesis while rejecting the null hypothesis. The first useful quantity is p-value. It is a probability calculated from the constructed test statistic. It could be used as a discriminator between H_0 and H_1. For example, if the p-value of a test statistic is 0.7, it indicates that if repeating an experiment under the same condition 100 times, 70% of the time the result would be consistent with the null hypothesis.

The second useful quantity is the significance level α. It is a value set to determine whether H_1 could be accepted and H_0 could be rejected. For example, if α is set to be 0.01, it means that analyzers could only tolerate as low as 1% of the time the result is consistent with the null hypothesis when repeating the same experiment multiple times. If a p-value of a test statistic is 0.003, it indicates that the H_1 is preferred over H_0. α is also called type I error because H_0 could still hold true even the p-value is smaller than it. When a value is chosen for α, it brings in a risk as well.

BIBLIOGRAPHY

[1] F. Zwicky, Die Rotverschiebung von extragalaktischen Nebeln, Helv. Phys. Acta 6 (1933) 110–127, [Gen. Rel. Grav.41,207(2009)]. doi:10.1007/s10714-008-0707-4.

[2] F. Zwicky, On the Masses of Nebulae and of Clusters of Nebulae, Astrophys. J. 86 (1937) 217–246. doi:10.1086/143864.

[3] V. C. Rubin, W. K. Ford, Jr., Rotation of the Andromeda Nebula from a Spectroscopic Survey of Emission Regions, Astrophys. J. 159 (1970) 379–403. doi:10.1086/150317.

[4] J. Liesenborgs, Rotation curve of a galaxy, citizendium (2007).

[5] M. Markevitch, A. H. Gonzalez, D. Clowe, A. Vikhlinin, L. David, W. Forman, C. Jones, S. Murray, W. Tucker, Direct constraints on the dark matter self-interaction cross-section from the merging galaxy cluster 1E0657-56, Astrophys. J. 606 (2004) 819–824. arXiv:astro-ph/0309303, doi:10.1086/383178.

[6] A. A. Penzias, R. W. Wilson, A Measurement of excess antenna temperature at 4080-Mc/s, Astrophys. J. 142 (1965) 419–421. doi:10.1086/148307.

[7] A. H. Guth, The Inflationary Universe: A Possible Solution to the Horizon and Flatness Problems, Phys. Rev. D23 (1981) 347–356. doi:10.1103/PhysRevD.23.347.

[8] ESA, the Planck Collaboration, Planck CMB, EUROPEAN SPACE AGENCY (2013).

[9] R. Adam, et al., Planck 2015 results. I. Overview of products and scientific results, Astron. Astrophys. 594 (2016) A1. arXiv:1502.01582, doi:10.1051/0004-6361/201527101.

[10] C. J. Copi, D. N. Schramm, M. S. Turner, Big bang nucleosynthesis and the baryon density of the universe, Science 267 (1995) 192–199. arXiv:astro-ph/9407006, doi:10.1126/science.7809624.

[11] V. Trimble, Existence and Nature of Dark Matter in the Universe, Ann. Rev. Astron. Astrophys. 25 (1987) 425–472. doi:10.1146/annurev.aa.25.090187.002233.

[12] L. Bergstrm, Nonbaryonic dark matter: Observational evidence and detection methods, Rept. Prog. Phys. 63 (2000) 793. arXiv:hep-ph/0002126, doi:10.1088/0034-4885/63/5/2r3.

[13] G. Bertone, Particle dark matter: observations, models and searches, Cambridge Univ. Press, Cambridge, 2010.
URL https://cds.cern.ch/record/1235368

[14] R. S. Somerville, J. R. Primack, The Star Formation History in a Hierarchical UniversearXiv:astro-ph/9811001.

[15] J. L. Feng, Dark Matter Candidates from Particle Physics and Methods of Detection, Ann. Rev. Astron. Astrophys. 48 (2010) 495–545. arXiv:1003.0904, doi:10.1146/annurev-astro-082708-101659.

[16] J. Ellis, K. A. Olive, Supersymmetric Dark Matter CandidatesarXiv:1001.3651.

[17] G. Jungman, M. Kamionkowski, K. Griest, Supersymmetric dark matter, Phys. Rept. 267 (1996) 195–373. arXiv:hep-ph/9506380, doi:10.1016/0370-1573(95)00058-5.

[18] O. Klein, Quantentheorie und fünfdimensionale relativitätstheorie, Zeitschrift für Physik 37 (12) (1926) 895–906. doi:10.1007/BF01397481.
URL http://dx.doi.org/10.1007/BF01397481

[19] M. B. Green, J. H. Schwarz, Supersymmetrical String Theories, Phys. Lett. B109 (1982) 444–448. doi:10.1016/0370-2693(82)91110-8.

[20] E. Witten, String theory dynamics in various dimensions, Nucl. Phys. B443 (1995) 85–126. arXiv:hep-th/9503124, doi:10.1016/0550-3213(95)00158-O.

[21] R. D. Peccei, H. R. Quinn, CP, Phys. Rev. Lett. 38 (1977) 1440–1443. doi:10.1103/PhysRevLett.38.1440.
URL http://link.aps.org/doi/10.1103/PhysRevLett.38.1440

[22] A. Kusenko, Sterile neutrinos: The Dark side of the light fermions, Phys. Rept. 481 (2009) 1–28. arXiv:0906.2968, doi:10.1016/j.physrep.2009.07.004.

[23] K. Garrett, G. Duda, Dark Matter: A Primer, Adv. Astron. 2011 (2011) 968283. arXiv:1006.2483, doi:10.1155/2011/968283.

[24] C. Csaki, The Minimal supersymmetric standard model (MSSM), Mod. Phys. Lett. A11 (1996) 599. arXiv:hep-ph/9606414, doi:10.1142/S021773239600062X.

[25] T. Marrodn Undagoitia, L. Rauch, Dark matter direct-detection experiments, J. Phys. G43 (1) (2016) 013001. arXiv:1509.08767, doi:10.1088/0954-3899/43/1/013001.

[26] L. Baudis, Dark matter searches, Int. J. Mod. Phys. A21 (2006) 1925–1937, [,350(2005)]. arXiv:astro-ph/0511805, doi:10.1142/S0217751X06032873.

[27] Y. A. Ramachers, WIMP direct detection overview, Nucl. Phys. Proc. Suppl. 118 (2003) 341–350, [,341(2002)]. arXiv:astro-ph/0211500, doi:10.1016/S0920-5632(03)01327-6.

[28] R. Agnese, et al., Search for Low-Mass Weakly Interacting Massive Particles with SuperCDMS, Phys. Rev. Lett. 112 (24) (2014) 241302. arXiv:1402.7137, doi:10.1103/PhysRevLett.112.241302.

[29] E. Armengaud, et al., Constraints on low-mass WIMPs from the EDELWEISS-III dark matter search, JCAP 1605 (05) (2016) 019. arXiv:1603.05120, doi:10.1088/1475-7516/2016/05/019.

[30] D. S. Akerib, et al., Results from a search for dark matter in the complete LUX exposure, Phys. Rev. Lett. 118 (2) (2017) 021303. arXiv:1608.07648, doi:10.1103/PhysRevLett.118.021303.

[31] E. Aprile, et al., XENON100 Dark Matter Results from a Combination of 477 Live Days, Phys. Rev. D94 (12) (2016) 122001. arXiv:1609.06154, doi:10.1103/PhysRevD.94.122001.

[32] J. Schieck, et al., Direct Dark Matter Search with the CRESST II Experiment, in: 38th International Conference on High Energy Physics (ICHEP 2016) Chicago, IL, USA, August 03-10, 2016, 2016. arXiv:1611.02113.
URL https://inspirehep.net/record/1495962/files/arXiv:1611.02113.pdf

[33] G. Bertone, D. Merritt, Dark matter dynamics and indirect detection, Mod. Phys. Lett. A20 (2005) 1021. arXiv:astro-ph/0504422, doi:10.1142/S0217732305017391.

[34] E. Charles, et al., Sensitivity Projections for Dark Matter Searches with the Fermi Large Area Telescope, Phys. Rept. 636 (2016) 1–46. arXiv:1605.02016, doi:10.1016/j.physrep.2016.05.001.

[35] M. Aguilar, et al., First result from the alpha magnetic spectrometer on the international space station: Precision measurement of the positron fraction in primary cosmic rays of 0.5˘350 gev, Phys. Rev. Lett. 110 (2013) 141102.
doi:10.1103/PhysRevLett.110.141102.
URL https://link.aps.org/doi/10.1103/PhysRevLett.110.141102

[36] H. Abdalla, et al., H.e.s.s. limits on linelike dark matter signatures in the 100 gev to 2 tev energy range close to the galactic center, Phys. Rev. Lett. 117 (2016) 151302.
doi:10.1103/PhysRevLett.117.151302.
URL https://link.aps.org/doi/10.1103/PhysRevLett.117.151302

[37] M. G. Aartsen, et al., Search for annihilating dark matter in the Sun with 3 years of IceCube data, Eur. Phys. J. C77 (3) (2017) 146. arXiv:1612.05949, doi:10.1140/epjc/s10052-017-4689-9.

[38] V. A. Mitsou, Overview of searches for dark matter at the LHC, J. Phys. Conf. Ser. 651 (1) (2015) 012023. arXiv:1402.3673, doi:10.1088/1742-6596/651/1/012023.

[39] A. Shcherbakova, Search for dark matter with the ATLAS detector at the LHC, J. Phys. Conf. Ser. 798 (1) (2017) 012100. doi:10.1088/1742-6596/798/1/012100.

[40] J. Andrea, Search for Dark Matter with top quarks, in: 9th International Workshop on Top Quark Physics (TOP 2016) Olomouc, Czech Republic, September 19-23, 2016, 2017. arXiv:1701.03046.
URL https://inspirehep.net/record/1508614/files/arXiv:1701.03046.pdf

[41] M. W. Goodman, E. Witten, Detectability of Certain Dark Matter Candidates, Phys. Rev. D31 (1985) 3059. doi:10.1103/PhysRevD.31.3059.

[42] J. D. Lewin, P. F. Smith, Review of mathematics, numerical factors, and corrections for dark matter experiments based on elastic nuclear recoil, Astropart. Phys. 6 (1996) 87–112. doi:10.1016/S0927-6505(96)00047-3.

[43] L. Baudis, Direct dark matter detection: the next decade, Phys. Dark Univ. 1 (2012) 94–108. arXiv:1211.7222, doi:10.1016/j.dark.2012.10.006.

[44] J. Lindhard, V. Nielsen, M. Scharff, P. Thomsen, Integral equations governing radiation effects. (notes on atomic collisions, iii), Kgl. Danske Videnskab., Selskab. Mat. Fys. Medd. Vol: 33: No. 10.

[45] D. K. Ferry, Semiconductors, 2053-2563, IOP Publishing, 2013. doi:10.1088/978-0-750-31044-4.
URL http://dx.doi.org/10.1088/978-0-750-31044-4

[46] R. Agnese, et al., Demonstration of Surface Electron Rejection with Interleaved Germanium Detectors for Dark Matter Searches, Appl. Phys. Lett. 103 (2013) 164105. arXiv:1305.2405, doi:10.1063/1.4819835,10.1063/1.4826093.

[47] J. Yen, "R133 - Continued Study on Detector-Detector Charge X-talk", CDMS Internal Online Note (2013).

[48] H. J. Maris, Phonon propagation with isotope scattering and spontaneous anharmonic decay, Phys. Rev. B 41 (1990) 9736–9743. doi:10.1103/PhysRevB.41.9736.
URL http://link.aps.org/doi/10.1103/PhysRevB.41.9736

[49] P. N. Luke, Voltageassisted calorimetric ionization detector, Journal of Applied Physics 64 (12) (1988) 6858–6860.
arXiv:http://dx.doi.org/10.1063/1.341976, doi:10.1063/1.341976.
URL http://dx.doi.org/10.1063/1.341976

[50] M. Pyle, Optimizing the Design and Analysis of Cryogenic Semiconductor Dark Matter Detectors for Maximum Sensitivity, Ph.D. Thesis (2012).

[51] A. Lindote, H. M. Araujo, V. A. Kudryavtsev, M. Robinson, Simulation of neutrons produced by high-energy muons underground, Astropart. Phys. 31 (2009) 366–375. arXiv:0810.1682, doi:10.1016/j.astropartphys.2009.03.008.

[52] SuperCDMS Simulation Group, "SuperCDMS Simulation", CDMS Internal Online Page.

[53] S. Agostinelli, et al., Geant4a simulation toolkit, Nuclear Instruments and Methods in Physics Research Section A: Accelerators, Spectrometers, Detectors and Associated Equipment 506 (3) (2003) 250 – 303. doi:http://doi.org/10.1016/S0168-9002(03)01368-8. URL http://www.sciencedirect.com/science/article/pii/S0168900203013688

[54] W. Wilson, R. Perry, W. Charlton, T. Parish, G. Estes, T. Brown, E. Arthur, M. Bozoian, T. England, D. Madland, J. Stewart, Sources 4a: A code for calculating (alpha,n) , spontaneous fission and delayed neutron sources and spectra, Tech. Rep. LA-13639-MS, Los Alamos National Laboratory (1999).

[55] Daechang co.,ltd, Material Safety Data Sheet: Copper and Copper Alloy Brass (C3604).

[56] SuperCDMS, "DOE Proposal: The SuperCDMS SNOLAB Experiment", CDMS Internal Online Document (2013).

[57] D. A. Abdushukurov, M. A. Abduvokhidov, D. V. Bondarenko, K. K. Muminov, T. A. Toshov, D. Yu. Chistyakov, Modeling the registration efficiency of thermal neutrons by gadolinium foils, JINST 2 (2007) P04001. arXiv:physics/0611225, doi:10.1088/1748-0221/2/04/P04001.

[58] J. B. Birks, Scintillations from Organic Crystals: Specific Fluorescence and Relative Response to Different Radiations, Proc. Phys. Soc. A64 (1951) 874–877. doi:10.1088/0370-1298/64/10/303.

[59] S. Westerdale, et al., Quenching Measurements and Modeling of a Boron-Loaded Organic Liquid ScintillatorarXiv:1703.07214.

[60] W. Beriguete, et al., Production of a gadolinium-loaded liquid scintillator for the Daya Bay reactor neutrino experiment, Nucl. Instrum. Meth. A763 (2014) 82–88. arXiv:1402.6694, doi:10.1016/j.nima.2014.05.119.

[61] R. Agnese, et al., Search for Low-Mass Weakly Interacting Massive Particles Using Voltage-Assisted Calorimetric Ionization Detection in the SuperCDMS Experiment, Phys. Rev. Lett. 112 (4) (2014) 041302. arXiv:1309.3259, doi:10.1103/PhysRevLett.112.041302.

[62] R. Calkins, "Nuclear and Electron Recoil Band Fits for the ytNF-precoiltNF Yield Plane", CDMS Internal Online Note (2015).

[63] B. Welliver, E. Lopez, "CAP Blinding Cut", CDMS Internal Online Note (2014).

[64] A. Anderson, "R133 Charge Calibration v2", CDMS Internal Online Note (2013).

[65] T. Doughty, "Run 134 - Calibration Check", CDMS Internal Online Note (2014).

[66] T. Doughty, "Run 134 - Final Preprocessing Check", CDMS Internal Online Note (2014).

[67] K. S. Cranmer, Kernel estimation in high-energy physics, Comput. Phys. Commun. 136 (2001) 198–207. arXiv:hep-ex/0011057, doi:10.1016/S0010-4655(00)00243-5.

[68] T. Doughty, "Lead Source Surface Background Model", CDMS Internal Online Note (2015).

[69] J. Neyman, E. S. Pearson, On the problem of the most efficient tests of statistical hypotheses, Philosophical Transactions of the Royal Society of London A: Mathematical, Physical and Engineering Sciences 231 (694-706) (1933) 289–337. arXiv:http://rsta.royalsocietypublishing.org/content/231/694-706/289.full.pdf, doi:10.1098/rsta.1933.0009.
URL http://rsta.royalsocietypublishing.org/content/231/694-706/289

[70] S. S. Wilks, The Large-Sample Distribution of the Likelihood Ratio for Testing Composite Hypotheses, Annals Math. Statist. 9 (1) (1938) 60–62. doi:10.1214/aoms/1177732360.

[71] F. James, M. Winkler, MINUIT User's Guide.

[72] T. Doughty, "Radiogenic Neutron Background Model", CDMS Internal Online Note (2016).

[73] Z. Ahmed, et al., Combined Limits on WIMPs from the CDMS and EDELWEISS Experiments, Phys. Rev. D84 (2011) 011102. arXiv:1105.3377, doi:10.1103/PhysRevD.84.011102.

[74] G. Cowan, K. Cranmer, E. Gross, O. Vitells, Asymptotic formulae for likelihood-based tests of new physics, Eur. Phys. J. C71 (2011) 1554, [Erratum: Eur. Phys. J.C73,2501(2013)]. arXiv:1007.1727, doi:10.1140/epjc/s10052-011-1554-0,10.1140/epjc/s10052-013-2501-z.

[75] N. Priel, L. Rauch, H. Landsman, A. Manfredini, R. Budnik, A model independent safeguard for unbinned LikelihoodarXiv:1610.02643.

[76] I. Lawson, Analysis of Rock Samples from the New Laboratory (2007).

[77] B. Welliver, Dedicated Searches For Low And High Mass Wimps With The SuperCDMS Soudan iZIP Detectors, Ph.D. Thesis (2015).

[78] L. Lista, Practical Statistics for Particle Physicists, in: 2016 European School of High-Energy Physics (ESHEP 2016) Skeikampen, Norway, June 15-28, 2016, 2016. arXiv:1609.04150.
URL https://inspirehep.net/record/1486520/files/arXiv:1609.04150.pdf